Petrology and geochemistry of the diamondiferous K-richterite- and leucite-bearing Kareevlei Kaapvaal lamproite

By

Mr. Zuko Qashani

Supervised by

Dr. Geoffrey Howarth

A dissertation submitted in fulfilment for the degree of

Master of Science

in the Department of Geological Sciences,

University of Cape Town, South Africa

February 2023

Declaration

I **ZUKO QASHANI** (Student number: QSHZUK002) hereby declare that the dissertation: *Petrology and geochemistry of the diamondiferous K-richterite- and leucite-bearing Kareevlei Kaapvaal lamproite*, is my own work and has not been previously submitted to the University of Cape Town or another university for a qualification. All the sources contributed to this work have been acknowledged, cited, and referenced.

……Feb…...day of ……12th…….2023

Signed by candidate

Acknowledgments

This study was conducted over a period of two years with the help and support of a number of people. To begin with, I would like to express my gratitude to the University of Cape Town (UCT) Financial Aid for the financial support.

I would like to express my sincere gratitude to my supervisor Dr Geoffrey Howarth for the continuous support of my master's research project, and his patience, motivation, and immense knowledge. His scientific guidance helped me a lot in all the time of research and writing of this thesis. I could not have imagined having a better supervisor and mentor for my master's research project. Also, I would like to thank the following people for their assistance in different parts of my master's research project:

- Dr Jock Robey for providing access to the Kareevlei diamond mine to collect samples analyzed in this study.
- Rene van der Merwe for thin section preparation.
- Jonathan van Rooyen for his assistance in sample preparation for bulk-rock geochemistry
- Associate Professor Phillip Janney and Christel Tinguely for assistance in XRF and ICP-MS analyses.
- Dr Christian Reinke from the University of Johannesburg (UJ), and Nicolas Laider from UCT for their great assistance in Electron Microprobe Analyses.
- Dr Petrus Le Roux for assisting in Sr and Nd isotope analyses.

Abstract

The Kareevlei diamond mine is the first mine on the evolved leucite-bearing Kaapvaal lamproite. These rock types have generally been believed to be non-diamondiferous or at least sub-economic and as a result, their petrogenesis has remained poorly constrained as the exploration programs focused mainly on the unevolved subvarieties of Kaapvaal lamproites, such as at the Finsch mine. To further assist with the petrogenesis of these uncommon diamondiferous rock types, 13 Kaapvaal lamproite samples of hypabyssal texture from the Kareevlei diamond mine have been analyzed for their petrography, mineral chemistry (phlogopite, K-richterite, and diopside), and bulk-rock major and trace elements as well as Sr–Nd isotope compositions. The Kareevlei Kaapvaal lamproites comprise completely altered olivine macrocrysts (3–12 vol.%) set in a groundmass of olivine microcrysts (3–19 vol.%), abundant phlogopite (32–58 vol.%), diopside (12–36 vol.%), pseudo-leucite (0–27 vol.%), K-richterite (0–25 vol.%), and interstitial material containing carbonate minerals.

Two distinct mineralogical varieties are identified based on the presence/absence of leucite and K-richterite: (1) phlogopite-diopside lamproites and (1) leucite-richterite lamproites. Phlogopite laths in these lamproite varieties show two distinct core populations characterized by high-Cr_2O_3 (Cr_2O_3 = 0.89–1.97 wt.%) and low-Cr_2O_3 concentrations (Cr_2O_3 = 0.04–0.68 wt.%), both mantled by TiO_2 and FeO-rich rims. High Cr_2O_3 cores are interpreted as xenocrysts from phlogopite peridotite xenoliths, whereas the low Cr_2O_3 cores resemble MARID xenolith phlogopite. The phlogopite rims have compositions similar to typical Kaapvaal lamproites and represent direct crystallization by the parent magma.

The Kareevlei leucite-richterite lamproites are characterized by raised bulk-concentrations of SiO_2 (44.8 – 47.9 wt.%), Al_2O_3 (6.34–7.34 wt.%), and Na_2O (0.78–1.99 wt.%), and lowered MgO (16.2–17.1 wt.%) concentrations compared to phlogopite-diopside lamproites (SiO_2 = 40.8–42.9 wt.%; Al_2O_3 = 5.44–6.22 wt.%; Na_2O = 0.42–0.74 wt.%, MgO = 20.7–23.0 wt.%). The two mineralogical varieties have distinct incompatible trace element concentrations, with the leucite-richterite samples being depleted in light REEs (LREE/Chondrite: La = 656–828; Ce = 518–597; Nd = 234–261) compared to the phlogopite-diopside samples (LREE/Chondrite: La = 1125–1391; Ce = 817–1029; Nd = 333–415). Additionally, these lamproite varieties exhibit clear separation in incompatible trace element ratios, with leucite-richterite lamproites having lower La/Yb = 101–143, Gd/Yb = 6.28–7.73, and La/Sm = 10.0–11.0, relative to phlogopite-diopside lamproites (La/Yb = 167–205; Gd/Yb = 8.13–9.55; La/Sm = 12.4–13.4). However, these mineralogical varieties have similar $^{87}Sr/^{86}Sr_i$ and $^{143}Nd/^{144}Nd_i$ ratios with ranges of 0.7071–0.7073 and 0.5118–0.5119, respectively.

The two distinct lamproite varieties identified as phlogopite-diopside and leucite-richterite lamproites in this study suggest relative evolution at Kareevlei, marked by the complete absence of K-richterite and leucite in the groundmass of phlogopite-diopside lamproites. The major element compositional trends of lamproites commonly reflect the primary mineralogy. In Kareevlei lamproites, these trends (e.g., MgO depletion with SiO_2, Al_2O_3, and Na_2O enrichment) appear to be controlled by relative mantle xenocryst accumulation rather than evolution through fractional crystallization as the incompatible trace elements and their ratios are not consistent with fractional crystallization control on Kareevlei magma evolution. The Sr-Nd isotopes suggest that both Kareevlei phlogopite-diopside and leucite-richterite lamproites are derived from an isotopically homogeneous mantle source within the sub-continental lithospheric mantle (SCLM). The higher incompatible trace element ratios (e.g., La/Yb, Gd/Yb, and La/Sm) in phlogopite-diopside lamproites are regarded as a consequence of derivation by lower degrees of partial melting. In contrast, the leucite-richterite lamproites with their low La/Yb, Gd/Yb, and La/Sm ratios are indicative of derivation by greater degrees of partial melting.

It is concluded that the Kareevlei lamproite varieties are generated by variable degrees of partial melting of MARID-veined peridotite lithologies in the SCLM. While these lamproites varieties appear to be derived from an isotopically homogenous source, the variation in their groundmass mineralogical assemblages is a consequence of variable degrees of partial melting rather than evolution through fractional crystallization en route to the surface. This hypothesis can be tested in the future for other Kaapvaal lamproite clusters across the Kaapvaal craton to see if variable degrees of partial melting are the primary process responsible for the relative evolution observed.

Contents

List of Tables

List of Figures

CHAPTER 1: INTRODUCTION

Kimberlites and lamproites are petrographically complex rocks formed by the differentiation and crystallization of magmas derived from the upper mantle (Field et al., 2008; Mitchell, 1995, 2006). They are hybrid magmatic rocks comprising abundant mantle xenoliths and xenocrysts (e.g., olivine macrocrysts >25 vol.%) in a fine-grained (<0.5mm) groundmass (Giuliani et al., 2016; Mitchell, 1995, 2006; Scott Smith, 2017). Kimberlites are derived from a common asthenospheric mantle reservoir whereas lamproites have Sr-Nd isotopes suggesting a mantle source within the sub-continental lithospheric mantle (SCLM) (Smith, 1983; Field et al., 2008; Giuliani et al., 2015; Scott Smith, 2017; Becker and Le Roex, 2006; Coe et al., 2008; Mitchell, 2006, 1995; Pearson et al., 2019; Tovey et al., 2021). Kimberlites are the main host to economically viable diamond deposits whereas lamproites are less commonly of economic importance (Figure 1.1).

Lamproites occur in all cratonic regions worldwide and show remarkable mineralogical variety and often distinct varieties are identified in different cratons. For example, in the Kaapvaal craton, lamproites are mostly carbonate-rich subvarieties (e.g., Mitchell, 1995). The lamproites similar to the carbonate-rich lamproites of the Kaapvaal craton occur elsewhere worldwide, for example at Weasua, Man craton (Howarth and Giuliani, 2020), and the Karelian craton (Kargin et al., 2014). Mitchell (2006) suggested that lamproites should be given names based on cratonic-type locality. Subsequently, this has led Scott Smith (2017) to propose the name "Kaapvaal lamproites" for those that occur in the Kaapvaal craton (i.e., previously Group II kimberlites or orangeites). In contrast, Pearson et al. (2019) suggested the term "carbonate-rich olivine lamproites" for Kaapvaal craton lamproites. Hereafter, I use Kaapvaal lamproite for rocks occurring within the Kaapvaal craton in South Africa.

Kaapvaal lamproites exhibit a wide range of mineralogy but are dominated by macrocrystic olivine (~25 vol.%) set in a groundmass of microcrystic olivine (<0.5 mm) (~25 vol.%), phlogopite, diopside, apatite, lesser spinel, perovskite, with or without K-richterite, sanidine, and leucite (Mitchell, 1995). They can be broadly divided into two varieties/endmembers, 1) unevolved varieties and 2) evolved varieties. The unevolved varieties are characterized by phlogopite-rich groundmass which may be similar to phlogopite-rich archetypal kimberlite groundmass. They can be distinguished from kimberlites by the presence of primary diopside in the groundmass, which is never present in kimberlites (Mitchell, 1995). The evolved varieties are characterized by the presence of K-richterite, leucite, and sanidine in the groundmass. Evolved varieties have been previously suggested to originate through fractional crystallization and evolution of an unevolved parent melt (e.g., Mitchell, 1995; Howarth et al., 2011). During fractionation, any solid component in the magma would be lost through gravitational settling and this would include diamonds. As a result, the evolved varieties of Kaapvaal lamproites are generally believed to be sub-economic, and therefore, exploration efforts only target the unevolved varieties (see Figure 1.1) (e.g., Mitchell, 1995; Howarth et al., 2011; Scott Smith, 2017).

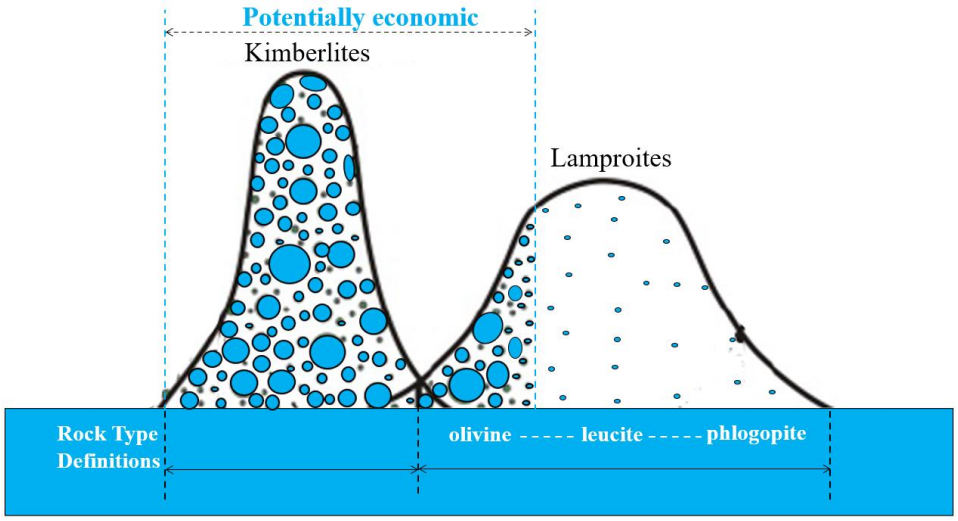

Figure 1. 1: Schematic representation of petrographic-based definitions for kimberlites and lamproites. Each petrographic group is represented by a curve. The width of the base of each curve represents a relative range of mineralogical composition for each group, height represents relative frequency worldwide, and the blue circles mimic 25 vol.% of olivine macrocryst abundances (adapted from Scott Smith, 2017)

The recent development of the Kareevlei diamond mine has revealed that K-richterite and leucite–bearing Kaapvaal lamproite, which falls under the evolved endmember, can be diamondiferous and of economic importance. The Kareevlei diamond grade is low at 5.0 cpht but diamonds are of high quality and exceed US$300 per carat, placing Kareevlei mine in the top 10 worldwide in terms of diamond quality (Grillz and Lohrentz, 2019). As a result, the inference that evolved Kaapvaal lamproites are sub-economic requires re-evaluation.

1.1 Aims and Objectives

The Kareevlei diamond mine is located approximately 130 km northwest of Kimberley, South Africa, close to other Cretaceous-aged (125–110 Ma) Kaapvaal lamproites in the southwestern part of the Kaapvaal craton (see Figure 1.2). It is the first diamond mine on an evolved K-richterite- and leucite-bearing Kaapvaal lamproite. The major goal of this study is to evaluate the petrogenesis of these uncommon rocks and evaluate the current models of Kaapvaal lamproite evolution through the fractional crystallization of a common parent melt. In order to achieve this goal, here I present the petrography, mineral chemistry, and bulk-rock geochemistry of 13 Kaapvaal lamproite samples. The primary objectives of this study are:

- Mineralogical classification of the Kareevlei Kaapvaal lamproite on the basis of groundmass mineralogy, which will be achieved by presenting detailed petrographic descriptions of the Kareevlei samples to identify the primary groundmass mineralogy.

- Constrain the xenocrystic vs magmatic origin of the groundmass phases by presenting major element compositions of each primary groundmass phase (i.e., phlogopite, K-richterite, and diopside compositions).
- Constrain the mantle source with the use of Sr–Nd isotope compositions.
- Finally, the effects of variable partial melting degrees in the source will be evaluated by presenting and evaluating bulk-rock geochemistry, specifically by evaluating the correlation between Sr-Nd isotopes and incompatible trace element ratios.

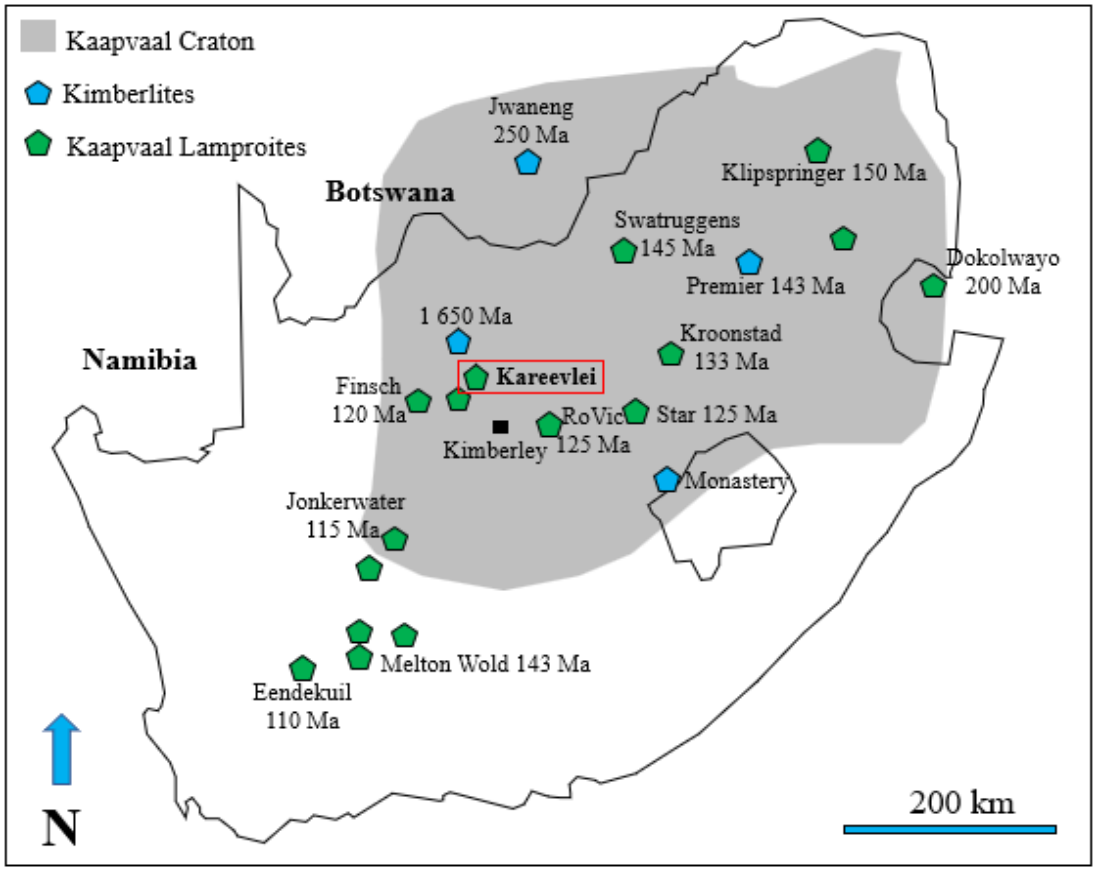

Figure 1. 2: Map of southern Africa illustrating the location of the Kareevlei lamproites as well as other major well-known Kaapvaal lamproites within the Kaapvaal craton (adapted from Howarth and Nembambula, 2021). Kareevlei and other Kaapvaal lamproites have not been dated. Note: RoVic = Robert Victor.

CHAPTER 2: BACKGROUND

2.1 Age, occurrence, and distribution of Kaapvaal lamproites

There are estimated to be 229 occurrences of Kaapvaal lamproites, and they mainly occur as clusters of pipes and intrusions (i.e., dikes/sills) in southern Africa (Skinner et al., 1992; Mitchell, 1995). A few Kaapvaal lamproites occur in an off-craton setting at the far southwestern margin of the craton (Clarke et al., 1991; Skinner et al., 1994) (Figure 1.2). The on-craton clusters predominantly occur around Kimberley in the southwestern part of the craton. Kaapvaal lamproites in southern Africa have been dated with an age range of 200 Ma – 110 Ma (Skinner, 1989; Smith et al., 1985). The Kaapvaal lamproite intrusion clusters in an off-craton setting have been dated (e.g., Skinner, 1989; Smith et al., 1985) younger than the other intrusions, and ages appeared to decrease progressively from the northeast to the southwestern part of the craton (Mitchell, 1995).

All these intrusions are reported to have been emplaced over a period of about 25 Myr in different provinces rather than sequentially (e.g., Mitchell, 1995). The youngest intrusions include Kaapvaal lamproites occurring in an off-craton setting around the Prieska area (Skinner, 1989; Skinner et al., 1994; Smith et al., 1994). Concerning the above, Mitchell (1995) suggests that there were two Kaapvaal lamproite magmatic events rather than one period of activity. Consequently, clusters in the lower southwestern part of the craton are dated at Cretaceous (~125 – 110 Ma) in age and form a widely synchronous group of intrusion with no spatial correlation (Mitchell, 1995). However, 143-Ma Melton Wold appears to be anomalous compared to other Kaapvaal lamproites in the southwestern part and off-craton setting. The status and age of this intrusion would require reinvestigation (e.g., Mitchell, 1995). The clusters in the central to the north-eastern part of the craton have been dated as being Upper-Jurassic in age (165–145 Ma) (e.g., Mitchell, 1995). They have been regarded as separate magmatic events rather than the early portions of the age trend (Mitchell, 1995).

The majority of Kaapvaal lamproites occur as en-echelon dike swarms such as those from Swartruggens and Star (Mitchell, 1995; Coe et al., 2008). This intrusion style is not common in kimberlites but is a diagnostic feature of many lamprophyre suites (Currie and Ferguson, 1970). Kaapvaal lamproites evolve to residual magmas, which crystallize amphiboles, sanidine, leucite, and aegirine (Mitchell, 1995). Mitchell (1995) noted that each Kaapvaal lamproite field differs with respect to mineralogical composition and degree of evolution. As a result, Barkly West Cluster has been reported (e.g., Mitchell, 1995) to be characterized by macrocrystic olivine-rich lamproites, whereas the other fields are relatively poor in macrocrystic lamproites. Kroonstad and Prieska Clusters are relatively more evolved than the Finsch and Winburg Clusters (Mitchell, 1995).

2.2 Mineralogy of lamproites

Lamproites are defined as potassium-rich igneous rocks (typically K_2O >5 wt.%) that possess diagnostic mineralogy and geochemistry (Wagner and Velde, 1986; Bergman, 1987; Prelevic et al., 2008). The mineralogy of these rocks reflects their peralkaline ultrapotassic nature (Mitchell and Bergman, 1991). Lamproites are characterized by the occurrence of Ti-phlogopite, K-richterite, Ti-tetraferriphlogopite, Na- and Al-poor leucite, Fe-rich sanidine, K-barian titanates (priderite and jeppeite), Ti-silicates, and Al-poor diopside (Mitchell and Bergman, 1991). As has been mentioned, not all the above phases have to be present for the rock to be referred to as lamproite. Generally, kimberlites and lamproites are classified based on two or three abundant groundmass phases, excluding olivine (Mitchell et al., 2019). Perovskite, wadeite, apatite, and Mg-chromite are minor and accessory phases in lamproites (Bergman, 1987; Mitchell, 1995; Mitchell and Bergman, 1991; Woolley et al., 1996).

Lamproites include the carbonate-rich subtypes that occur on the Kaapvaal craton, termed carbonate-rich olivine lamproites (e.g., Pearson et al., 2019), previously known as orangeites (e.g., Mitchell, 1995) and here called Kaapvaal lamproites as suggested by Scott-Smith (2017). These rocks encompass a wide range of mineralogy and are divided into two endmembers: (1) unevolved and (2) evolved varieties (e.g., Howarth et al., 2011; Mitchell, 1995). The unevolved varieties are primarily characterized by a groundmass of abundant phlogopite (~50 vol. %) and minor groundmass phases such as diopside, spinels of various compositions ranging from Mg-chromite to Ti-magnetite, perovskite, Sr-rich apatite, REE-rich phosphates, K-barian titanates that belong to hollandite group, Mn-ilmenite, Nb-rutile, and the carbonate-serpentine mesostasis (Mitchell, 1995). These unevolved varieties of Kaapvaal lamproites are more similar to archetypal kimberlites in terms of their mineralogy, whereas the evolved varieties are characterized by alkali-rich groundmass phases such as sanidine, leucite, K-richterite, and abundant diopside with aegirine overgrowths and are similar to lamproites that occur elsewhere worldwide (Mitchell, 1995).

2.2.1 Comparing mineralogical characteristics of lamproites with kimberlites

Lamproites are interpreted as being highly enriched in phlogopite (up to ~50 vol.%) compared to kimberlites (<20 vol.%). Microphenocrystic phlogopite is not a characteristic mineral of kimberlites, although many comprise minor volumes (typically <1 vol.%) of macrocrystic phlogopite (Mitchell, 1995). When these phlogopites are present in kimberlites, they typically occur as late-stage colorless laths of phlogopite-kinoshitalite and commonly show poikilitic textures (Mitchell, 1995). Calcite-serpentine segregation texture is common in many kimberlites, and these textures appear to be less common in lamproites (Mitchell, 1995). However, unevolved subtypes of Kaapvaal lamproites can comprise abundant calcite-serpentine mesostasis, such as those from Finsch (Fraser and Hawkesworth, 1992).

The more evolved subvarieties of Kaapvaal lamproites generally lack calcite-serpentine segregations. The quenched sheaf-like textured apatite has been reported to be common in kimberlites (e.g., Mitchell, 1995) but not typical in Kaapvaal lamproites. Kimberlites are spinel and perovskite-rich and typically appear to be relatively coarse-grained compared to Kaapvaal lamproites (Skinner, 1989; Mitchell, 1995; Field et al., 2008). The only kimberlites that exhibit similar mineralogical characteristics with unevolved Kaapvaal lamproites are those that are rich in phlogopite, and they have been referred to as micaceous kimberlites, such as those from Dutoitspan (e.g., Ramokgaba et al., 2021) and Jagersfontein (e.g., Taylor and Kingdom, 1999). These micaceous kimberlites typically exhibit textural and mineralogical characteristics of other kimberlites which makes them differ from lamproites, that is, they are rich in oxides, comprise atoll spinels, and have calcite-segregation textures while the tetraferriphlogopite and diopside are absent (Mitchell, 1995). The presence of monticellite in the groundmass of kimberlites indicates low silica activity in kimberlitic magmas; hence diopside is absent from kimberlite groundmass (Mitchell, 2008) whereas diopside can be a primary phase in Kaapvaal lamproites (Mitchell, 1995).

Table 2. 1: Summary of mineralogical variation between kimberlites and lamproites (taken from Mitchell, 1995 and Howarth et al., 2011).

	Kimberlites	**Lamproites**
Olivine macrocrysts	Abundant	Common, but rare in more evolved varieties
Olivine microcrysts	Common sub/euhedral olivine	Common to minor sub/euhedral
Macrocryst mica	Minor phlogopite	Common phlogopite
Microcryst mica	Rare phlogopite	Common phlogopite
Groundmass mica	Common laths of phlogopite-kinoshitalite	Common poikilitic plates of tetraferriphlogopite
Spinel	Abundant, coarse-grained. Typically, Mg-chromite zoned to Mg-ulvospinel	Minor - rare. Mg-chromite rarely zone to Ti-magnetite
Monticellite	Common, and may be pseudomorphed by carbonate or serpentine	Common in unevolved varieties, and typically pseudomorphed by carbonate or serpentine
Diopside	Primary diopside is absent, may be present in contaminated groundmass	Microcrysts, common - rare
Perovskite	Common, euhedral to rounded	Rare, subhedral to poikilitic
Apatite	Common to rare, euhedral prisms or acicular radiation aggregates	Common euhedral prisms and poikilitic plates
Melilite	Common - always pseudomorphed	Common - always pseudomorphed
Carbonates	Simple assemblage (common calcite and minor dolomite)	Common calcite, common Sr-Mn-Fe dolomites, minor witherite, ancylite, and stronitanite
Serpentine	Abundant secondary and primary segregations	Common secondary
Sanidine	Absent	Common in the groundmass of more evolved varieties
K-richterite	Absent	Common in the groundmass of more evolved varieties
Aegirine	Absent	Common in the groundmass of more evolved varieties
Leucite	Absent	Common in the groundmass of more evolved varieties
K-Ba hollandite	Very rare	Common
Mn ilmenite	Rare	Common
Zr-silicates	Very rare	Common
Barite	Rare	Common
Megacrysts	Characteristic	Rare to absent

2.2.2 Groundmass mineral chemistry

Phlogopite chemistry

The compositional variations in minerals have become convenient when distinguishing kimberlites from lamproites and other related rocks (e.g., Mitchell, 1995; Shaikh et al., 2018; Howarth and Giuliani, 2020). Phlogopite is one of the few minerals that preserve the history of petrogenesis from the mantle to the surface with its distinct core–rim zones reflecting rapid changes in crystallization conditions (Giuliani et al., 2016; Shaikh et al., 2017). Thus, phlogopite is a good petrogenetic indicator of magma compositional evolution (Giuliani et al., 2016; Mitchell, 1995) and is useful to discriminate kimberlites from lamproites. Unlike phlogopite in kimberlites, the phlogopite in lamproites exhibits compositions ranging from phlogopite to tetraferriphlogopite (e.g., Mitchell, 1995). The phlogopite compositional variations are evaluated by major elements plots of Al_2O_3 against FeO and TiO_2 as shown in Figure 2.1 below. Phlogopites in kimberlites are clearly distinguished by the Al_2O_3 enrichment trend with no significant variation in FeO and TiO_2. In Kaapvaal lamproites, phlogopites exhibit core-to-rim Al_2O_3 depletion trends coupled with constant FeO and TiO_2 enrichment towards the tetraferriphlogopite rims.

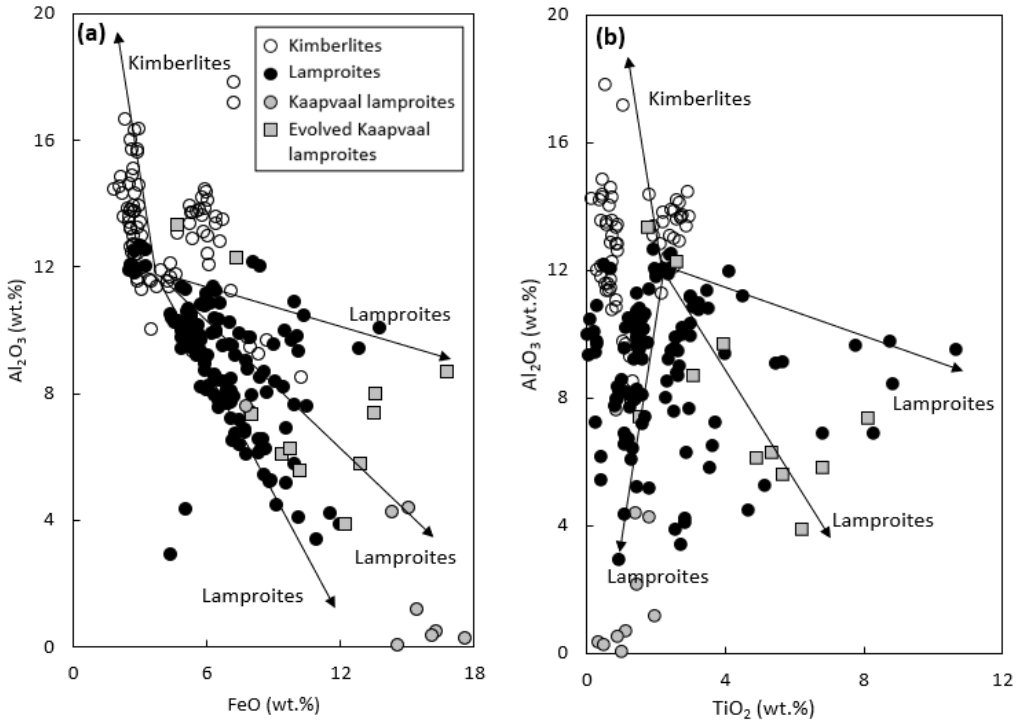

Figure 2. 1: Phlogopite compositional variation plots of major elements Al_2O_3, FeO, and TiO_2 in kimberlites and lamproites. (a) Al_2O_3 vs FeO. (b) Al_2O_3 vs TiO_2. The arrows represent evolutionary trends from core to rims of phlogopite in kimberlites and lamproites. Phlogopite literature data for kimberlites are from Tongo (Howarth and Giuliani, 2020), India (Shaikh et al., 2018); lamproites data from West Kimberley and Leucite Hills (Mitchell and Bergman, 1991), Weasua (Howarth and Giuliani, 2020), India (Shaikh et al., 2018); Kaapvaal lamproites and their evolved subtypes are from the Kaapvaal craton (Mitchell, 1995).

K-richterite chemistry

K-richterite is a late-stage groundmass phase that generally crystallizes contemporaneously with groundmass poikilitic phlogopite in lamproites and is never observed in kimberlites (Konzett, 1997; Mitchell, 1995). It is part of the evolved Kaapvaal lamproite mineral suite (Mitchell, 1995). The paragenesis of K-richterite in Kaapvaal lamproites and any other lamproites elsewhere worldwide has been reported to be similar (e.g., Mitchell, 1995) (Figure 2.2a–b. However, the only key difference that has been noted is that Kaapvaal lamproites tend to have K-richterite that is poorer in TiO_2 (< 1 wt.%; Mitchell, 1995), relative to K-richterite in other lamproites worldwide (TiO_2 = 1–7 wt.%; Mitchell and Bergman, 1991) (Figure 2.2b).

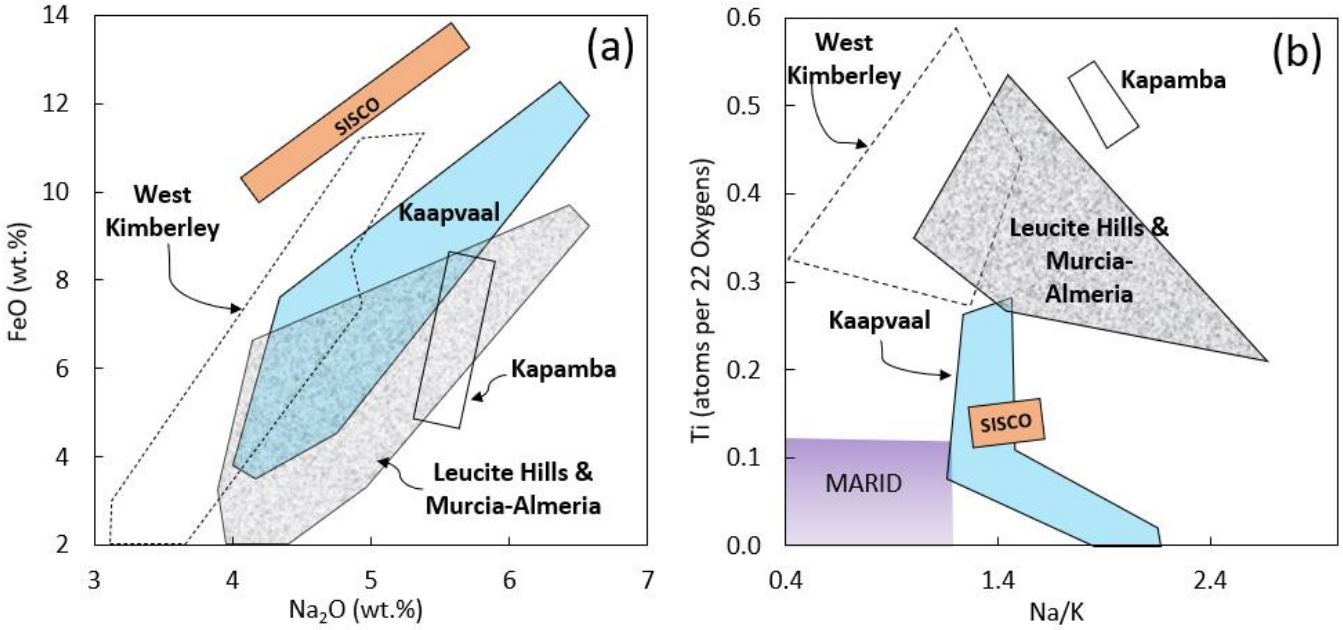

Figure 2. 2: The (a) Na_2O vs FeO and (b) Na/K vs Ti compositional variation of K-richterites from Kaapvaal lamproites (from Pniel and Besterskraal; Mitchell, 1995) and other lamproites from West Kimberley (Mitchell and Bergman, 1991), Leucite Hills and Murcia-Almeria (Mitchell and Bergman, 1991), Sisco (Mitchell and Bergman, 1991), and Kapamba (Mitchell, 1995). The K-richterite compositions of mica-amphibole-rutile-ilmenite-diopside (MARID) xenoliths are from Dawson and Smith (1977).

Diopside chemistry

Diopside is interpreted to have been crystallized contemporaneously with leucite after groundmass phlogopite crystallization in Kaapvaal lamproites (e.g., Mitchell and Bergman, 1991; Tainton, 1992). Significantly, diopside is the primary characteristic feature of lamproites, and it is not observed in kimberlites unless those kimberlites have assimilated crustal xenoliths (Mitchell, 1995). In Kaapvaal lamproites, the diopside has been reported to be relatively more abundant in the evolved subtypes and the majority are Fe-poor zonation-free diopside phenocrysts with little extension towards hedenbergite (see Figure 2.3a) (e.g., Mitchell, 1995).

Diopsides are typically zonation-free in lamproites worldwide (Mitchell, 1995). However, when zonation is present, it is defined by compositionally distinct core zones (e.g., Fe- and Al-rich) that are unlike any of the diopside phenocrysts. Compositions of these core zones typically trend from diopside to hedenbergite and augite compositions and have been interpreted to be associated with clinopyroxenite xenoliths in Leucite Hills lamproites (e.g., Barton and Van Bergen, 1981; Mitchell and Bergman, 1991) (Figure 2.3a–b). The distinct Fe- and Al-rich core zones are typically mantled by zones similar in composition to diopside phenocrysts (Mitchell and Bergman, 1991).

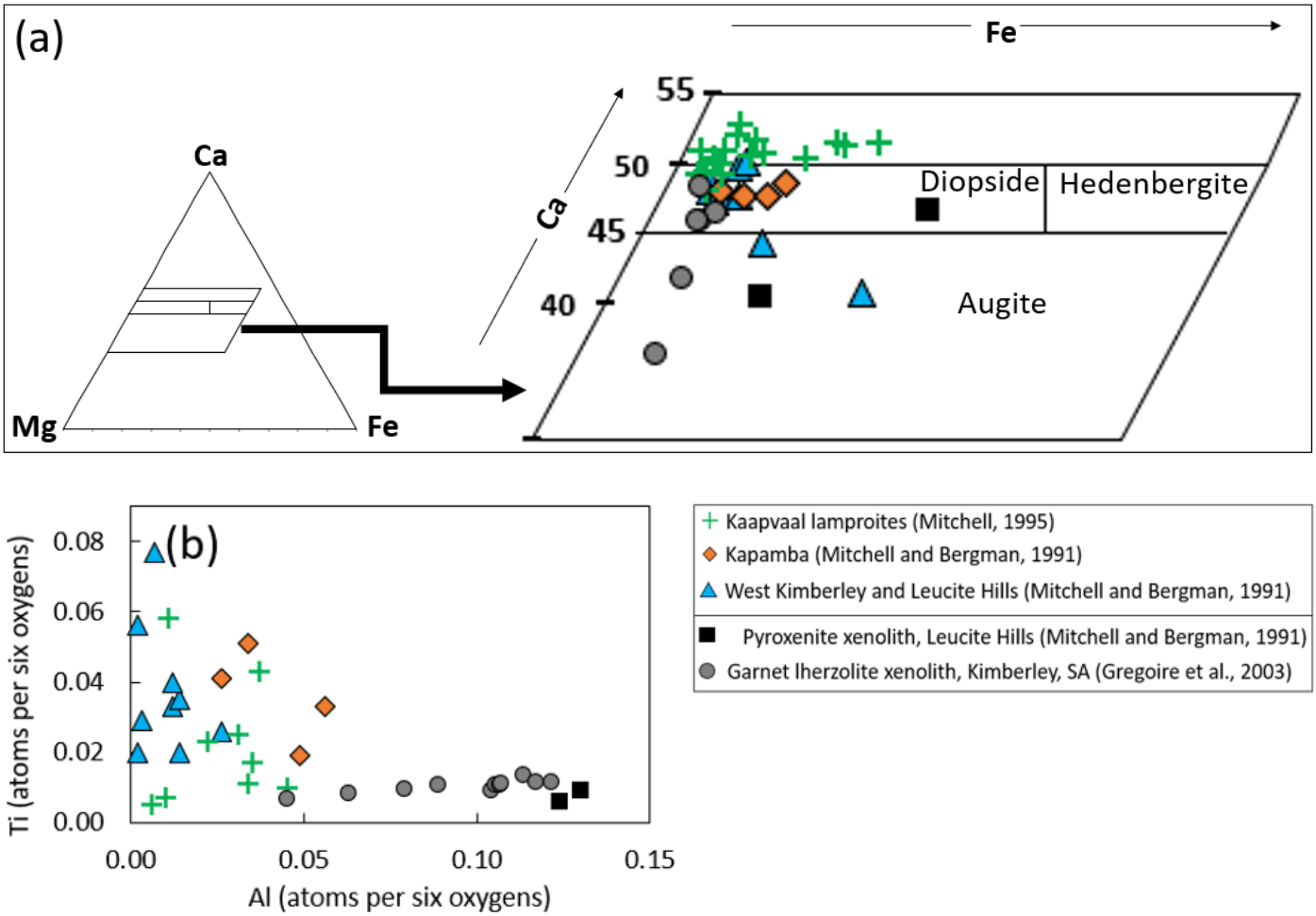

Figure 2. 3: Compositions of diopsides from lamproites (Mitchell, 1995; Mitchell and Bergman, 1991) and pyroxenite xenoliths (Mitchell and Bergman, 1991) and garnet lherzolite xenoliths (Grégoire et al., 2003) on (a) Ca -Mg-Fe quadrilateral and (b) Al-Ti plots.

2.3 Geochemical features of kimberlites, lamproites, and Kaapvaal lamproites

The mineralogy of kimberlites and lamproites reflects the major element geochemistry of these rocks. Petrographic observations reveal that Kaapvaal lamproites are relatively macrocrystic olivine-poor compared to kimberlites, such as those at New Elands and Swartruggens (Mitchell, 1995). However, the "unevolved" subvariety of Kaapvaal lamproites is a mixture of abundant macrocrystic olivines interpreted to be derived by assimilation of mantle-derived harzburgite and/or lherzolite xenoliths, with phlogopite, carbonates, and apatite (e.g., Mitchell, 1995; Becker and Le Roex, 2006). Thus, Mitchell (1995) argues that olivine macrocrysts may be considered contaminants in these magmas, whereas the other phases are primary or magmatic phases. High macrocrystic olivine contents in unevolved varieties of lamproites impart higher MgO and lower SiO_2 contents, making them less distinguishable from kimberlites (Mitchell, 1995; Pearson et al., 2019).

2.3.1 Geochemistry of kimberlites

Kimberlites have been reported to show a wide range in major element compositions because of differentiation and variation in modes of macrocrystic olivine and primary phases (e.g., Mitchell, 1986; Gurney and Ebrahim, 1973; Smith et al., 1985). Macrocrystic olivine-rich kimberlites are generally enriched in SiO_2 and MgO compared to the macrocrystic olivine-poor kimberlites (Becker and Le Roex, 2006). The concentrations of MgO and SiO_2 in these rocks display a broad positive correlation (Figure 2.4a) with relatively low SiO_2 contents and higher MgO contents (Becker and Le Roex, 2006). Higher FeO contents (relative to lamproites) have been interpreted to be a consequence of contamination by ilmenite megacrysts (e.g., Boyd and Nixon, 1975; Robey, 1981; Becker and Le Roex, 2006). These FeO concentrations (ranging from 7.6–15.4 wt.%) generally display a broad negative correlation with MgO (Figure 2.4b).

By definition, kimberlites are considered to be SiO_2-poor (25 – 35 wt.%), Al_2O_3-poor (<5 wt.%), and low Na_2O/K_2O ratios (<0.5) (Mitchell, 1995). These rocks are generally potassic but not peralkaline, and thus, their major element geochemistry resembles that of unevolved varieties of Kaapvaal lamproites (Mitchell, 1995). Therefore, these two rock types cannot be simply distinguished by their major element geochemistry. It has been revealed that K_2O and TiO_2 may give an effective discriminant only when both elements are greater than 1 wt.% (e.g., Smith et al., 1985). The K_2O vs TiO_2 variation plots are of importance as they reflect phlogopite mica abundances in kimberlites and lamproites. In these variation plots, kimberlites are typically characterized by high TiO_2 and low K_2O concentrations (Figure 2.4c) (Mitchell, 1995). The high TiO_2 contents are ascribed to the presence of abundant Ti-rich spinel and perovskite in the kimberlite's groundmass. Low K_2O and Al_2O_3 concentrations in kimberlites reflect the scarcity of phlogopite and the common occurrence of kinoshitalite-rich groundmass mica (Mitchell, 1995).

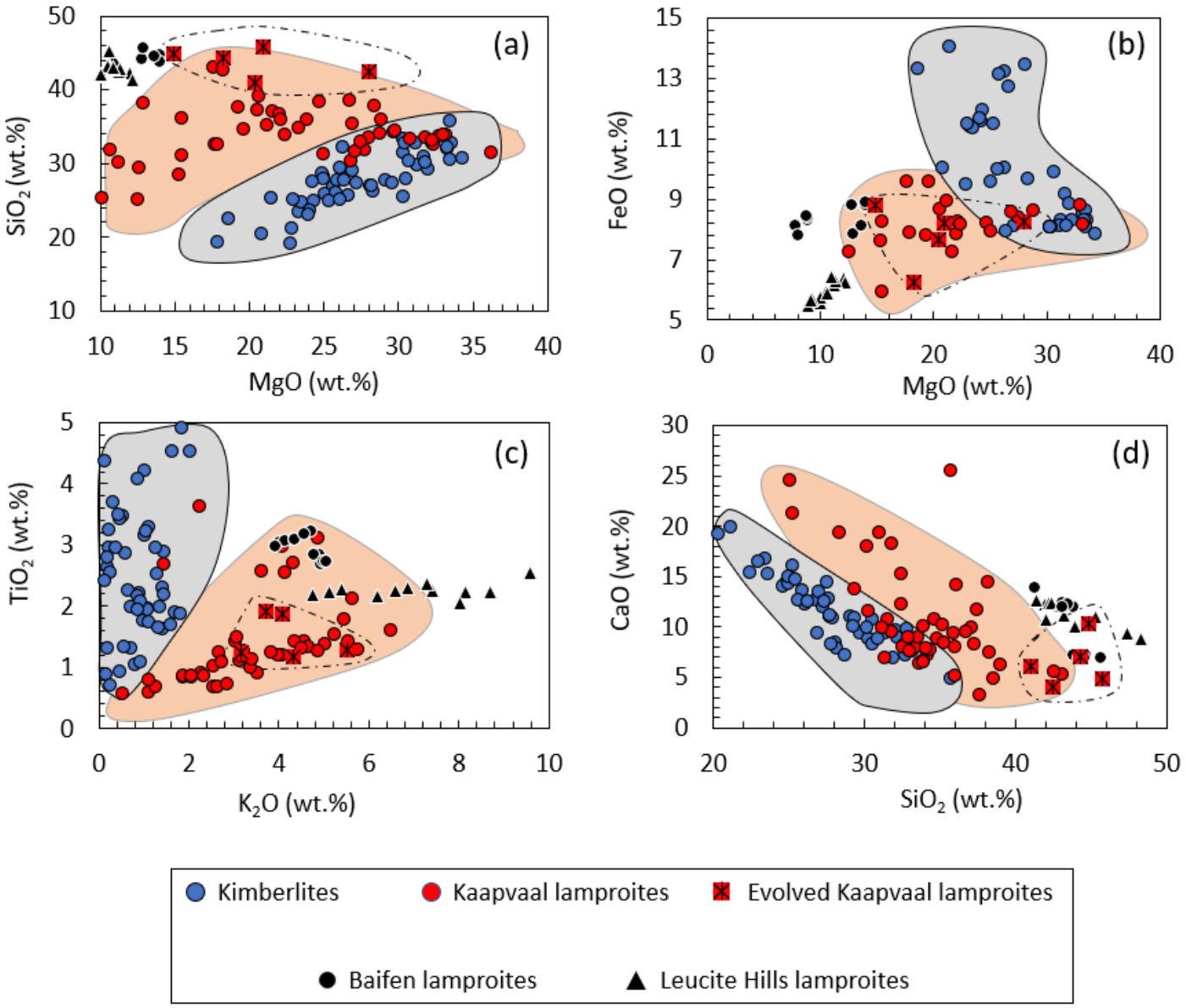

Figure 2. 4: Variations of (a) MgO vs SiO_2, (b) MgO vs FeO, (c) K_2O vs TiO_2, (d) SiO_2 vs CaO for kimberlites (data from Le Roex et al., 2003; Harris et al., 2004; Becker and Le Roex, 2006), Kaapvaal lamproites (Becker and Le Roex, 2006; Coe et al., 2008) and Leucite Hills and Baifen lamproites (Mirnejad and Bell, 2006; Xiang et al., 2020). Note that the evolved Kaapvaal lamproites are marked by a red square with a star (Mitchell, 1995). The gray fields represent kimberlites compiled from Le Roex et al. (2003) and Becker and Le Roex (2006). Orange fields represent Kaapvaal lamproites compiled from Becker and Le Roex (2006) and Coe et al. (2008). Dotted fields represent evolved subtypes of Kaapvaal lamproites (Mitchell, 1995).

Becker and Le Roex (2006) have shown that the high field strength elements (HSFE: Zr, Nd, and Hf) in combination with other incompatible elements cover a wide range of concentrations in kimberlites. Kimberlites typically show a sub-parallel pattern for chondrite-normalized rare earth elements (REE) (Figure 2.5a) with recognizable light REE (e.g., LREE: La = 300–1300) enrichment compared to heavy REE (e.g., HREE: Lu = 3–8) (Becker and Le Roex, 2006). In primitive mantle (PM) normalized trace element patterns, these rocks are strongly enriched in incompatible elements (e.g., Nb = 155–603 and Ba = 24–326) and relatively depleted in Rb, K, Sr, Hf, and Ti (Figure 2.6a) (Becker and Le Roex, 2006). Le Roex et al. (2003) and Harris et al. (2004) reported that the negative anomalies of Rb, K, Sr, Hf, and Ti in the PM-normalized

patterns are characteristic features of kimberlites. Therefore, Rb and K negative anomalies tend to be larger in kimberlites, whereas Kaapvaal lamproites generally lack these anomalies (see Figures 2.6a and b) (Becker and Le Roex, 2006; Harris et al., 2004; Pearson et al., 2019). Kimberlites are also characterized by rare positive Zr-Hf anomaly, which has been interpreted by Becker and Le Roex (2006) as a consequence of contamination by zircon megacrysts (Figure 2.6a).

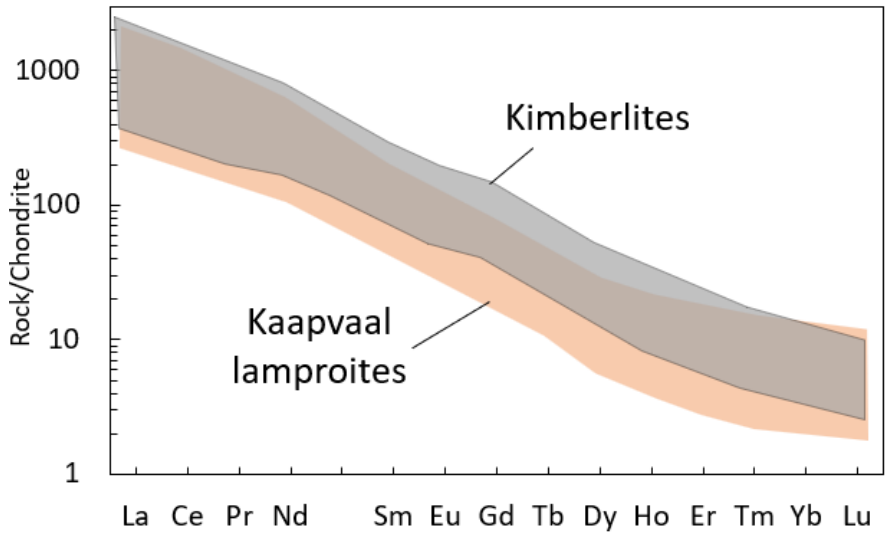

Figure 2. 5: Chondrite-normalized REE patterns for kimberlites (Becker and Le Roex, 2006; Harris et al., 2004; Le Roex et al., 2003) and Kaapvaal lamproites (Becker and Le Roex, 2006; Coe et al., 2008).

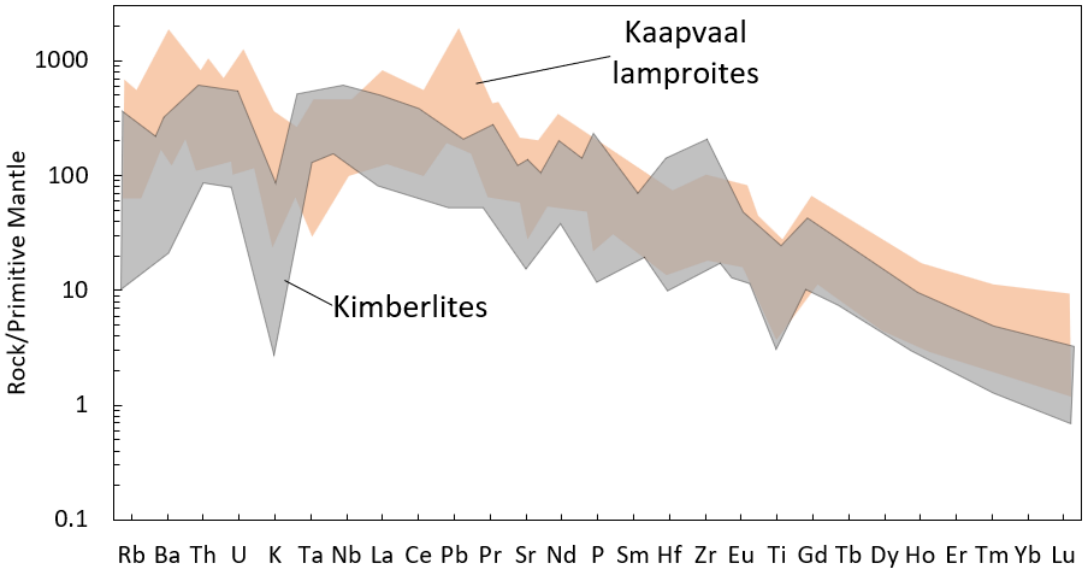

Figure 2. 6: Primitive mantle-normalized trace elements patterns for kimberlites (Becker and Le Roex, 2006; Harris et al., 2004; Le Roex et al., 2003) and Kaapvaal lamproites (Becker and Le Roex, 2006; Coe et al., 2008).

The initial Sr-Nd isotope ratios of kimberlites are $(^{87}Sr/^{86}Sr)_i$ ~0.70328 to 0.70537 and $(^{143}Nd/^{144}Nd)_i$ ~ 0.512491 to 0.512711, typically low and high compared to the present day bulk earth respectively (Smith, 1983; Smith et al., 1985; Le Roex et al., 2003; Becker and Le Roex, 2006) (Figure 2.7). Kimberlite isotope ratios reveal that the kimberlite mantle source appears to have evolved along a uniform isotopic trajectory over a period of 2 billion years, which has been suggested to indicate that kimberlites worldwide are derived from the same homogeneous reservoir (Woodhead et al., 2019). These magmas originate at depths greater than 140 km (Smith, 1983; Mitchell, 1995; Mitchell, 2008; Mitchell et al., 2019), and during their formation, they incorporate lithospheric material en route to the surface, altering the kimberlite primary magma composition (Woodhead et al., 2019; Giuliani et al., 2020). As a result, kimberlites show vast variation in mineralogy but similar isotopic ratios (Giuliani et al., 2020; Woodhead et al., 2019).

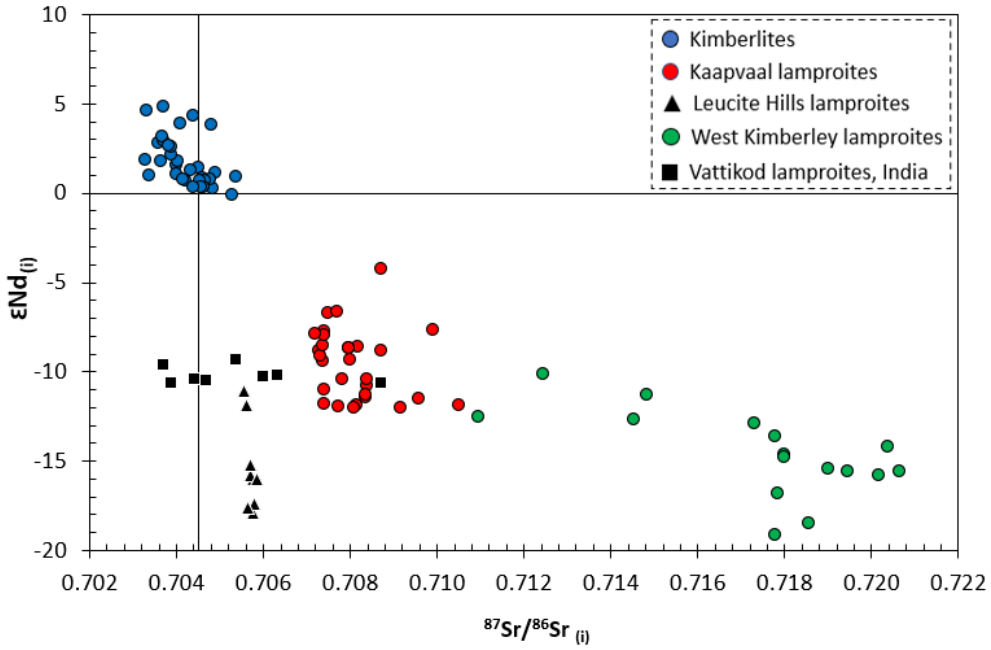

Figure 2. 7: Sr-Nd diagram showing the isotopic compositions of kimberlites (Becker and Le Roex, 2006), Kaapvaal lamproites (Becker and Le Roex, 2006; Coe et al., 2008), Leucite Hills and Baifen lamproites (Mirnejad and Bell, 2006; Xiang et al., 2020), West Kimberley lamproites (Fraser, 1988), and Vattikod lamproites (Talukdar et al., 2018). Note, the horizontal and vertical line within the plotting area represent the present-day bulk earth.

2.2.3 Geochemistry of lamproites

Lamproites worldwide are generally characterized by higher K_2O, SiO_2, and TiO_2 concentrations and lower FeO, and CaO concentrations relative to both kimberlites and Kaapvaal lamproites (Mitchell and Bergman, 1991) (see Figure 2.4a–d). These rocks have also higher K_2O/Na_2O ratios, typically > 5 (Mitchell and Bergman, 1991). Phlogopite-sanidine lamproites are mineralogical distinct from Kaapvaal lamproites to the point that bulk-rock composition comparison is unnecessary (Mitchell, 1995). However, olivine and madupitic lamproites are SiO_2-poor and K_2O-rich rocks with mineralogical and compositional affinities with evolved varieties of Kaapvaal lamproites (Mitchell, 1995).

Phlogopite and madupitic lamproites show a large range in isotopic characteristics, with initial values of $(^{87}Sr/^{86}Sr)_i$ = 0.70523–0.70606 and $(^{143}Nd/^{144}Nd)_i$ = 0.511256–0.512311 (Bergman, 1987). The Ti, Mg, and K enrichment and the Ca, Na, Al depletion of primitive lamproites indicate that they are derived by partial melting of harzburgite-rich sources under reduced H_2O-rich conditions (Bergman, 1987; Mitchell and Bergman, 1991). Initial melts that form these rocks originated from SCLM sources (Bergman, 1987; Mitchell and Bergman, 1991).

2.2.4 Geochemistry of Kaapvaal lamproites

It was initially discovered by Wagner (1914) and later demonstrated by Smith et al. (1985) that Kaapvaal lamproites have major element compositions distinct from kimberlites. In contrast to kimberlites, these rocks are relatively SiO_2-rich (29.0–43.1 wt.%; Becker and Le Roex, 2006). Kaapvaal lamproites generally show a large variation in MgO contents and Mg# (MgO = 17.1–36.3 wt.% and Mg# = 0.80–0.91) amongst macrocryst-rich Kaapvaal lamproites (Becker and Le Roex, 2006). These variations reflect the variable modal abundances of olivine (Becker and Le Roex, 2006; Mitchell, 1995). The MgO-rich Kaapvaal lamproites are more macrocrystic olivine-rich, whereas the evolved varieties (e.g., those from Eendekuil) have substantially lower MgO and Mg#, which has been argued to be the consequence of intense fractionation (e.g., Becker and Le Roex, 2006).

Incompatible trace element ratios are proven useful for distinguishing Kaapvaal lamproites from kimberlites in the Kaapvaal craton (e.g., Becker and Le Roex, 2006; Coe et al., 2008; Howarth et al., 2011). The Pb and Large Ion Lithophile Elements (LILE) concentrations in Kaapvaal lamproites show a poor correlation with more immobile incompatible elements (e.g., La) (Becker and Le Roex, 2006). However, they are notably higher than those in kimberlites (e.g., Becker and Le Roex, 2006). Kaapvaal lamproites have been reported to have higher ratios of Th/Nb (0.21 ± 0.06), Ba/Nb (24 ± 10), and La/Nb (1.6 ± 0.5) and lower ratios of Ce/Pb (16 ± 12) than kimberlites (Figures 2.8a and b) (e.g., Becker and Le Roex, 2006). In the chondrite-normalized REE plots, these rocks display sub-parallel REE patterns and extreme enrichment in LREE (La = 1600) relative to HREE (Lu = 2–10) (Becker and Le Roex, 2006) (Figure 2.5).

Kaapvaal lamproites have recognizable higher ratios of La/Yb and La/Sm, whereas kimberlites show higher Gd/Yb ratios (Figures 2.8c and d). The initial Sr-Nd isotope ratios of these rocks are $(^{87}Sr/^{86}Sr)_i$ ~ 0.70728 to 0.70837 and $(^{143}Nd/^{144}Nd)_i$ ~ 0.511865 to 0.512055, generally higher and lower than the present day bulk earth respectively (Smith, 1983; Smith et al., 1985; Becker and Le Roex, 2006) (see Figure 2.7). Smith (1983) argued that Kaapvaal lamproite magmas are derived from sources that possess low U/Pb and Nd/Sm and high Rb-Sr ratios. The source of Kaapvaal lamproites is interpreted (e.g., Smith, 1983; Coe et al., 2008) to be the SCLM and generated by melting of highly metasomatized lithologies such as the mica-amphibole-rutile-ilmenite-diopside (MARID) xenoliths (Giuliani et al., 2015).

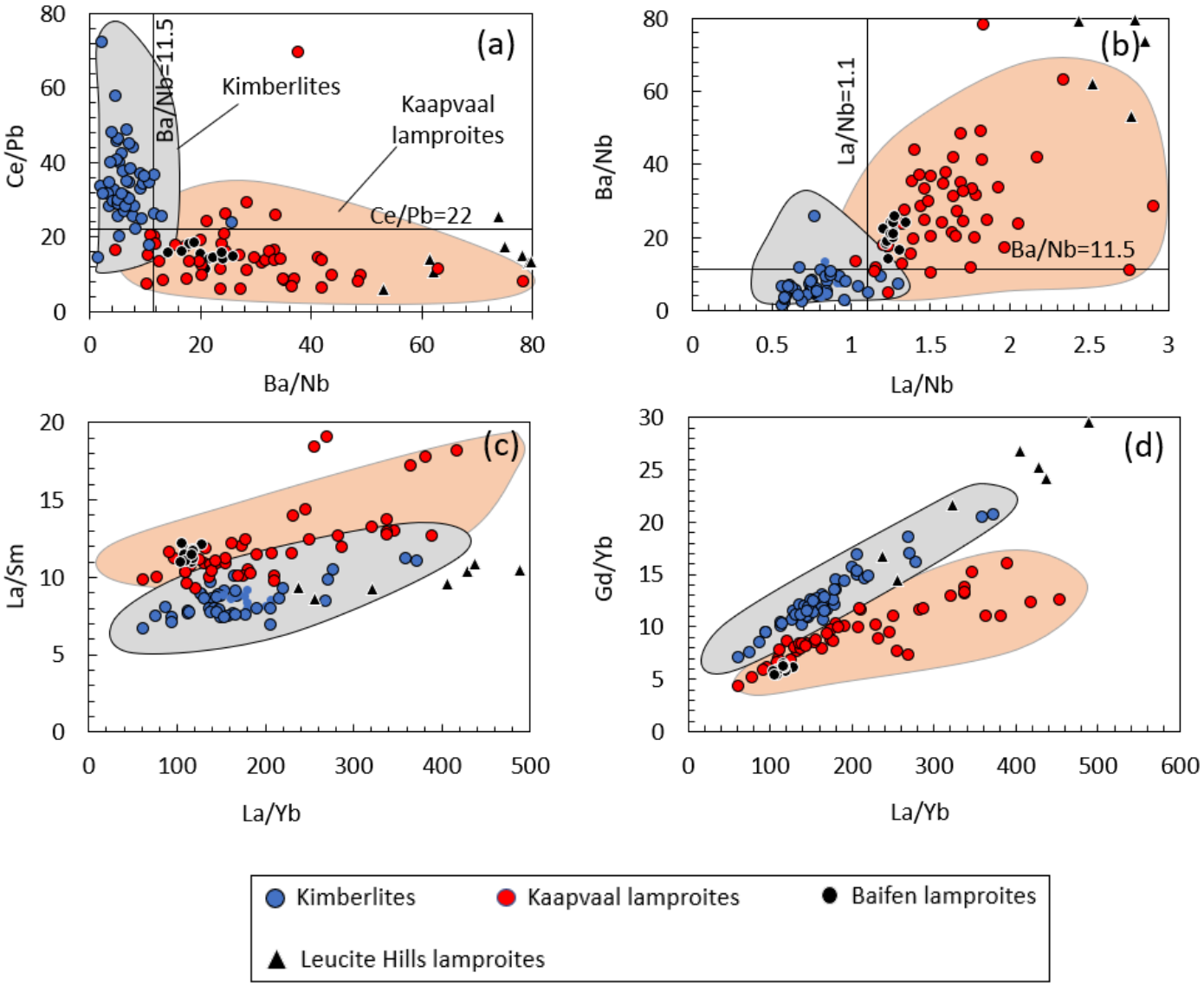

Figure 2. 8: Variation of (a) Ba/Nb vs Ce/Pb (b) La/Nb vs Ba/Nb (c) La/Yb vs La/Sm (d) La/Yb vs Gd/Yb for kimberlites (Becker and Le Roex, 2006; Le Roex et al., 2003; Harris et al., 2004), Kaapvaal lamproites (Becker and Le Roex, 2006; Coe et al., 2008), and Leucite Hills and Baifen lamproites (Mirnejad and Bell, 2006; Xiang et al., 2020). The gray fields represent kimberlite, and the orange fields represent Kaapvaal lamproites compiled using the same data as presented above.

Evolved varieties of Kaapvaal lamproites

With regards to fractional crystallization control on Kaapvaal lamproite magma evolution, as discussed in sections 1 and 2.2, compositions of these magmas evolve and crystallize "evolved mineral assemblages" including leucite, sanidine, K-richterite, and aegirine when undergo intense fractionation (Becker and Le Roex, 2006; Mitchell, 1995; Howarth et al., 2011). The evolved varieties of Kaapvaal lamproites have been considered as a petrographic group more distinct from kimberlites and interpreted as being relatively more SiO_2-rich than the unevolved group as a consequence of the occurrence of richterite in the groundmass (e.g., Tainton, 1992). The evolved group of Kaapvaal lamproites is more enriched in Al_2O_3 and depleted in MgO and volatiles compared to unevolved Kaapvaal lamproites (Figure 2.9a) (Tainton, 1992; Mitchell, 1995). Moreover, they have higher contents of Na_2O than unevolved varieties, which have been interpreted to be a consequence of low-temperature alteration of leucite and sanidine (Figure 2.9b) (e.g., Mitchell, 1995; Tainton, 1992).

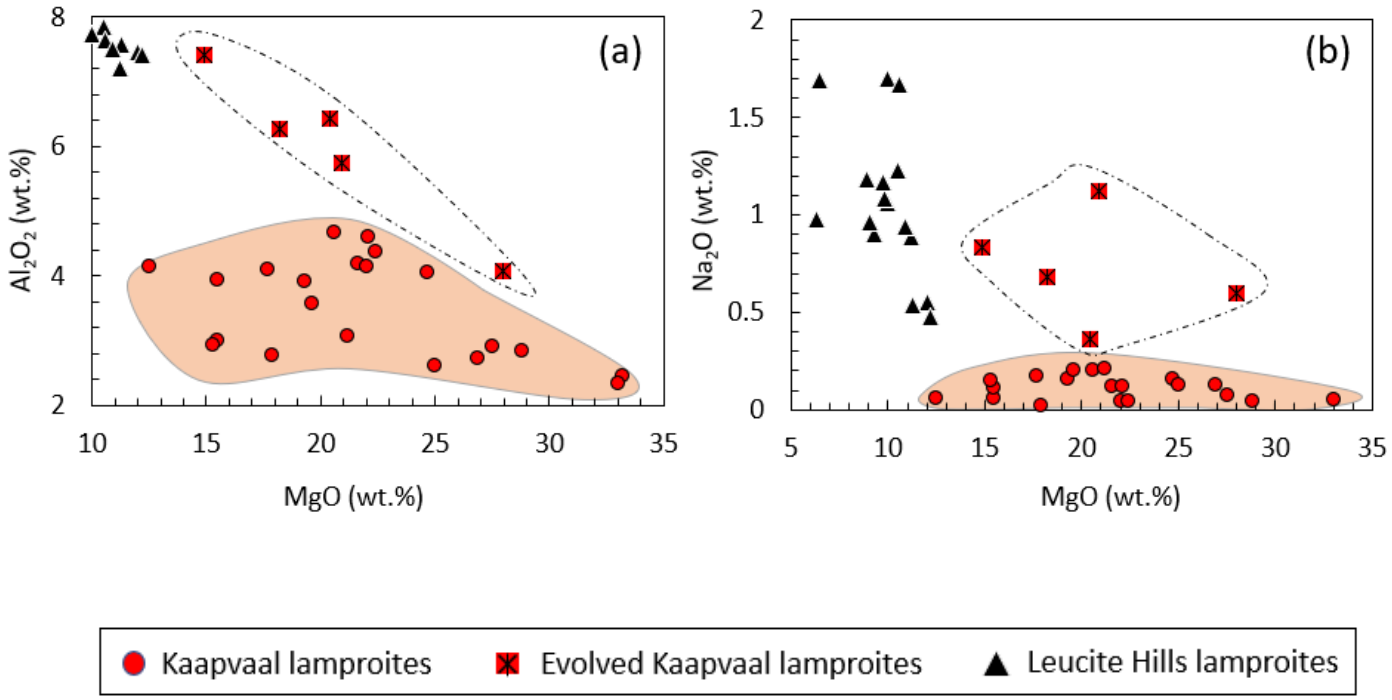

Figure 2. 9: Plots of Al_2O_3 and Na_2O versus MgO for lamproites (Mirnejad and Bell, 2006), Kaapvaal lamproites (Data source: Coe et al., 2008), and evolved Kaapvaal lamproites (Tainton, 1992 and Skinner et al., 1994). The orange fields represent Kaapvaal lamproites Swartruggens and Star, compiled using Coe et al. (2008) data. Dotted fields represent evolved Kaapvaal lamproites from Sover North, Postmasburg, Pniel, Brandewynkuil, and Slypsteen compiled using average major elements data of Tainton (1992) and Skinner et al. (1994)

CHAPTER 3: SAMPLE PREPARATION AND ANALYTICAL TECHNIQUES

3.1 Sample preparation

A total of 13 samples (labelled KRV 2, KRV 3, KRV 4, KRV 5, KRV 6, KRV 7, KRV 8, KRV 9, KRV 10, KRV 11, KRV 12, KRV 13, and KRV 14) collected from the Kareevlei diamond mine were cut and thin sectioned at the University of Cape Town (UCT) for petrographic and electron probe micro-analyses (EPMA). All these samples were first examined using a Zeiss petrographic microscope housed at UCT, and samples were divided into two varieties based on the presence and/or absence of leucite and K-richterite (see Table 3.1 below). For bulk-rock geochemistry, the rock samples were crushed into small chips of about 3 to 5 mm in size using the jaw crusher. Then the fresh rock chips were handpicked to avoid foreign materials such as crustal xenoliths and any other material that is not kimberlite related. Handpicked fresh rock chips were then milled with a Siebtechnik carbon steel swing mill to produce a powder of approximately 20 g.

Table 3. 1: Kareevlei pipe samples divided based on the presence or absence of leucite and K-richterite.

leucite-richterite types	**phlogopite-diopside types**
KRV 2	KRV 5
KRV 3	KRV 6
KRV 4	KRV 7
	KRV 8
	KRV 9
	KRV 10
	KRV 11
	KRV 12
	KRV 13
	KRV 14

3.2 Electron probe microanalyses (EPMA)

Phlogopite and K-richterite analyses

These analyses were conducted using a CAMECA SX 100 Electron Microprobe housed at the University of Johannesburg (UJ). For both phlogopite and K-richterite, the beam was accelerating at 15 kV with the beam current and diameter of 15 nA and 5 μm respectively, and the on-peak counting time per element of 10 to 50 s, depending on the element. The calibration standards for both phlogopite and K-richterite were measured at their Kα lines, except for Ba which was measured at Lα lines. Calibration standards are as follow: F (Kα, fluorite), Cl (Kα, NaCl), Na (Kα, jadeite), Al (Kα, almandine), Si (Kα, diopside), K (Kα, orthoclase), Ca (Kα, wollastonite), Ti (Kα, TiO_2), Cr (Kα, Cr_2O_3), Mn (Kα, rhodonite), Fe (Kα, hematite), and Ba (Lα, barite).

Diopside analyses

The analyses of diopside were also performed at UJ using the CAMECA SX 100 Electron Microprobe Analyser. The beam was accelerating at 20 kV with a beam current of 20 nA and a beam diameter of 2 μm. The on-peak counting time per element was 16–40 s depending on the element. Calibration standards for diopside are as follows: Na (jadeite), Mg (olivine), Al (almandine), Si (diopside), K (orthoclase), Ca (wollastonite), Ti (TiO_2), Cr (Cr_2O_3), Mn (rhodonite), and Fe (hematite). All the elements were measured on Kα lines.

3.3 X-Ray Fluorescence (XRF) analyses

The major element concentrations were measured using an X-Ray Fluorescence (XRF) instrument housed at Stellenbosch University. Sample powders were prepared as fused glass disks and used to measure the major elements. The sample powder preparation went as follows: 2 g of sample powder was placed into a ceramic crucible and dried overnight at 110 ° C in an oven. Once dried, the samples were weighed again to calculate the water content adsorbed (H_2O wt.%), and the dried powders were then heated in an oven of 900 ° C for a minimum of four hours to extract all the unwanted volatiles including H_2O and CO_2. After 4 hours of heating, the sample powders were then placed into a desiccator and cooled for a minimum of two hours. Once cooled, sample powders were weighed again to determine the weight percentage lost on ignition (LOI wt.%).

To prepare fused disks for XRF analyses, 0.7g of prepared powdered sample was added to 6g of Claisse XRF flux, and then the 0.7 g sample powder + 6 g Claisse XRF flux was melted and homogenized in the Claisse M4 Fluxer. The homogeneous melt was then poured into a hot platinum mould to cool and solidify, producing a fused glass disk ready to be placed in an XRF. The PANalytical XRF spectrometer was calibrated with the popular standards (e.g., BE-N, JB-1, and BHVO-1), which were prepared in the same manner as the samples being analyzed.

3.4 Inductively coupled plasma-mass spectrometry (ICP-MS) analyses.

A total of 13 samples and the SARM-39 standard were analyzed for a group of trace elements concentrations using the Thermo-Fisher iCAP RQ quadrupole ICP-MS housed in the UCT Geological Sciences Department. The analyzed elements were Li, Sc, V, Cr, Co, Ni, Cu, Zn, Rb, Sr, Y, Zr, Nb, Ba, La, Ce, Pr, Nd, Sm, Eu, Tb, Gd, Dy, Ho, Er, Tm, Yb, Lu, Hf, Ta, Pb, Th, and U, and their concentrations are presented in parts per million (ppm). To prepare for ICP-MS analyses, 50 mg of sample powder was weighed out and placed into 5 ml Teflon vials, in which 4 ml of a 4:1 mixture of concentrated hydrofluoric acid (HF) and nitric acid (HNO_3) was added. The Teflon vial was then closed and moved into the Teflon capsule of a steel Parr digestion vessel, and 2 ml of pure water was poured into the outer vessel to minimize the pressure difference between the outer Teflon and inner Teflon.

The steel Parr digestion vessels were firmly sealed and put into a 200 ° C oven for 24 hours to allow complete digestion. Once completely digested, the 3 ml Teflon vial was expelled from the capsule, and the cap was cautiously removed and put on a hot plate at 100 ° C to allow the evaporation of the acid mixture, followed by the addition and subsequent evaporation of 2 ml of pure nitric acid (HNO_3). After complete acid evaporation, the samples were then diluted using a stock solution of 5% HNO_3 containing 10 ppb of In, Bi, Re, and Rh used as internal standards. Calibration curves were obtained using artificial multi-element standard solutions.

3.4 Sr–Nd isotope analyses

The Sr–Nd isotope analyses were performed using the Nu-Plasma HR Multi-collector Inductively Coupled Plasma Mass Spectrometer (HR MC-ICP-MS) at the UCT Department of Geological Sciences. Preparation for MC-ICP-MS analyses went as follows: 50 mg of sample powder was digested in concentrated 2M HNO_3 at 140 ° C for 48 hours in closed 7 ml Teflon beakers. Once digested, the samples were then dried and redissolved in 1.7 ml of 2M HNO_3 for the elemental separation of Sr and Nd. The sequential column chemistry outlined by Mikova and Denkova (2007) was followed when separating Sr and Nd.

The measured $^{87}Sr/^{86}Sr$ isotope ratios were analysed as 200 parts per billion (ppb) 0.2% HNO_3 solutions, with NIST SRM-987 and an $^{87}Sr/^{86}Sr$ normalising value of 0.710255 as reference standards. For the correction of instrumental mass fractionation, the exponential law and an $^{86}Sr/^{88}Sr$ value of 0.1194 was used. Measured Nd isotope ratios were analysed as 50 ppb 2% HNO_3 solutions plus JNdi-1 and a $^{143}Nd/^{144}Nd$ normalising value of 0.512115 as reference standards. To correct all the Nd isotope data, the natural Sm and Ce isotope abundances and measured signals for ^{147}Sm and ^{140}Ce were used. For the correction of instrumental mass fractionation, the exponential law and a $^{146}Nd/^{144}Nd$ value of 0.7219 was used.

CHAPTER 4: RESULTS

4.1 Petrography

The Kareevlei lamproite is characterized by abundant phlogopite (32–58 vol.%), diopside, and alkali-rich phases in the groundmass, including K-richterite and leucite, along with interstitial material which is predominantly clay mineral alteration and sometimes contains fine-grained carbonate (could be calcite). The mineralogy of the Kareevlei samples analysed in this study varies significantly and the samples are divided into two types: leucite-richterite and phlogopite-diopside lamproites. A summary of all samples with modal abundances and classification is presented in Table 4.1.

Table 4. 1: Mineralogical characteristics and modal abundances of lamproites from Kareevlei.

Classification (type)	**Olivine modes (vol.%)**		**Matrix and accessory minerals**
and Samples ID	**Microcrysts**	**Macrocrysts**	
Leucite-richterite			
KRV2	5	7	*Phl (56 vol.%), Lct (27 vol.%), K-richt (17 vol.%), Diop (26 vol.%), Alt (1 vol.%)*
KRV3	3	7	*Phl (40 vol.%), Lct (12 vol.%), Sanid (7 vol.%), K-richt (25 vol.%), Diop (16 vol.%), Alt (15 vol.%)*
KRV4	8	11	*Phl (58 vol.%), Diop (17 vol.%), K-richt (3 vol.%) Alt (18 vol.%)*
Phlogopite-diopside			
KRV5	10	3	*Phl (36 vol.%), Diop (29 vol.%), Alt (25 vol.%)*
KRV6	19	8	*Phl (32 vol.%), Diop (23 vol.%), Alt (19 vol.%)*
KRV7	18	9	*Phl (44 vol.%), Diop (16 vol.%), Alt (13 vol.%)*
KRV8	16	5	*Phl (48 vol.%), Diop (12 vol.%), Alt (19 vol.%)*
KRV9	9	3	*Phl (47 vol.%), Diop (36 vol.%), Alt (5 vol.%)*
KRV10	9	4	*Phl (53 vol.%), Diop (27 vol.%), Alt (5 vol.%)*
KRV11	9	6	*Phl (56 vol.%), Diop (17 vol.%), Alt (12 vol.%)*
KRV12	15	12	*Phl (50 vol.%), Diop (19 vol.%), Alt (5 vol.%)*
KRV13	10	3	*Phl (40 vol.%), Diop (16 vol.%), Alt (5 vol.%)*
KRV14	10	3	*Phl (56 vol.%), Diop (27 vol.%), Alt (3 vol.%)*

(Phl) Phlogopite, (Lct) Leucite, (Diop) Diopside, (Sanid) Sanidine, (K-richt) K-richterite, (Alt) Alteration

4.1.1 Kareevlei leucite-richterite lamproite

The leucite-richterite samples consist of highly altered olivine macrocrysts (0.5–2.5 mm) and microcrysts (0.2–0.3 mm) in a groundmass of phlogopite (40–57 vol.%), diopside (16–26 vol.%), K-richterite (3–25 vol.%), leucite (7–27 vol.%), and an interstitial material (1–25 vol.%) comprising fine-grained alteration material which could be carbonate minerals, calcite and serpentine. Olivine is highly altered to a variety of fine-grained materials including carbonate minerals; no fresh olivine was identified. These olivines can be identified by morphology and size even though they are always altered. The macrocrystic olivines (0.5–0.9 mm) in these rocks are dominantly subhedral whereas the olivine microcrysts (0.1–0.4 mm) are generally anhedral and difficult to identify due to alteration as they commonly blend in with the fine-grained altered interstitial material. All these olivines are commonly mantled by groundmass phlogopite (Figure 4.1a). Oxides such as spinel and perovskite are common constituents in kimberlites, however, spinel or perovskite are absent in the Kareevlei lamproites.

Two textural associations of phlogopite are identified as (1) Macrocryst laths (0.3–0.9 mm in length) that display distinct zoning defined by pleochroic orange-brown to pale–brown cores to distinct darker brick-red rims, typically 0.02 mm wide. Phlogopite rims host inclusions of diopside laths in some cases. (2) Poikilitic phlogopite plates (0.3–0.5 mm across) host inclusions of pseudomorphed leucite (spherical crystals) and diopside laths (Figure 4.1b). Poikilitic phlogopite is characterized by weak pleochroism ranging from pale orange-brown to darker orange–brown. The poikilitically enclosed spherical pseudo-leucites are 0.05–0.1 mm in size, and diopside laths are approximately 0.06 – 0.1 mm.

Diopside and pseudo-leucite are distributed throughout the groundmass of these rocks. Diopside grains occur as colorless elongated prisms and/or laths, generally, 0.2–0.5 mm in length varying from coarse-grained subhedral crystals (0.3–0.5 mm) and blocky prisms (0.3 mm length × 0.2 mm width) to fine-grained laths (0.1 mm length and < 0.1 mm width). Under cross-polarized light (XPL), the diopsides are characterized by high birefringence and inclined extinction. Leucite is present as pseudomorphed spherical, colorless, or light-gray grains (0.1–0.3 mm) with abundances of 7–27 vol.% and is highly altered to irregular gray patches in the groundmass (Figure 4.1c, e, g, and h). These pseudo-leucites are present in some cases as mantles to K-richterite in the groundmass and rarely occur as inclusions in the K-richterite. Colorless/white irregular patches in the interstitial material are observed adjacent to highly altered leucite patches. These patches are partly altered, exhibit low first-order birefringence under XPL, and may be sanidine. K-richterite (14–30 vol. %) is characterized by pale green to brown-pink pleochroism with distinct darker green-brown margins and two distinct cleavage planes intersecting at 60^{o} (Figure 4.1e). This occurs as irregular patches and plates (0.1 – 0.3 mm) in the groundmass and is consistently mantled by phlogopite and pseudo-leucite (Figures 4.1c, e, f, g, and h). The interstitial material in the groundmass is at abundances of 1 – 15 vol.%, and comprises calcite and secondary phases such as clay minerals (Figure 4.1d).

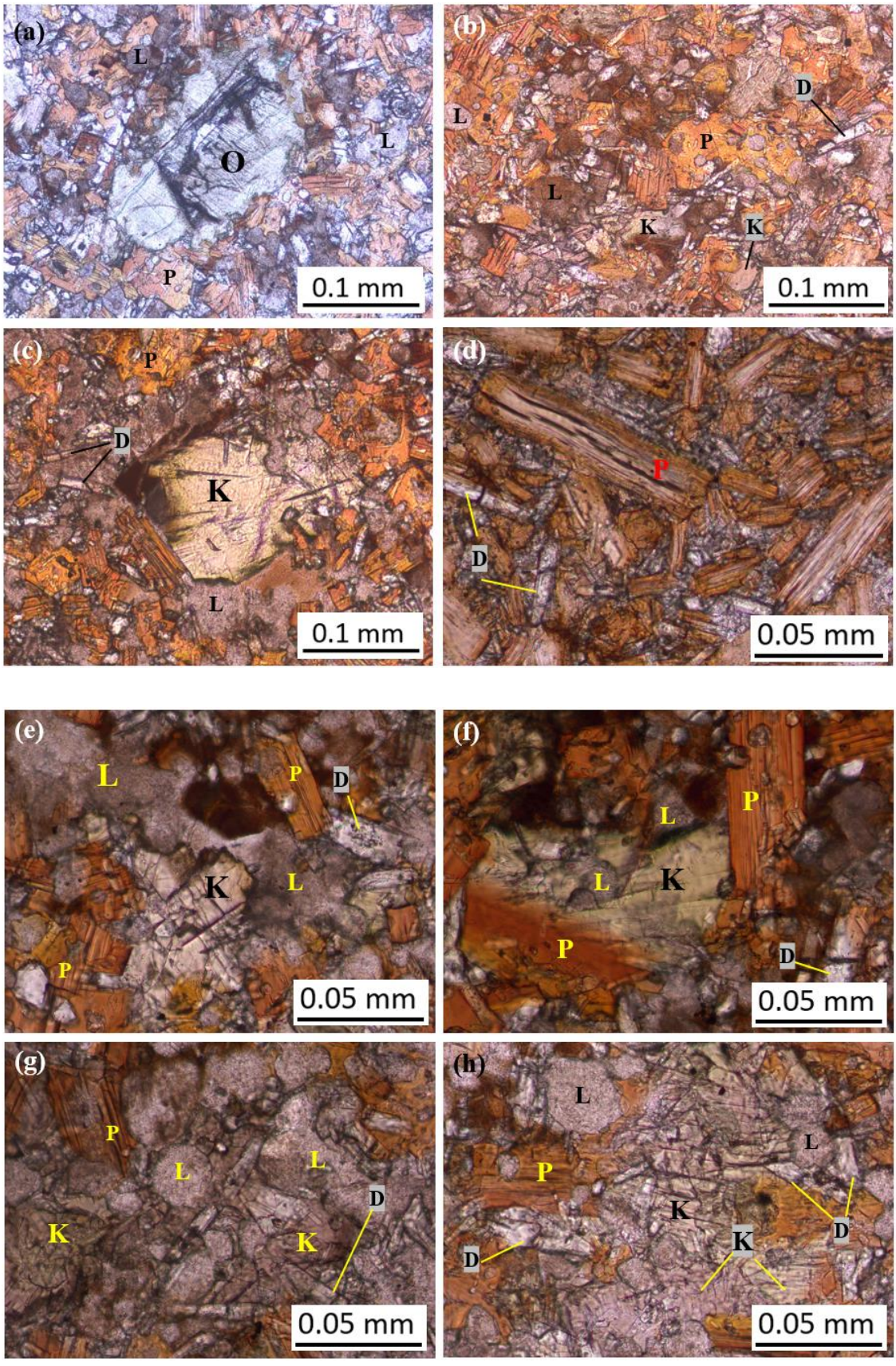

Figure 4. 1: Kareevlei leucite-richterite lamproite microphotographs. (a) Altered subhedral olivine macrocryst mantled by fine-grained brownish poikilitic phlogopite. (b) Groundmass of spherical pseudo-leucites and diopside crystals poikilitically enclosed in the groundmass phlogopite. (c) Pale-green K-richterite mantled by a patch of light gray altered leucite and fine-grained groundmass phlogopite. (d) Zoned phlogopite laths and diopside laths hosted in carbonate-mesostasis. (e) and (f): K-richterite plates mantled by poikilitic phlogopite and leucite. (g) and (h): K-richterite mantled by groundmass phlogopite and leucite. Note, D = Diopside, K = K-richterite, L = Leucite, O = Olivine, P = Phlogopite.

4.1.2 Kareevlei phlogopite-diopside lamproite

The phlogopite-diopside samples are characterized by the complete absence of K-richterite and leucite in the groundmass and have relatively abundant microcrystic olivines (9–19 vol.%) compared to the leucite-richterite samples (3–8 vol%), whereas the macrocrysts are relatively low in abundance (7–11 vol.%). Both olivine macrocrysts (0.5–2.3 mm) and microcrysts (0.2–0.4 mm) in these rocks are subhedral to anhedral although they are consistently altered and mantled by groundmass tetraferriphlogopite (Figure 4.2c). The olivine microcrysts commonly blend within the fine-grained interstitial alteration material and can be hard to identify due to high alteration (Figure 4.2e).

Phlogopite occurs in two textural forms as in leucite-richterite samples. 1) Phlogopite laths (0.2–0.9 mm) characterized by zonation defined by weak pleochroic pale brown to darker orange-brown cores and strong orange-brown rims that in places host inclusions of fine-grained diopside laths (<0.1 mm). The phlogopite lath rims are as thin as 0.02 mm. Phlogopite laths in these samples may be set in interstitial carbonate and exhibit a flow-aligned texture (Figures 4.2a and b). (2) Poikilitic phlogopite plates (0.2 – 0.8 mm) characterized by a weak pleochroism of light orange-brown to orange-brown and host abundant inclusions of diopside laths (0.1–0.4 mm). Anhedral and blocky diopside macrocrysts (0.3–0.8 mm) are present in the groundmass of these samples and are zoned in reflected light, with mottled cores and clean-textured rims (see Figures 4.2d and 4.7c). Some samples have relatively abundant interstitial carbonate (up to 25 vol.%) in the groundmass (Figures 4.2a and b).

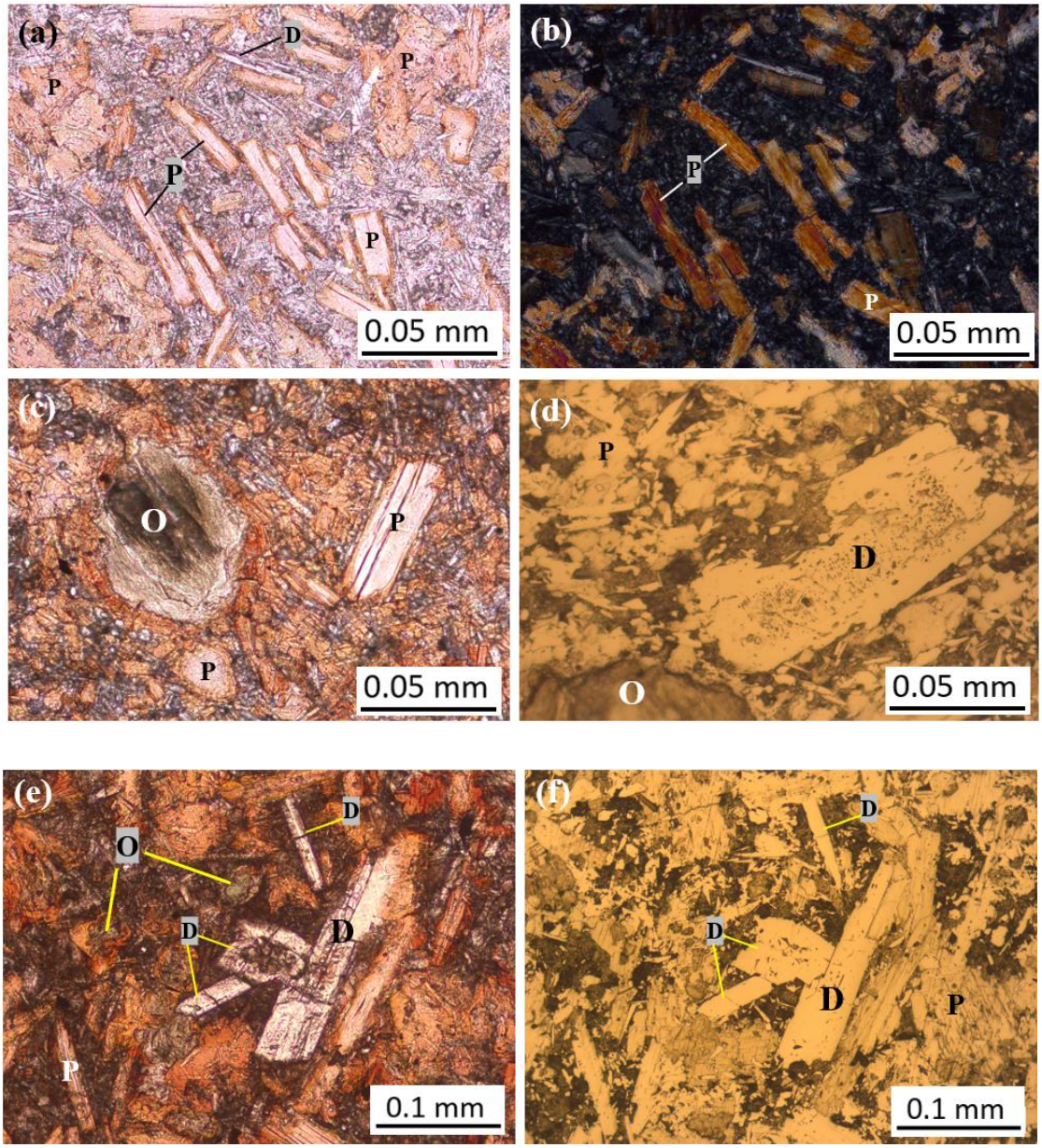

Figure 4. 2: Kareevlei phlogopite-diopside lamproite microphotographs: (a) and (b) Phlogopite laths and fine-grained diopside laths hosted in carbonate-mesostasis and groundmass phlogopite. (c) Olivine microcryst, phlogopite lath, and microcrystic diopside laths hosted in groundmass phlogopite. (d) Macrocrystic prismatic diopside hosted in the groundmass phlogopite. (e) and (f) Subhedral and prismatic diopsides, and altered microcrystic olivine hosted in the groundmass poikilitic phlogopite.

4.2 Mineral chemistry

4.2.1 Phlogopite compositions

Phlogopite was analyzed by EPMA in two leucite-richterite samples (KRV2 and KRV3) and four phlogopite-diopside samples (i.e., KRV5, KRV6, KRV9, and KRV12). Cores and rims of 10 to 12 grains were analyzed in each sample. Two textural types of phlogopite identified as zoned phlogopite laths and groundmass poikilitic phlogopite (see Figures 4.1b and d) were analyzed in the leucite-richterite samples. Only phlogopite laths were analyzed in phlogopite-diopside samples. All the results are presented in Figures 4.4 and 4.5. Phlogopite compositions in the different mineralogical types overlap and so are described together below. A full dataset of analyzed phlogopites is presented in Appendix 1.

The phlogopite laths display compositional zonation defined by cores and rims, which were identified by both petrography and Back-Scattered Electron (BSE) imaging (Figure 4.3 below). The Cr_2O_3 concentrations in the cores vary widely and two distinct Cr_2O_3 core populations are identified. 1) The low-Cr_2O_3 core population (Cr_2O_3 0.04–0.68 wt.%) mantled by TiO_2 and FeO-rich phlogopite rims (TiO_2 = 2.01–5.56 wt.%; FeO = 5.85 – 14.8 wt.%) relative to the cores (TiO_2 = 0.38–4.22 wt.%; FeO = 2.69–9.02 wt.%). The rims have Cr_2O_3 compositions that overlap with the low-Cr_2O_3 core population. 2) The high-Cr_2O_3 core population (0.89–1.97 wt.%) is clearly compositionally distinct from low-Cr_2O_3 cores and the rims (Figures 4.5c and d). Both of these core populations are mantled by rims of identical compositions which have Cr_2O_3 concentrations that vary from below detection to 0.53 wt.%. The MgO and Al_2O_3 compositions are similar in all the cores and decrease with increasing TiO_2 and FeO towards the rims (Figures 4.4a and b; Figures 4.5a and b).

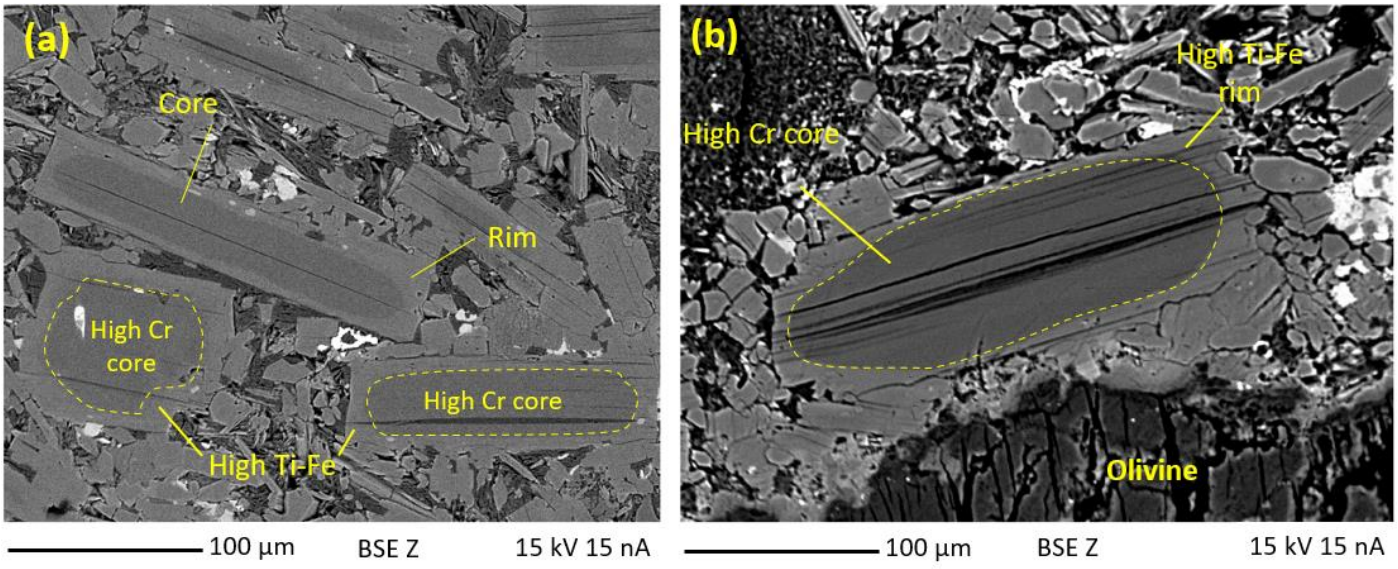

Figure 4. 3: BSE images of phlogopites from Kareevlei lamproite. These phlogopites are captured at a 100 µm scale (shown by a thin black line underneath each image) and characterized by darker cores and lighter rims.

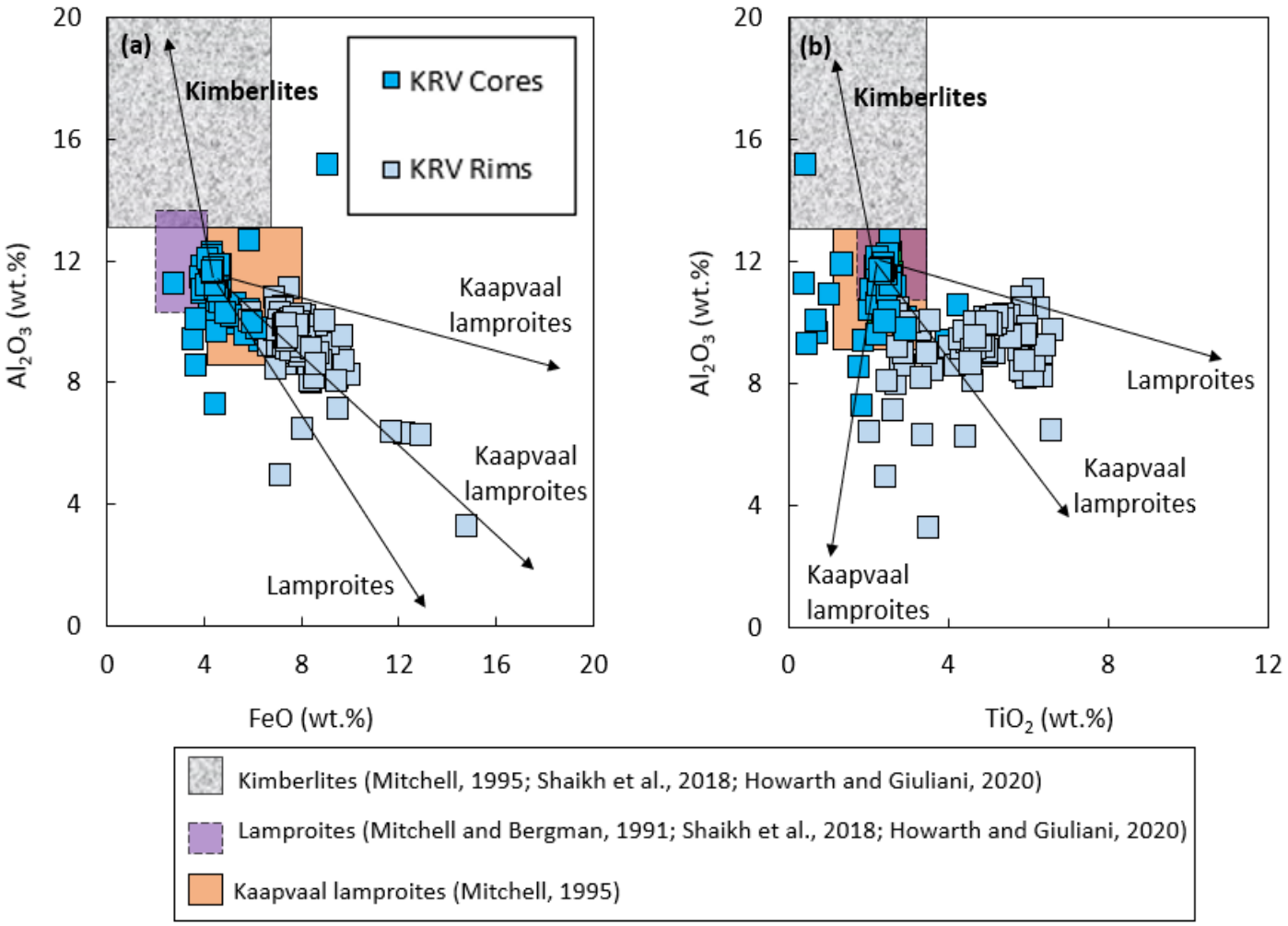

Figure 4. 4: The phlogopite compositional variation plots of Kareevlei lamproites compared to worldwide kimberlites and other lamproites. The arrows represent evolutionary trends of phlogopite in kimberlites and lamproites. The background fields represent phlogopite core compositions in kimberlites and lamproites, and the arrows are evolutionary trend from the core towards the rims.

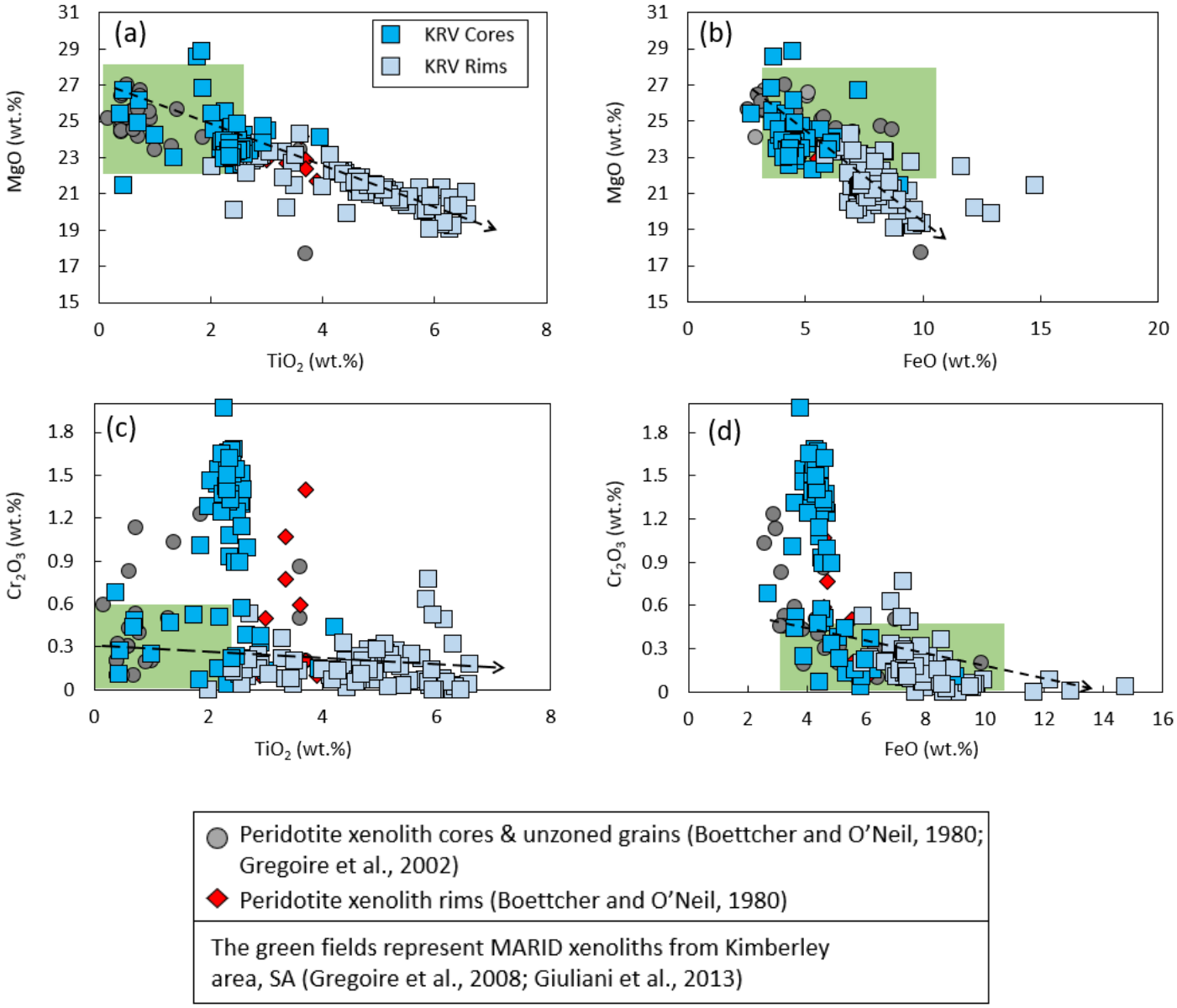

Figure 4. 5: Major oxide covariation plots for phlogopite grains from the Kareevlei lamproites compared to mantle xenoliths. Arrows represent the composition evolutionary trends from Kareevlei phlogopite cores to the tetraferriphlogopite overgrowths and poikilitic phlogopite plates. Note: KRV = Kareevlei.

4.2.2 K-richterite compositions

K-richterite was analyzed from one representative sample (KRV2) out of the three leucite-richterite samples and seven grains were analyzed. They are characterized by variable concentrations of TiO_2 (3.39–5.13 wt.%), K_2O (4.60–4.80 wt.%), FeO (5.36–8.87 wt.%), and Cr_2O_3 (below detection to 0.09 wt.%). A full set of K-richterite compositions is presented in Appendix 2. The Na_2O concentrations vary from 4.73 to 6.09 wt.% and positively correlate with FeO (Figure 4.6a). The compositions of these K-richterites show narrow ranges of Na/K ratios and Ti (Na/K = 1.52–1.94, and Ti = 0.35–0.54). Titanium and Na/K are clustered and show no correlation (Figure 4.6b).

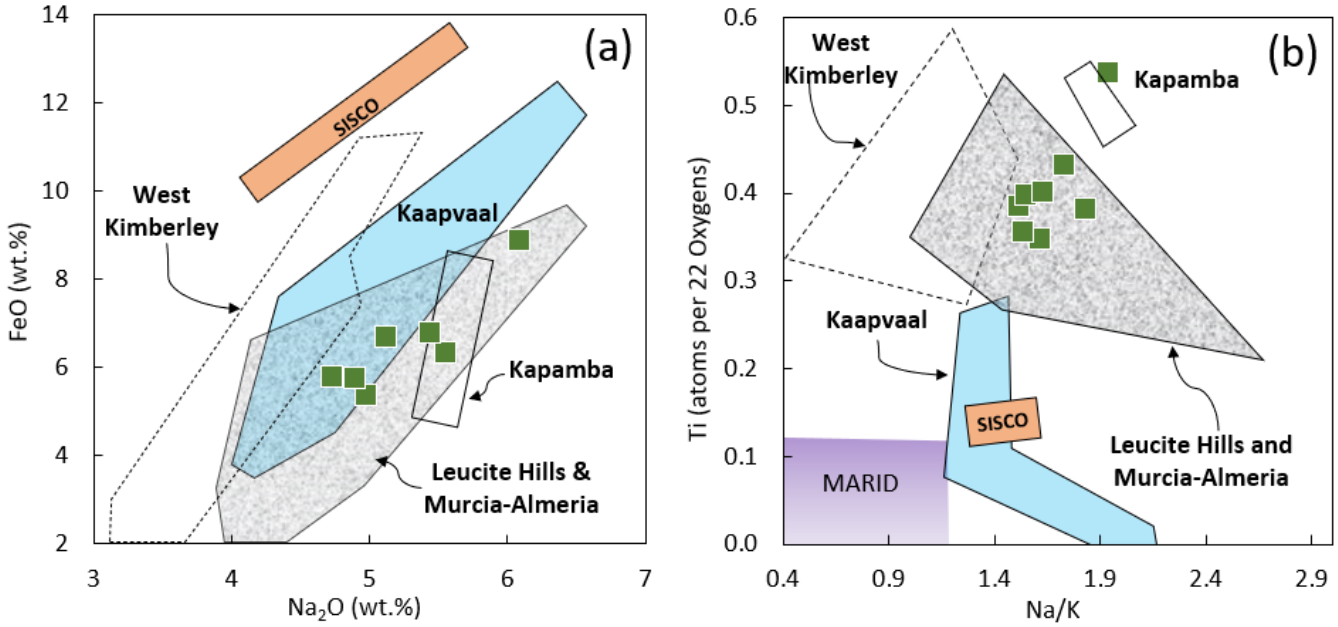

Figure 4. 6: Compositions of K-richterite from Kareevlei (green squares) on (a) Na_2O vs FeO and (b) Na/K vs Ti plots, compared to K-richterite in lamproites from West Kimberley (Mitchell and Bergman, 1991), Leucite Hills and Murcia-Almeria (Mitchell and Bergman, 1991), Sisco (Mitchell and Bergman, 1991), Kapamba (Mitchell, 1995), MARID (Dawson and Smith 1977), and Kaapvaal (from Pniel and Besterskraal) (Mitchell, 1995).

4.2.3 Diopside compositions

Diopside grains were analyzed from three representative samples; one sample was a leucite-richterite type (KRV2), and two samples were phlogopite-diopside type (KRV5 and KRV12). Seven to ten grains were analyzed from each sample. The majority of diopsides are unzoned subhedral and prismatic laths in the groundmass, characterized by concentrations of TiO_2 = 0.14–1.70 wt.%, Na_2O = 0.22–0.62 wt.%, Al_2O_3 = 0.09–1.25 wt.%, Cr_2O_3 = below detection to 0.89 wt.%, and CaO = 20.5–25.2 wt.%. A rare anhedral macrocrystic diopside (~0.5 mm) was also analyzed, which displayed distinct core-rim zonation (Figure 4.7c). The zonation is defined by a Al_2O_3- and FeO-rich (Al_2O_3 = 0.70–1.25 wt.%; FeO = 7.98–10.8 wt.%) and TiO_2-poor core (< 0.50 wt.%) relative to the rim (Al_2O_3 = 0.26–0.36 wt.%; FeO = 2.38–2.42 wt.%; TiO_2 = 0.90–1.03 wt.%) (Figures 4.7a and c). The full dataset of diopside compositions is presented in Appendix 3. The Ti (Ti atoms per 6 oxygens) varies from 0.02 to 0.04 and positively correlates with Al (Al atoms per 6 oxygens) (Figure 4.7b).

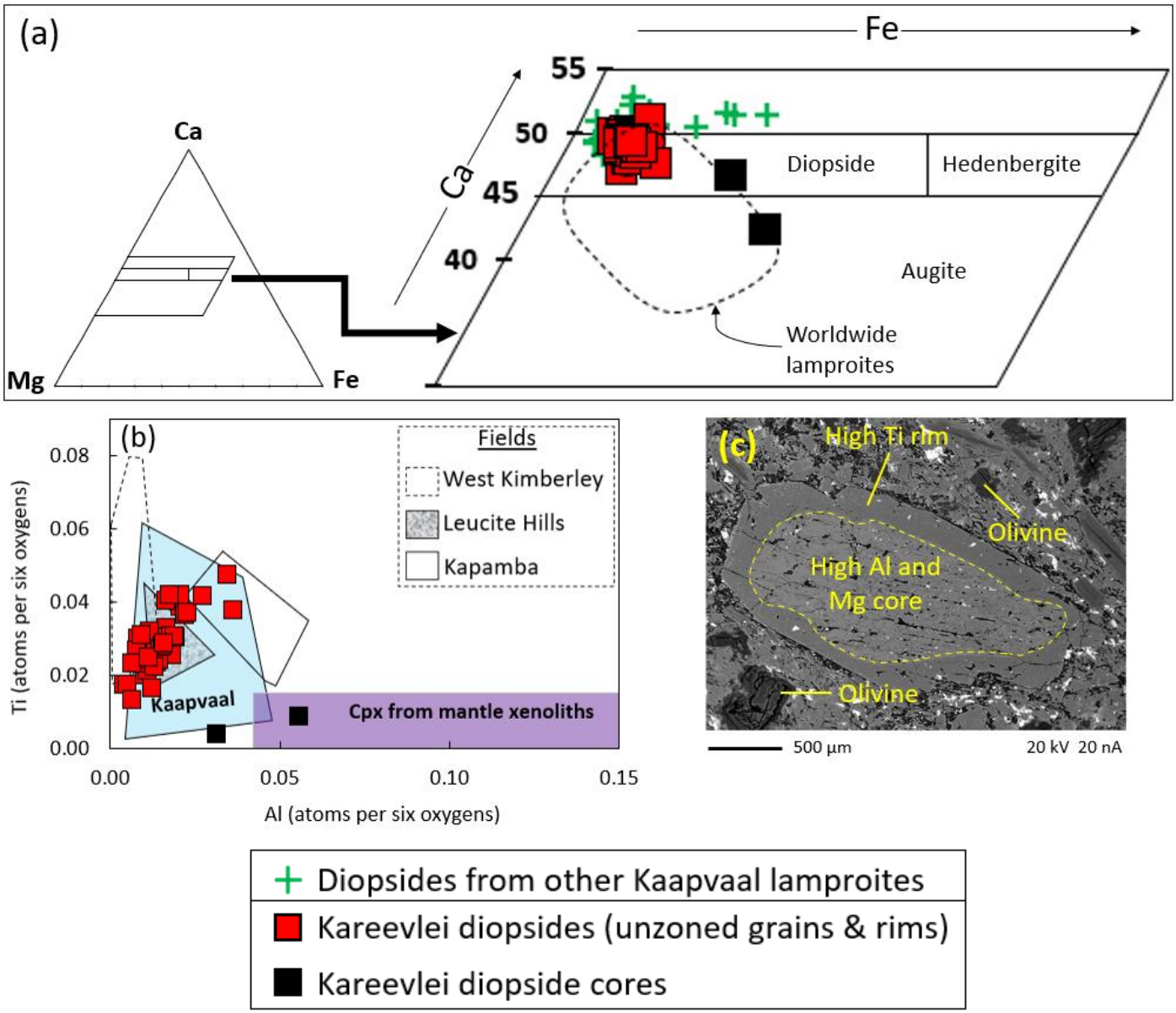

Figure 4. 7: Compositions of diopsides from Kareevlei lamproites on (a) Ca-Mg-Fe quadrilateral and (d) Al vs Ti plot, compared to compositions of diopsides from Australia, West Kimberley lamproites(Mitchell and Bergman, 1991; Jaques et al., 1986), Leucite Hills lamproites (Mitchell and Bergman, 1991), Kapamba lamproites (Scott et al., 1988), Kaapvaal lamproites (Mitchell, 1995), clinopyroxenes (cpx) from peridotites (Grégoire et al., 2002) and garnet lherzolite mantle xenoliths (Grégoire et al., 2003). The field of worldwide lamproites in the quadrilateral was compiled by Mitchell and Bergman (1991). Figures (c) is BSE image of the analyzed zoned diopside.

4.3 Bulk-rock geochemistry

A total of thirteen samples (see Table 2) from the Kareevlei lamproite were analyzed for major and trace elements as well as Sr-Nd isotopes, including samples of both the leucite-richterite (n = 3) and diopside-phlogopite (n = 10) types. A full dataset of major, trace elements and Sr-Nd isotope compositions are presented in Tables 4.2, 4.3, and 4.4.

4.3.1 Major elements geochemistry

The Kareevlei lamproite samples show distinct geochemical compositions between the two identified varieties. The leucite-richterite types are characterized by higher concentrations of SiO_2 (44.8–47.9 wt.%), Al_2O_3 (6.34–7.34 wt.%), Na_2O (0.78–1.99 wt.%), and lower MgO concentrations (MgO = 16.2–17.1 wt.%) relative to the phlogopite-diopside types (SiO_2 = 40.8–42.9 wt.%; Al_2O_3 = 5.44–6.22 wt.%; Na_2O = 0.42–0.74 wt.%; MgO = 20.7–23.0 wt.%). Titanium and K_2O concentrations in these varieties (i.e., both leucite-richterite and phlogopite-diopside types) are similar (TiO_2 = 1.85–2.25 wt.%; K_2O = 4.49–6.75 wt.%) (Figure 4.8c).

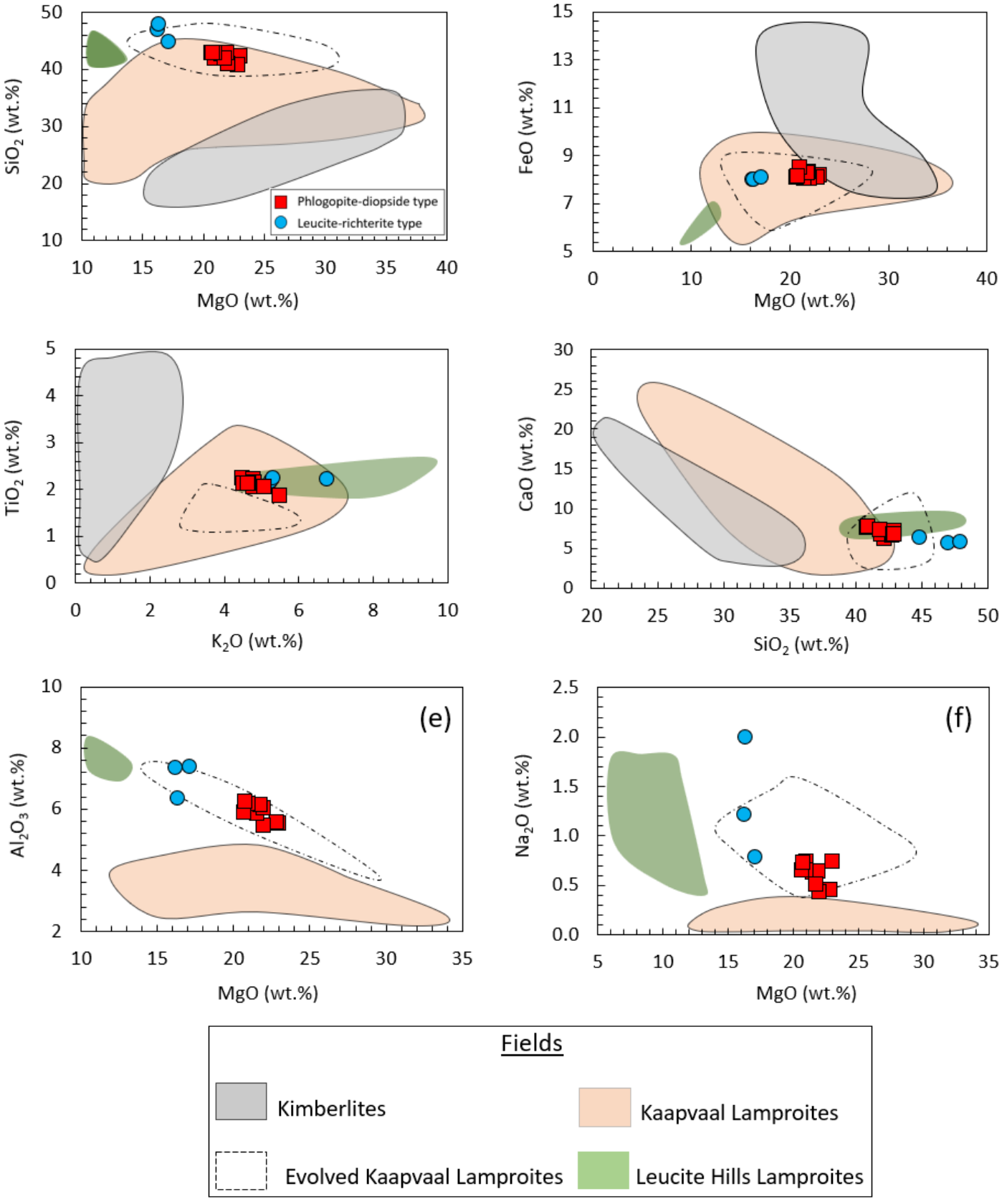

Figure 4. 8: Variation plots of selected major elements of Kareevlei lamproites in comparison with kimberlites (Becker and Le Roex, 2006; Le Roex et al., 2003), Kaapvaal lamproites (Becker and Le Roex, 2006; Coe et al., 2008), Leucite Hills Lamproites (Mirnejad and Bell, 2006). The dotted fields of evolved sub-group of Kaapvaal lamproites from Sover North, Postmasburg, Pniel, Brandewynkuil, and Slypsteen (Mitchell, 1995).

Table 4. 2: Major element compositions of Kareevlei samples (in wt.%).

	Leucite-richterite samples			Phlogopite-diopside samples									
Sample ID	**KRV 2**	**KRV 3**	**KRV 4**	**KRV 5**	**KRV 6**	**KRV 7**	**KRV 8**	**KRV 9**	**KRV 10**	**KRV 11**	**KRV 12**	**KRV 13**	**KRV 14**
SiO_2	47.0	47.9	44.8	42.2	40.8	40.9	41.9	42.7	42.9	41.8	42.8	42.9	42.9
TiO_2	2.16	2.25	2.22	2.24	2.12	2.12	2.21	2.06	2.14	1.85	2.12	2.12	2.06
Al_2O_3	7.34	6.34	7.38	5.54	5.55	5.44	5.92	5.86	6.03	6.13	6.17	5.89	6.22
Fe_2O_3	7.99	8.01	8.08	8.20	8.11	8.02	8.33	8.05	8.32	8.26	8.50	8.09	8.12
MnO	0.13	0.12	0.11	0.12	0.16	0.17	0.13	0.14	0.15	0.14	0.14	0.13	0.14
MgO	16.2	16.4	17.1	23.0	22.8	22.0	21.0	21.5	21.9	21.8	21.0	20.7	20.8
CaO	5.71	5.72	6.38	6.25	7.59	7.76	6.69	6.68	7.17	7.37	6.79	6.73	6.70
Na_2O	1.22	1.99	0.78	0.74	0.46	0.42	0.74	0.63	0.64	0.51	0.65	0.65	0.73
K_2O	5.24	5.32	6.75	4.49	4.72	4.52	4.79	4.77	4.80	5.50	4.66	4.63	5.08
P_2O_5	0.44	0.64	1.36	0.90	1.74	1.93	1.51	1.21	1.17	1.60	1.02	1.34	1.20
SO_3	b.d.	0.05	0.01	b.d.	b.d.	b.d.	b.d.	b.d.	b.d.	b.d.	b.d.	b.d.	b.d.
Cr_2O_3	0.12	0.13	0.13	0.14	0.15	0.14	0.15	0.16	0.15	0.16	0.18	0.14	0.14
NiO	0.06	0.07	0.06	b.d.	b.d.	b.d.	b.d.	b.d.	b.d.	b.d.	b.d.	b.d.	b.d.
H_2O-	1.40	0.83	0.49	b.d.	b.d.	b.d.	b.d.	b.d.	b.d.	b.d.	b.d.	b.d.	b.d.
LOI	3.83	3.52	3.35	5.98	4.98	5.70	5.71	5.40	3.57	4.02	5.11	5.68	4.97
Total	98.8	99.3	99.1	99.8	99.2	99.2	99.1	99.2	99.0	99.2	99.1	99.0	99.0

Note: b.d = below detection; LOI = loss of ignition.

4.3.2 Trace element geochemistry

The full dataset of trace elements compositions is presented in Table 6. The first-period transition metals such as Ni and Cr have slightly varying concentrations of Ni = 451–689 ppm and Cr = 798–1 078 ppm. Nickel and Cr exhibit a positive correlation with MgO, with the phlogopite-diopside samples having relatively high concentrations of Ni, Cr, and MgO compared to the leucite-richterite samples (Figures 4.9a and b). Nickel shows narrow variations within each type of lamproite, i.e., in leucite-richterite (Ni = 451–585 ppm) and phlogopite-diopside samples (Ni = 559–689 ppm).

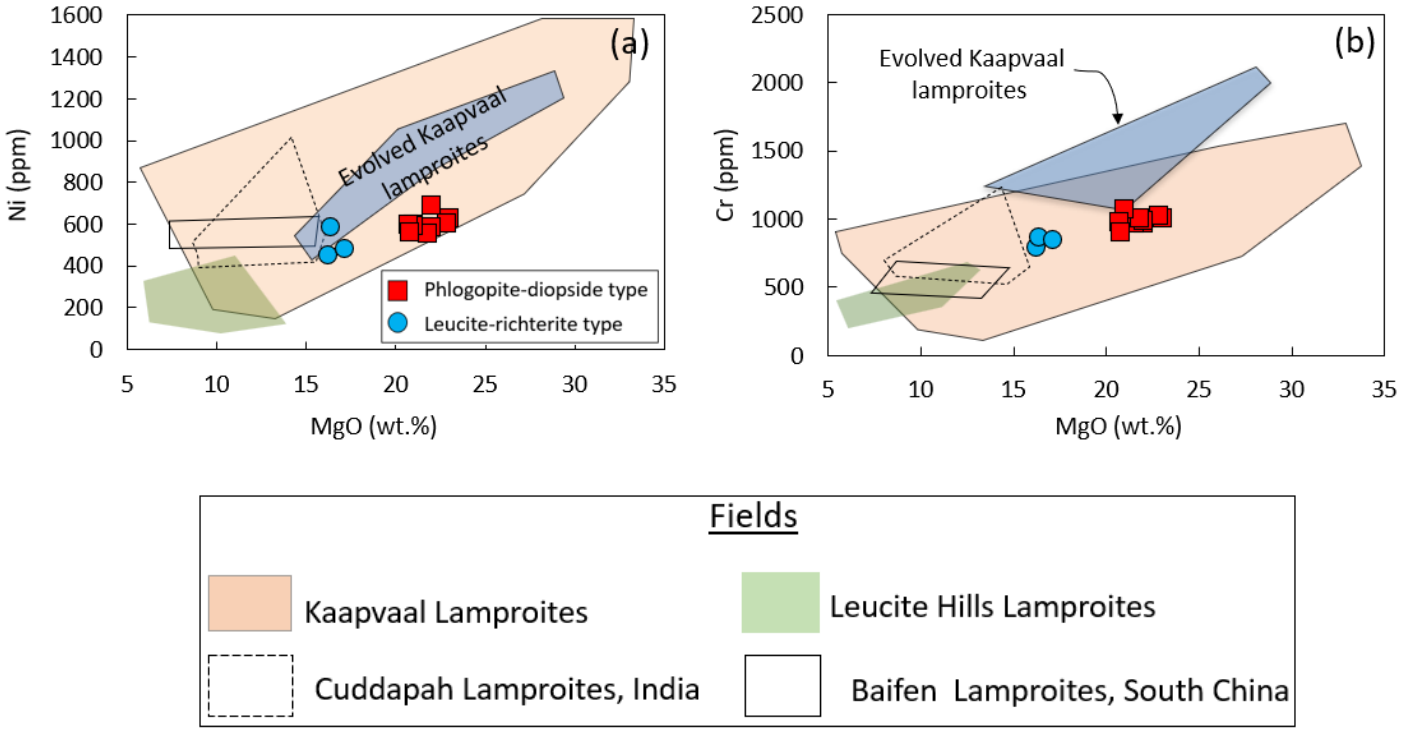

Figure 4. 9: The bivariate plots of Ni and Cr against MgO for Kareevlei lamproites samples in comparison with Kaapvaal lamproites (Becker and le Roux, 2006), including the evolved subgroup of Kaapvaal lamproites from Sover North, Postmasburg, Pniel, Brandewynkuil, and Slypsteen (Mitchell, 1995); Leucite Hills lamproites (Mirnejad and Bell, 2006); Baifen lamproites, South China (Xiang et al., 2020); Cuddapah lamproites, India (Chalapathi-Rao et al., 2004).

The Kareevlei lamproites exhibit distinct compositions of immobile incompatible elements (e.g., La) in which the phlogopite-diopside types are more enriched (La = 267–230 ppm) than the leucite-richterite types (La = 155–196 ppm). Large ion lithophile elements such as Rb, Pb, and Sr in these lamproites positively correlate with La, with the phlogopite-diopside type being slightly enriched in Rb, Pb, and Sr (Rb = 198–250 ppm; Pb = 27.5–40.6 ppm; Sr = 2077–2698 ppm) compared to the leucite-richterite type (Rb = 118–211 ppm; Pb = 13.1 – 29.0 ppm; Sr = 958–1370 ppm) (see Figures 4.10b, c, and d). The Ba concentrations appear similar in both types varying widely from 1890 up to 5472 ppm and show no correlation with La (Figure 4.10a). In general, the LILE positively correlate with La except for Ba. Rubidium (Rb) when plotted against K_2O varies widely and shows slightly scattered distributions, with the leucite-richterite type being slightly more enriched in K_2O than the phlogopite-diopside type (Figure 4.10e).

The HFSE (e.g., Nb and Th) positively correlate with immobile incompatible elements (e.g., La) (Figure 4.11g and h), whereas Zr and Hf are nearly constant at widely varying La (Figure 4.11e and f). Hafnium when plotted against Zr does not show correlation, and samples are clustered in a small area (Figure 23c). The HFSE in the lamproite types have similar compositions and exhibit narrow ranges of Ta = 3.81–4.85 ppm, Hf = 11.5–13.7 ppm, and Zr = 456–553 ppm. However, the leucite-richterite type appears to have distinctly lower Th and Nb concentrations (Th = 22.5–23.8 ppm; Nb = 85.5–89.0 ppm) than the phlogopite-diopside type (Th = 31.6–39.4 ppm; Nb = 94.2–111 ppm). Niobium when plotted against Th exhibits a positive correlation, whereas there is no correlation with Ta (see Figure 4.11a and d). The Nb when plotted against TiO_2 shows no correlation and samples are clustered in a small area due to narrow variations in concentrations (Figure 4.11b).

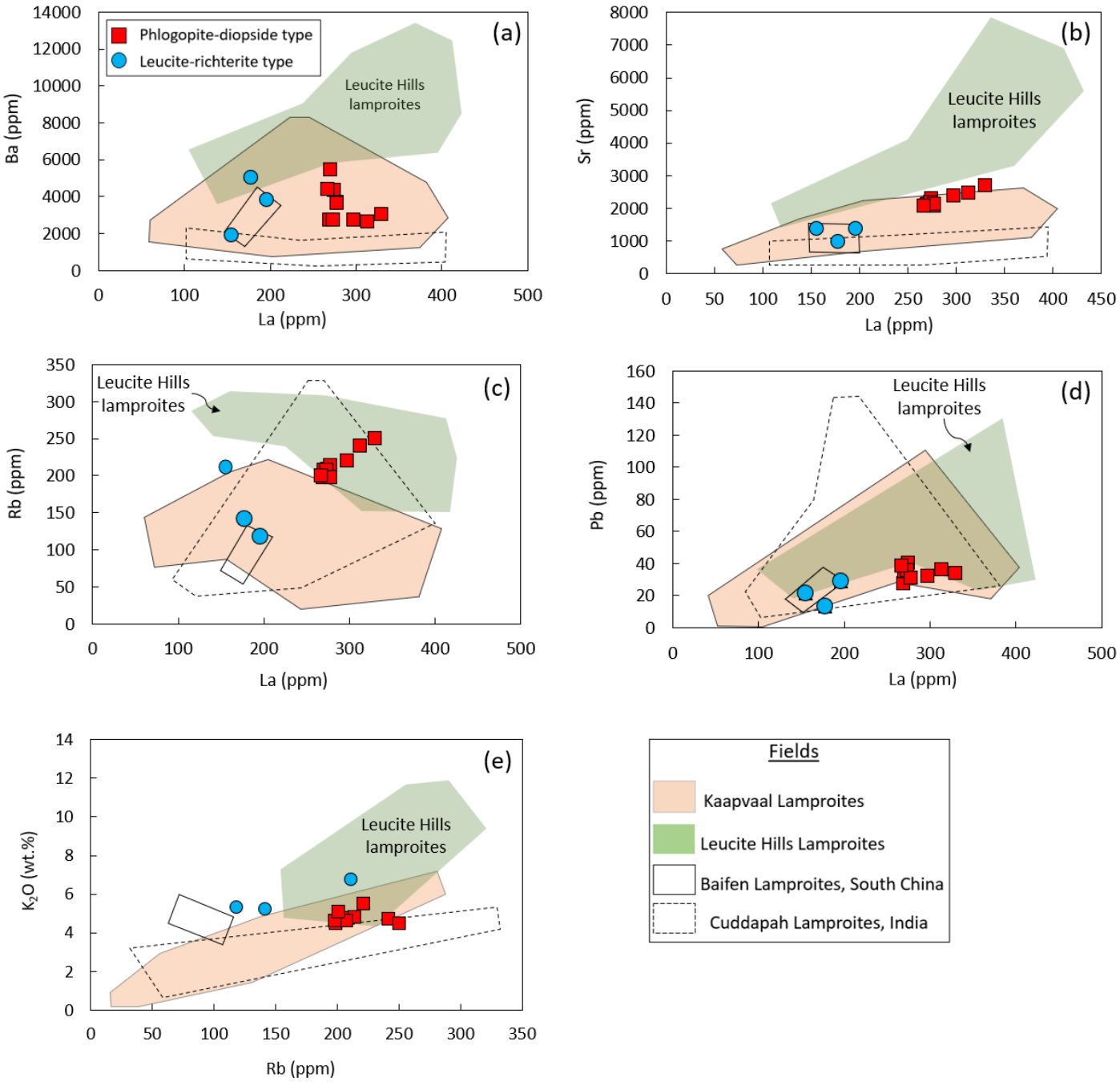

Figure 4. 10: Covariation plots of selected LILE in Kareevlei lamproites samples, compared to Kaapvaal lamproites (Becker and le Roex, 2006; Coe et al., 2008), Leucite Hills lamproites (Mirnejad and Bell, 2006), Cuddapah lamproites, India (Chalapathi-Rao et al., 2004), and Baifen lamproites, South China (Xiang et al., 2020).

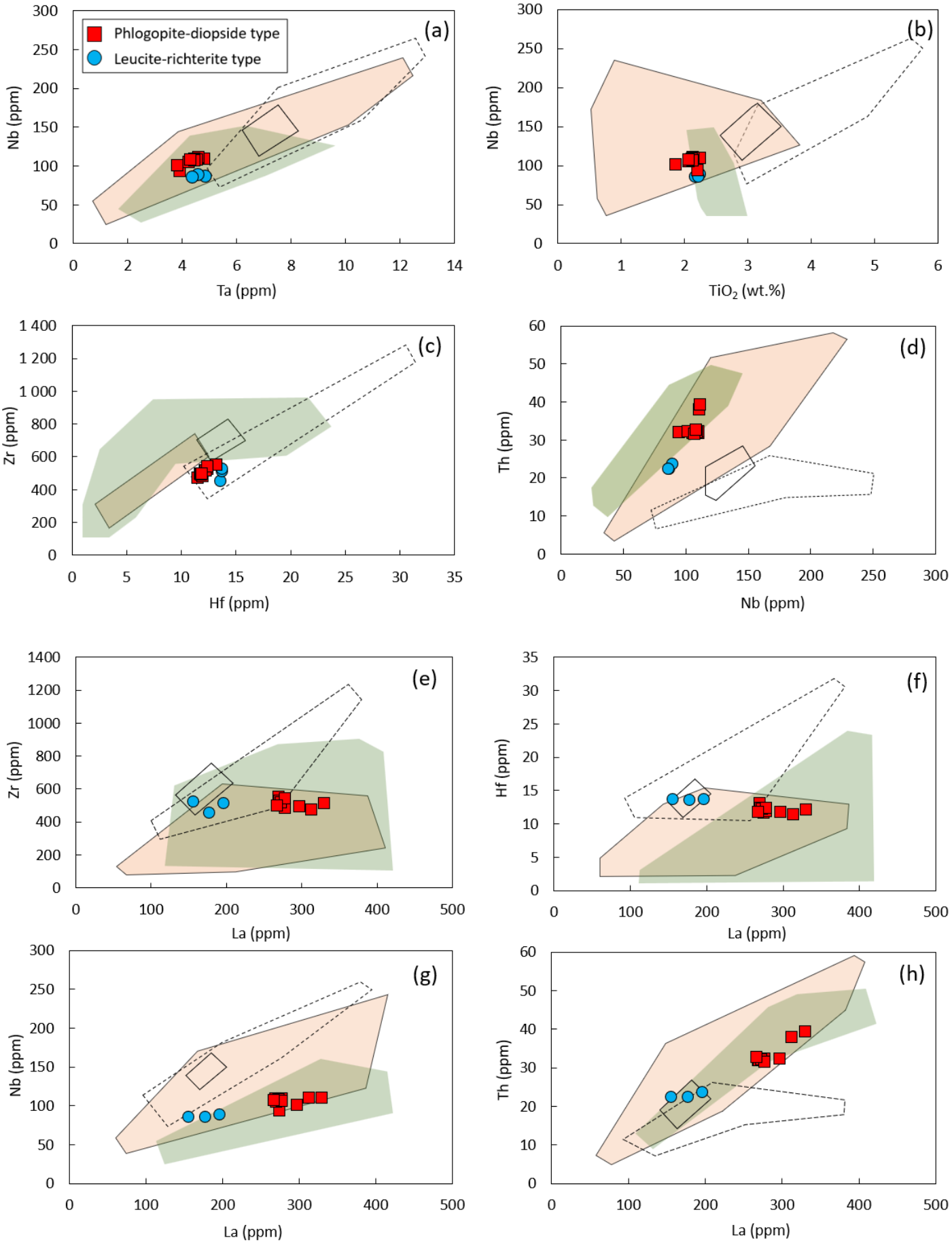
Phlogopite-diopside type
Leucite-richterite type
(a)
Nb (ppm)
Ta (ppm)
(b)
Nb (ppm)
TiO2 (wt.%)
(c)
Zr (ppm)
Hf (ppm)
(d)
Th (ppm)
Nb (ppm)
(e)
Zr (ppm)
La (ppm)
(f)
Hf (ppm)
La (ppm)
(g)
Nb (ppm)
La (ppm)
(h)
Th (ppm)
La (ppm)

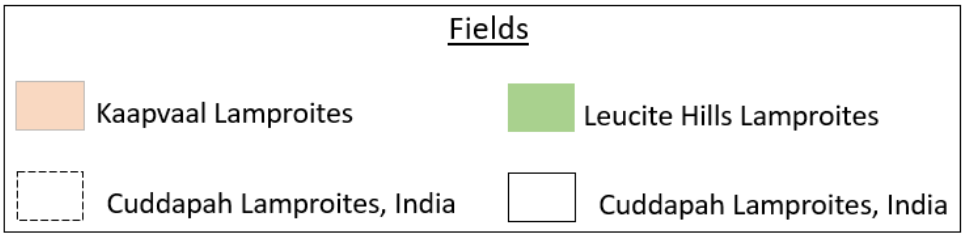

Figure 4. 11: Covariation plots of selected high field strength elements (HFSE) in Kareevlei Kaapvaal lamproite samples, compared to other Kaapvaal lamproites (Becker and Le Roex, 2006; Coe et al., 2008), Leucite Hills lamproites (Mirnejad and Bell, 2006), Cuddapah lamproites, India (Chalapathi-Rao et al., 2004), Baifen lamproites, South China (Xiang et al., 2020).

The Kareevlei lamproites are characterized by variable incompatible trace element ratios of Ba/Nb = 22.1 to 58.6, La/Nb = 1.82 to 2.97, Ce/Pb = 12.6 to 24.5, La/Yb = 101 to 205, and Gd/Yb = 6.28 to 9.55. The leucite-richterite samples are characterized by distinctly lower values of La/Sm, Gd/Yb, and La/Yb than the phlogopite-diopside types (Figure 4.12c and d). These ratios (i.e., La/Sm and Gd/Yb) exhibit a positive correlation when plotted against La/Yb (Figure 4.12c and d). In La/Nb–Ba/Nb covariation plots, the samples show no significant correlation and are scattered across a wide area (Figure 4.12b). The Ce/Pb ratios are relatively constant at widely varying Ba/Nb ratios (Figure 4.12a).

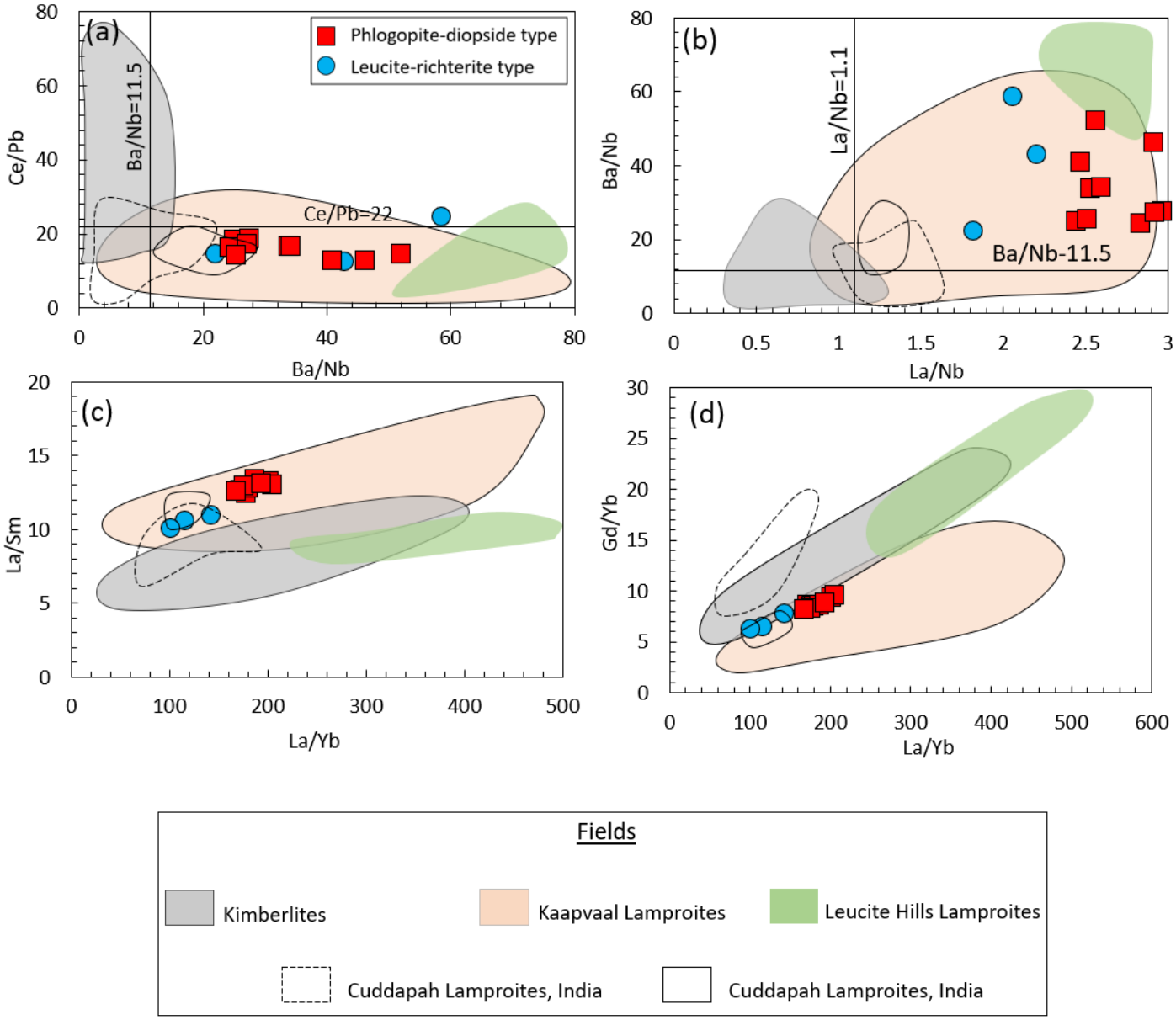

Figure 4. 12: Covariation plots of trace element ratios in Kareevlei lamproites samples, compared to kimberlites (Becker and Le Roex, 2006; Le Roex et al., 2003), Kaapvaal lamproites (Becker and Le Roex, 2006; Coe et al., 2008), Leucite Hills lamproites (Mirnejad and Bell, 2006), Cuddapah lamproites, India (Chalapathi-Rao et al., 2004), and Baifen lamproites, South China (Xiang et al., 2020).

When the REE data of the Kareevlei samples are normalized to chondrite values (Sun and McDonough, 1989), they are relatively enriched in LREE relative to HREE and characterized by steep, sub-parallel patterns that flatten toward the HREE (Figure 4.13a and b). In these chondrite-normalized distribution patterns, the leucite-richterite samples are slightly depleted in LREE compared to the phlogopite-diopside samples, whereas they appear to have similar HREE compositions. In extended trace element patterns normalized to primitive mantle values (Sun and McDonough, 1989), these rocks exhibit negative anomalies of Sr, P, Ti, and Ta–Nb, with positive anomalies of Ba and Pb (Figure 4.13c and d).

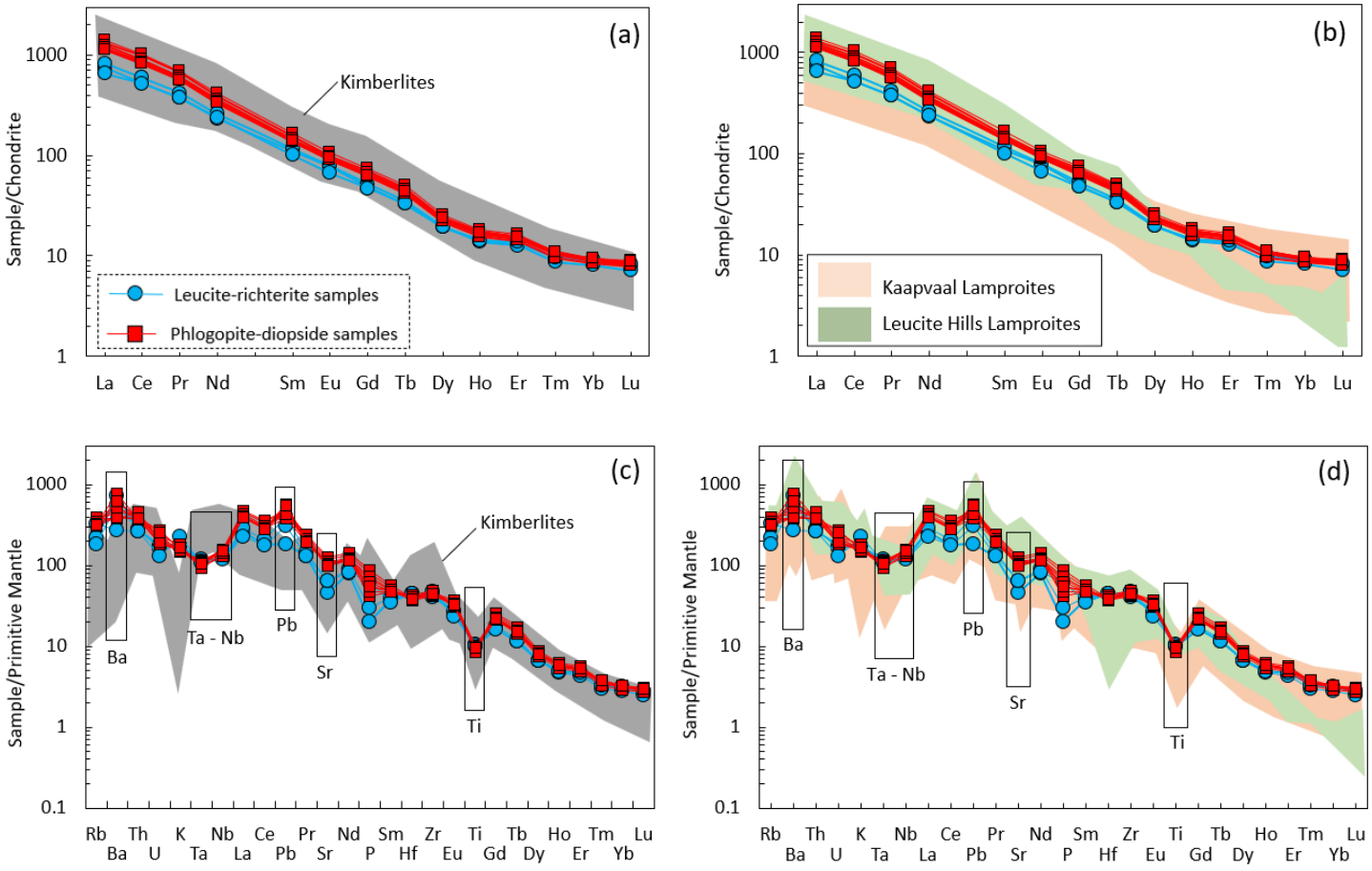

Figure 4. 13: Chondrite normalized REE patterns and primitive mantle normalized trace element distribution patterns of Kareevlei lamproites in comparison with kimberlites (A and C) and lamproites (B and D). The fields of kimberlite, Leucite Hills lamproites, and Kaapvaal lamproites were compiled from the same bulk-rock literature data in Figure 4.12.

Table 4. 3: Bulk-rock trace element compositions (in ppm) of the Kareevlei lamproites.

	Leucite-richterite samples			Phlogopite-diopside samples									
	KRV2	KRV3	KRV4	KRV5	KRV6	KRV7	KRV8	KRV9	KRV10	KRV11	KRV12	KRV13	KRV14
Li	13.4	9.68	10.2	8.54	8.26	7.60	7.65	8.37	10.4	7.92	7.71	8.86	8.36
Zn	142	94.5	93.6	99.2	84.2	88.5	85.8	87.2	89.5	77.6	100	84.7	85.5
Co	42.7	48.2	49.2	61.2	59.5	63.4	56.9	56.4	57.3	51.4	56.3	58.3	54.8
Cr	798	871	851	1014	1030	972	993	976	995	1006	1078	980	904
Ni	451	585	486	628	605	689	598	585	586	559	591	598	561
Cu	60.8	40.1	34.4	41.7	37.2	38.0	42.5	42.5	47.2	36.8	39.0	42.2	45.9
V	185	144	138	147	105	88.8	135	121	116	131	128	116	152
Sc	18.9	18.1	21.8	21.6	25.1	24.8	22.2	22.4	22.6	23.7	23.5	22.5	22.5
Rb	141	118	211	199	241	250	209	208	214	221	208	198	201
Sr	958	1370	1356	2123	2473	2698	2311	2145	2094	2384	2206	2140	2077
Y	20.7	19.8	19.8	24.8	24.1	25.6	24.4	23.5	23.7	24.4	23.8	22.3	24.5
Zr	456	513	526	553	476	517	500	530	485	495	518	543	500
Nb	86.2	89.0	85.5	110	110	111	94	105	110	102	109	107	108
Ba	5048	3813	1890	2751	2677	3046	4351	5472	3715	2756	2751	3655	4424
La	177	196	155	269	313	330	274	270	277	297	272	277	267
Ce	322	365	317	509	595	630	516	509	523	551	513	519	500
Pr	35.7	39.6	35.5	54.2	62.9	66.4	54.7	53.8	55.4	58.1	54.6	54.8	52.9
Nd	109	122	111	160	183	194	161	159	162	168	160	160	156
Sm	16.8	17.9	15.5	21.2	23.6	25.2	21.7	21.7	21.7	22.2	21.0	21.2	21.2
Eu	4.46	4.58	3.89	5.32	5.74	6.16	5.54	5.66	5.42	5.43	5.17	5.27	5.45
Gd	9.84	10.6	9.69	13.4	14.4	15.3	13.1	12.8	13.1	13.7	12.9	12.6	12.9
Tb	1.23	1.32	1.24	1.68	1.78	1.88	1.63	1.61	1.62	1.70	1.62	1.56	1.63
Dy	4.89	4.95	4.90	6.08	6.11	6.49	5.91	5.79	5.88	6.01	5.83	5.51	5.96
Ho	0.81	0.78	0.80	0.98	0.97	1.03	0.96	0.93	0.95	0.96	0.94	0.87	0.96
Er	2.23	2.10	2.27	2.54	2.57	2.71	2.54	2.45	2.51	2.55	2.49	2.33	2.56
Tm	0.24	0.22	0.25	0.27	0.26	0.28	0.27	0.26	0.26	0.27	0.26	0.24	0.28
Yb	1.53	1.38	1.54	1.56	1.55	1.61	1.56	1.52	1.54	1.59	1.55	1.43	1.59
Lu	0.20	0.18	0.21	0.21	0.22	0.23	0.22	0.21	0.21	0.22	0.22	0.20	0.22
Hf	13.6	13.7	13.7	13.1	11.5	12.1	11.7	12.4	12.0	11.8	12.2	12.4	11.9
Ta	4.85	4.60	4.39	4.79	4.60	4.60	3.91	4.24	4.45	3.81	4.54	4.45	4.30
Pb	13.1	29.0	21.7	27.5	36.3	33.9	40.6	35.2	31.4	32.2	35.7	31.1	38.7
Th	22.5	23.8	22.5	31.9	38.1	39.4	32.0	31.9	32.4	32.4	32.2	31.6	32.7
U	3.78	3.38	2.75	4.27	4.52	4.03	5.68	4.82	4.06	4.76	3.82	4.14	5.31
Calculated ratios													
Ba/Nb	58.6	42.9	22.1	25.0	24.3	27.4	46.2	52.0	33.9	27.1	25.3	34.2	41.0
La/Nb	2.06	2.21	1.82	2.45	2.84	2.97	2.91	2.56	2.53	2.92	2.51	2.59	2.47
Ce/Pb	24.5	12.6	14.6	18.5	16.4	18.6	12.7	14.5	16.7	17.1	14.4	16.7	12.9
La/Sm	10.6	11.0	10.0	12.7	13.2	13.1	12.6	12.4	12.8	13.4	13.0	13.1	12.6
La/Yb	116	143	101	172	202	205	176	178	180	187	176	194	167
Gd/Yb	6.45	7.73	6.28	8.59	9.32	9.55	8.40	8.45	8.50	8.63	8.34	8.85	8.13

4.3.3 Sr-Nd isotope geochemistry

The measured $^{87}Sr/^{86}Sr$ and $^{143}Nd/^{144}Nd$ ratios of the Kareevlei lamproite varieties are similar, and have narrow ranges of $^{87}Sr/^{86}Sr$ = 0.707605 ± 0.000010–0.707969 ± 0.000015 and $^{143}Nd/^{144}Nd$ = 0.511841 ± 0.000006–0.511923 ± 0.000016. The initial rations of $^{87}Sr/^{86}Sr$ and $^{143}Nd/^{144}Nd$ were calculated using the isochron equations $(^{87}Sr/^{86}Sr)_m = (^{87}Sr/^{86}Sr)_i + (^{87}Rb/^{86}Sr)(e^{\lambda t} - 1)$ (equation 1) and $(^{143}Nd/^{144}Nd)_m = (^{143}Nd/^{144}Nd)_i + (^{147}Sm/^{144}Nd)(e^{\lambda t} - 1)$ (equation 2), where $(^{87}Sr/^{86}Sr)_m$ and $(^{143}Nd/^{144}Nd)_m$ represent the measured ratios and $(^{87}Sr/^{86}Sr)_i$ and $(^{143}Nd/^{144}Nd)_i$ represent the initial ratios. The $^{87}Rb/^{86}Sr$ and $^{147}Sm/^{144}Nd$ ratios in the above equations were calculated from the total concentrations (in ppm) of Rb, Sr, Sm, and Nd produced by ICP-MS analysis and natural abundances of their stable isotopes. That is, the ^{87}Rb, ^{86}Sr, ^{147}Sm, and ^{144}Nd proportions were calculated from total concentrations in ppm (Table 4.3).

The λ represents the decay constant from parent to daughter, which is equal to 1.42×10^{-11} for the breakdown of ^{87}Rb to ^{87}Sr and 6.54×10^{-12} for the breakdown of ^{147}Sm to ^{144}Nd (Winter, 2001). The t is the age of the Kareevlei lamproites. Kaapvaal lamproites in the same region of the craton are generally of similar age (Mitchell, 1995). The exact age of the Kareevlei lamproite is unknown but it is located near Finsch Kaapvaal lamproite, which has an age of 118 Ma (Smith, 1983; Field et al., 2008). Therefore, I assume Kareevlei lamproites have a similar age of 118 Ma, and used this in Sr and Nd initial ratio calculations. The $^{87}Sr/^{86}Sr_i$ ratios do not show a great difference from the measured ratios; they have a narrow range of $(^{87}Sr/^{86}Sr)_i$ = 0.707068 – 0.707302. Epsilon values of Nd ($^{\varepsilon}Nd$) present the degree of enrichment and depletion of Nd in the mantle source, and were calculated using the following equation:

$$\mathbf{^{\varepsilon}Nd = [(^{143}Nd/^{144}Nd)_i / I^t_{CHUR} - 1] \times 10\,000} \text{ (equation 3)}$$

The $^{143}Nd/^{144}Nd_i$ ratios range from 0.511769 to 0.511859 and were calculated using equation 2. The I^t_{CHUR} is the $^{143}Nd/^{144}Nd$ ratio for the chondrite uniform reservoir (CHUR) at the time of the rock formation (t) and it was calculated from equation 4:

$$\mathbf{(^{143}Nd/^{144}Nd)_{CHUR,t} = (^{143}Nd/^{144}Nd)_{CHUR,\,today} - (^{147}Sm/^{144}Nd)_{CHUR,today}} \text{ (equation 4)}$$

The calculated $^{\varepsilon}Nd_i$ values have a range from -14.0 to -12.2 (Figure 4.14).

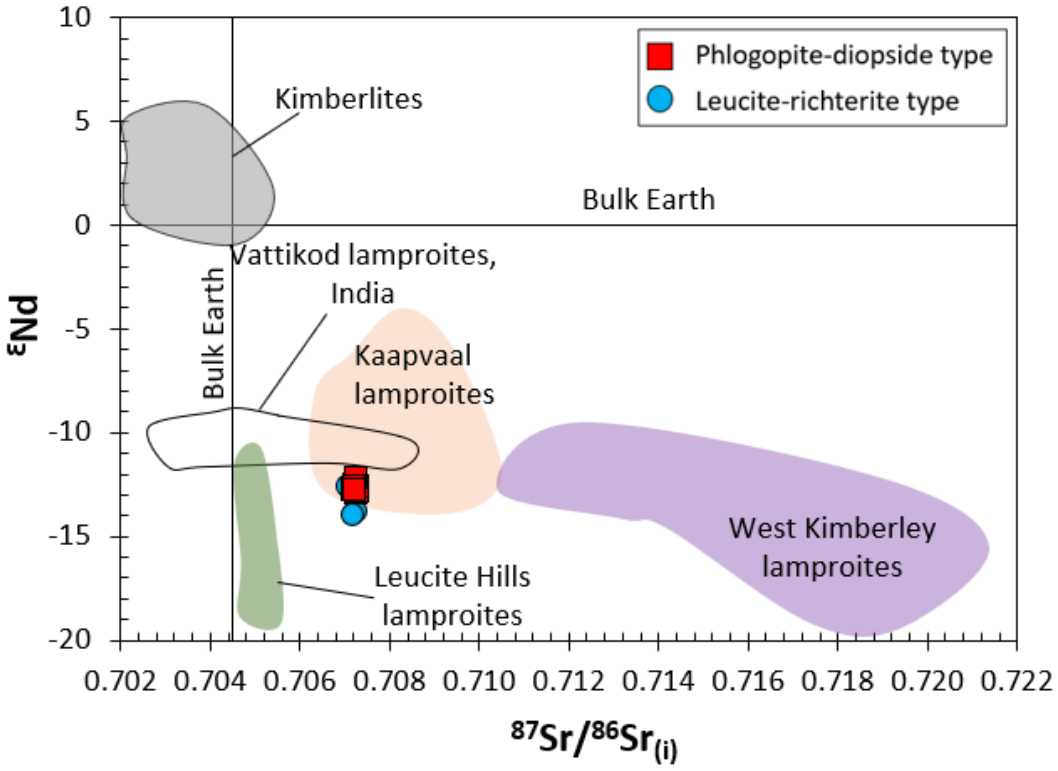

Figure 4. 14: Variations in isotopic composition of Kareevlei lamproites compared to kimberlites (Becker and Le Roex, 2006), Kaapvaal lamproites (Becker and Le Roex, 2006; Coe et al., 2008), West Kimberley lamproites (Fraser, 1988), Leucite Hills lamproites (Mirnejad and Bell, 2006), and Vattikod lamproites (Talukdar et al., 2018). The initial ratios and $^{\varepsilon}$Nd values were calculated assuming ages of 118 Ma (Mitchell, 1995 and Field et al., 2008).

Table 4. 4: Measured and calculated initial ratios of Sr-Nd isotopes.

	Leucite-richterite samples			**Phlogopite-diopside samples**			
	KRV2	KRV3	KRV4	KRV5	KRV6	KRV7	KRV8
Rb (ppm)	141	118	211	199	241	250	209
Sr (ppm)	958	1370	1356	2123	2473	2698	2311
$^{87}Rb/^{86}Sr$	0.4154	0.2429	0.4395	0.2639	0.2752	0.2618	0.2550
$^{87}Sr/^{86}Sr$ (m)	0.707969	0.707605	0.707804	0.707712	0.707661	0.707671	0.707633
±SD	0.000012	0.000015	0.000012	0.000010	0.000010	0.000010	0.000011
Sm (ppm)	16.8	17.9	15.5	21.2	23.6	25.2	21.7
Nd (ppm)	109	122	111	160	183	194	161
$^{147}Sm/^{144}Nd$	0.096743	0.092661	0.087698	0.083577	0.081309	0.082037	0.084969
$^{143}Nd/^{144}$ Nd (m)	0.511852	0.511841	0.511909	0.511887	0.511900	0.511907	0.511905
±SD	0.000010	0.000009	0.000012	0.000008	0.000009	0.000009	0.000009
	at 110 Ma						
$^{87}Sr/^{86}Sr_{(i)}$	0.707273	0.707197	0.707068	0.707270	0.707200	0.707233	0.707206
$^{143}Nd/^{144}Nd_{(i)}$	0.511777	0.511769	0.511842	0.511823	0.511837	0.511844	0.511839
$^{\varepsilon}$Nd	-13.8	-14.0	-12.6	-12.9	-12.7	-12.5	-12.6

Table 4. 4: Continued

	Diopside-phlogopite type					
	KRV9	KRV10	KRV11	KRV12	KRV13	KRV14
Rb (ppm)	208	214	221	208	198	201
Sr (ppm)	2145	2094	2384	2206	2140	2077
$^{87}Rb/^{86}Sr$	0.2737	0.2886	0.2617	0.2656	0.2613	0.2728
$^{87}Sr/^{86}Sr_{(m)}$	0.707746	0.707786	0.707699	0.707619	0.707664	0.707694
±SD	0.000010	0.000014	0.000010	0.000011	0.000015	0.000010
Sm (ppm)	21.7	21.7	22.2	21.0	21.2	21.2
Nd (ppm)	159	162	168	160	160	156
$^{147}Sm/^{144}Nd$	0.086391	0.084544	0.083038	0.082859	0.083460	0.085769
$^{143}Nd/^{144}Nd_{(m)}$	0.511895	0.511905	0.511923	0.511896	0.511906	0.511897
±SD	0.000006	0.000013	0.000009	0.000016	0.000011	0.000007
			At 110 Ma			
$87Sr/86Sr_{(i)}$	0.707287	0.707302	0.707260	0.707174	0.707227	0.707237
$^{143}Nd/^{144}Nd_{(i)}$	0.511828	0.511840	0.511859	0.511833	0.511842	0.511831
$^{\varepsilon}Nd$	-12.8	-12.6	-12.2	-12.8	-12.6	-12.8

CHAPTER 5: DISCUSSION

5.1 Classification of Kareevlei rocks

The presented petrography and mineral composition data are evaluated here to classify the Kareevlei rocks as kimberlites or lamproites based on the nomenclature proposed by Mitchell et al. (2019), i.e., the groundmass mineralogy along with the compositions of phlogopite. The Kareevlei rocks exhibit typical lamproitic mineralogical characteristics, in which the abundant Al_2O_3- and Na_2O-poor primary diopside (Al_2O_3 < 1 wt.% and Na_2O < 1.5 wt.%), abundant phlogopite, K-richterite, and spherical pseudo-leucites occur alongside secondary minerals such as serpentine and less common carbonate. In addition, the compositional trend of zoned phlogopites, i.e., the Al_2O_3 depletion coupled with TiO_2 and FeO enrichment toward the rims is typical of lamproites (e.g., Mitchell, 1995). Overall, the petrographic observations including the presence of abundant primary diopside, K-richterite, and pseudo-leucite supported by mineral compositions (e.g., phlogopite composition trends) strongly suggest that the Kareevlei rocks are lamproites and part of the previously termed "evolved orangeite or Group II kimberlite" group (e.g., Mitchell, 1995). Thus, they are classified as Kaapvaal lamproites.

5.2 Origin of compositional zoning in phlogopite, K-richterite, and diopside from Kareevlei Kaapvaal lamproites

Kaapvaal lamproites commonly comprise abundant macrocrystic grains, predominantly olivine, phlogopite, and less commonly diopside, which are characterized by compositionally distinct core and rim zones. The cores in phlogopite grains of kimberlites and lamproites are commonly interpreted to be xenocrystic in origin, derived from disaggregation of mantle xenoliths, whereas the rims are magmatic in origin and crystallized from the magma during the evolution (Mitchell, 1995; Giuliani et al., 2016), and the same has been shown to apply to olivine (e.g., Arndt et al., 2010; Giuliani, 2018; Howarth and Nembambula, 2021; Viljoen et al., 2022). Compositional zoning in phlogopite indicates crystallization during rapid changes in crystallization conditions, and therefore makes it a good petrogenetic indicator of magma evolution (e.g., Pasteris, 1983; Giuliani et al., 2016; Shaikh et al., 2017). In Kareevlei Kaapvaal lamproites, I evaluate the compositionally distinct core and rim zones in phlogopite and diopside to constrain the xenocrystic and/or magmatic origin.

Phlogopite in the Kareevlei lamproites is a major phase occurring as zoned laths and groundmass poikilitic grains. The phlogopite laths show two distinct core populations characterized by (1) high- and (2) low-Cr_2O_3 concentrations mantled by Cr_2O_3-poor, and TiO_2 and FeO-rich rims (Figures 4.5c and d). Significantly, the Cr_2O_3-rich nature of the high-Cr core population is similar to phlogopite reported from metasomatized phlogopite peridotite mantle xenoliths and indicates crystallization at high pressure-temperature (P–T) conditions (P = ~1.0–2.0 GPa; T = ~950–1 050°C) at depth in the mantle compared to rims and the groundmass phlogopite (e.g., Çoban and Flower, 2006; Giuliani et al., 2016; Shaikh et al., 2017). Similar phlogopite with Cr_2O_3-rich and TiO_2-poor cores mantled by Cr_2O_3-poor and TiO_2-rich rims are recognized in lamproites from other cratonic regions, e.g., in the Bucak area, SW Turkey (Çoban and Flower, 2006) and Karelian craton, Russia (Shaikh et al., 2017). These cores are relatively Cr_2O_3-rich (1.17–1.82 wt.%) compared to typical Kaapvaal lamproites, e.g., Finsch, Swartruggens, and Sover North (Cr_2O_3 0.11–1.47 wt.%; Mitchell, 1995), and interpreted to be xenocrysts crystallized at deeper levels of the mantle or inherited from metasomatized peridotite mantle lithologies (e.g., Giuliani et al., 2013, 2016; Kopylova et al., 2010; Shaikh et al., 2017). Therefore, in the Kareevlei lamproites, this would suggest that the high-Cr_2O_3 cores could have been derived from metasomatized mantle peridotites.

In contrast, the low-Cr_2O_3 cores analysed in this study display Cr_2O_3 compositions that have been exhibited by phlogopites previously analyzed by Giuliani et al. (2013) and Grégoire et al. (2003) in MARID xenoliths from the Kimberley area, South Africa (Figures 4.5c and d). Significantly, MARIDs are generally interpreted to be the source of Kaapvaal lamproites (e.g., Giuliani et al., 2015; Mitchell and Edgar, 2002; Wagner and Velde, 1986). Therefore, in Kareevlei lamproites, this could suggest that the low-Cr_2O_3 cores are derived from MARIDs. The two phlogopite core populations in both Kareevlei lamproite varieties are thus interpreted to be xenocrystic in origin, derived from two separate mantle lithologies. Phlogopite core-to-rim trends of Al_2O_3 and MgO depletion coupled with TiO_2 and FeO enrichment (see Figures 4.4a and b; 4.5a and b) are consistent with magmatic evolutionary trends described by Mitchell (1995) in other Kaapvaal lamproites. Thus, this would suggest that the rims are of magmatic origin and crystallized during magma evolution.

Experimental studies indicate that TiO_2 compositions in both K-richterites and phlogopites have an inverse relationship with pressure (P); i.e., they decrease continuously with increasing pressure (Foley, 1990; Konzett, 1997). Thus, Kareevlei K-richterites having TiO_2 contents ranging from 3.39 to 5.13 wt.%, comparable with poikilitic groundmass phlogopite and rim zones, could indicate that these K-richterites were contemporaneous with groundmass phlogopite crystallization at low P. In addition, the occurrence of these K-richterites as groundmass plates and patches usually mantled by TiO_2-rich groundmass poikilitic phlogopite and in places hosting pseudo-leucite inclusions suggests contemporaneous crystallization with these phlogopites. The Kareevlei K-richterite has higher TiO_2 compositions relative to other Kaapvaal lamproites and is comparable with K-richterite in Leucite Hills and Murcia-Almeria (4.06–8.48 wt.%) and West Kimberley (4.57–8.01

wt.%) lamproites reported by Mitchell and Bergman (1991), however, the Na/K ratios are similar to that of previously reported Kaapvaal lamproites (see Figure 4.6b).

Diopside in the Kareevlei lamproites generally forms unzoned prismatic grains and rarely subhedral-to-anhedral zoned macrocrysts, which is typical of many lamproites worldwide (Howarth and Giuliani, 2020; Kargin et al., 2014; Coban and Flower, 2006). The diopside laths are included, along with pseudo-leucite, in the poikilitic phlogopite and appear to have been crystallized contemporaneously with spherical pseudo-leucite. Such diopside textural occurrences have been identified in other leucite lamproites (e.g., Foley, 1989) and madupitic lamproites (e.g., Tainton, 1992) and were interpreted to have crystallized in the magma contemporaneously with leucites at low P (~0.5 GPa). The majority of diopsides in Kareevlei lamproites are FeO-poor and fall within the field of diopside in the quadrilateral (Figure 4.7a). In contrast, the core zones of diopside macrocrysts are FeO- and MgO-rich, overlapping with diopside compositions in mantle xenoliths. These more augite-rich cores are relatively poor in TiO_2 (0.14–0.31 wt.%) and CaO (22.5–22.7 wt.%) compared to their rims (TiO_2 = 0.90–1.03 wt.%; CaO = 25.0–25.1 wt.%), which have analogous compositions to other unzoned diopside grains in the groundmass. The cores have analogous compositions with garnet lherzolite from the Kaapvaal craton (TiO_2 = 0.01–0.62 wt.%; CaO = 16.1–22.0 wt.%; Grégoire et al., 2003) and are likely xenocrystic in origin, whereas their rims have crystallized in the lamproite magma en route to the surface.

5.3 Alteration and contamination of bulk-rock geochemistry

The most important and diagnosable geochemical aspect of magma compositional evolution is alteration and/or contamination through volatiles related to the magma (deuteric alteration), interaction with groundwater in post-emplacement, and incorporation of crustal xenoliths into the rock. The alteration was identified by petrographic analyses and crustal xenoliths were identified and carefully eliminated during careful sample preparation for bulk-rock geochemistry. However, these processes such as alteration and crustal contamination can potentially influence the bulk-geochemical compositions and therefore need to be identified and/or evaluated even post-sample preparation. The lack of positive correlation between $(^{87}Sr/^{86}Sr)_i$ and SiO_2 bulk-compositions in the Kareevlei lamproites (Figure 5.1) is interpreted to indicate that crustal contamination did not play a significant role in geochemical compositions (e.g., Xiang et al., 2020).

Petrographic observations show evidence of late-stage or low-temperature alteration throughout both Kareevlei lamproite varieties: olivine microcrysts and macrocrysts are completely altered to a variety of serpentine and carbonate. In leucite-richterite types, the leucite is altered and completely pseudomorphed. Low-temperature alteration effects can be examined by contrasting the behavior of mobile elements (e.g., Ba, Rb, Sr, etc), where the systematic deviations of elements or element ratios in the plots against immobile elements (e.g., La) indicate modification of geochemical composition by alteration (Coe et al., 2008; Le Roex et al., 2003; Xiang et al., 2020). The LILE (e.g., Rb and Sr) and HFSE (e.g., Nb and Th) exhibit a slight to moderate deviation from the slope, which implies that these elements have partially been disturbed (Figure 5.2). However, the incompatible REEs (e.g., Sm and Gd) including their ratios (e.g., La/Sm and Gd/Yb) exhibit a coherent positive correlation with La and La/Yb (Figures 4.12c and d, and 5.2), suggesting that these elements are mainly unaffected by alteration. Therefore, this suggests that it is appropriate to constrain mantle source characteristics of Kareevlei Kaapvaal lamproites on the basis of incompatible REEs, whereas other elements appear to have been variably affected by late-stage alteration consistent with suggestions in previous studies (e.g., Le Roex et al., 2003; Xiang et al., 2020).

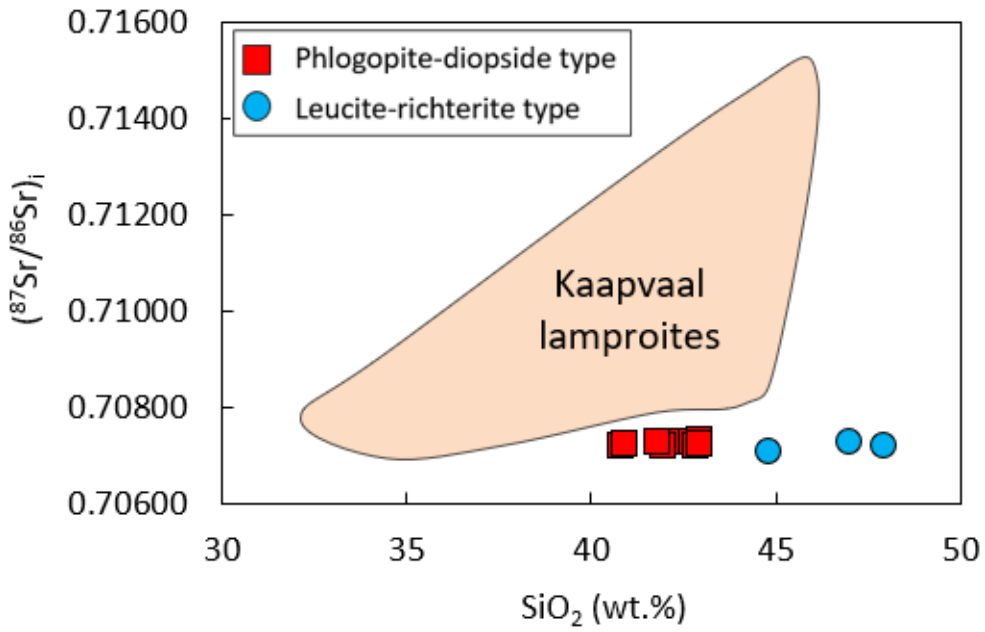

Figure 5. 1: $^{87}Sr/^{86}Sr$ initial ratios vs SiO_2 (wt.%) for the Kareevlei Kaapvaal lamproites. The field of Kaapvaal lamproites is compiled from on-craton Kaapvaal lamproites from New Elands, Newlands, and Robert Victor (Becker and Le Roex, 2006) and from Lace and Voorspoed lamproites (Howarth et al., 2011).

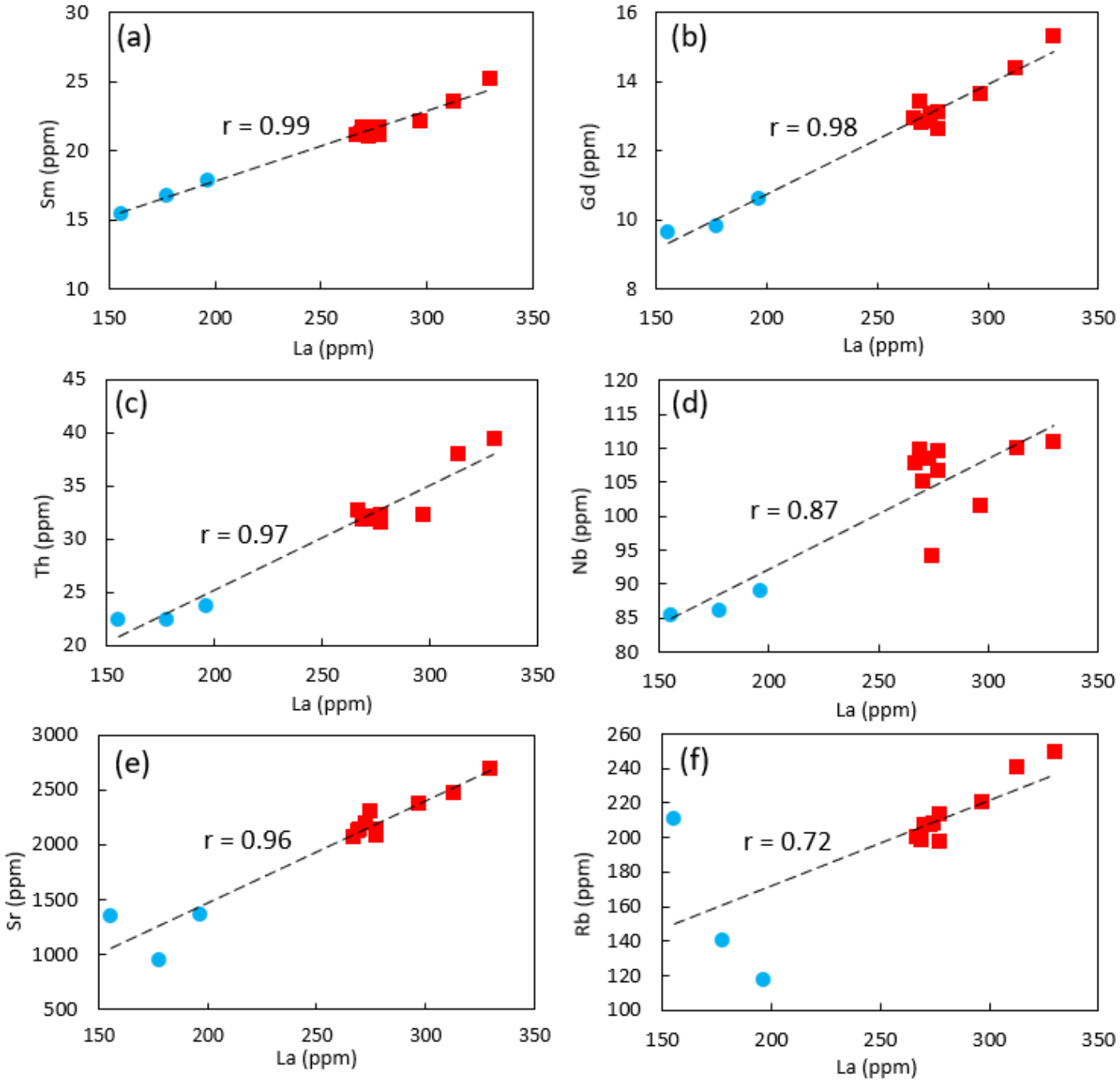

Figure 5. 2: Variation plots of selected incompatible trace elements in Kareevlei lamproites. Note: blue circles represent leucite-richterite lamproites, and red squares represent phlogopite-diopside lamproites. The r is the correlation strength.

5.4 Petrogenesis of Kareevlei phlogopite-diopside compared to leucite-richterite lamproites

Kaapvaal lamproites generally vary widely in mineralogy, typically from unevolved to evolved varieties (Mitchell, 1995). Mitchell (1995) notes that the mineral assemblages can even vary within a single intrusion or a pipe; for example, in the Voorspoed pipe (Howarth et al., 2011). The Kareevlei Kaapvaal lamproites show two distinct mineralogical varieties based on the presence/absence of certain alkali-rich phases (i.e., K-richterite and leucite) clearly displayed by petrography and variation in bulk-rock geochemical compositions. Here I evaluate the petrogenesis of these mineralogically distinct lamproites and evaluate whether the evolution from one mineralogical variety to the other resulted from fractionation, source heterogeneity, or variable degrees of partial melting.

5.4.1 Role of fractional crystallization and mantle xenocryst entrainment

Kimberlites and olivine lamproites generally comprise olivine macrocrysts that are xenocrysts derived by the disaggregation of mantle peridotites, and thus represent mantle cargo that these melts have transported to the surface (Becker and Le Roex, 2006; Le Roex et al., 2003; Scott Smith, 2017). Recent studies have revealed that both macrocrysts and microcrysts contain xenocrystic cores, but they also both contain magmatic overgrowth rims (e.g., Giuliani, 2018; Howarth and Giuliani, 2020), indicating that loss of olivine macrocrysts and/or microcrysts through fractionation en route to the surface can result in magma evolution. The entrainment of xenocrystic olivines is expected to result in raised bulk-compositions of elements compatible with olivine such as MgO and Ni for olivine-rich varieties compared to olivine-poor varieties, whereas fractional crystallization will result in the opposite trend (e.g., Coe et al., 2008).

The Kareevlei Kaapvaal lamproites of this study have relatively low olivine macrocryst abundances (leucite-richterite lamproites = 7–11 vol.%; phlogopite-diopside lamproites = 3–12 vol.%) compared to typical Kaapvaal lamproites (~25 vol.%; Skinner, 1989; Mitchell, 1995), indicating potential loss through fractionation. However, the phlogopite-diopside lamproites have relatively high abundances of microcrystic olivines (9–19 vol.%) in the groundmass, compared to leucite-richterite varieties (olivine microcrysts = 3–8 vol.%). Nickel and Cr systemically decrease with decreasing MgO (wt.%) from phlogopite-diopside to leucite-richterite lamproite varieties, consistent with the lower abundances of olivines in leucite-richterite lamproites (Figure 4.9a and b). Thus, the major element compositions suggest that the leucite-richterite lamproites may have evolved from the phlogopite-diopside lamproites through fractionation of olivine phenocrysts as suggested in other studies for the origin of the evolved end-members (e.g., Coe et al., 2008; Howarth et al., 2011; Mitchell, 1995).

Moreover, Kargin et al. (2014) argued that fractionation is accompanied by the increase of SiO_2, Al_2O_3, Na_2O, K_2O, and slightly TiO_2 and FeO, along with the decrease in MgO, Cr_2O_3, and Ni in lamproitic magmas. The systematic decrease in MgO with an increase in SiO_2, Al_2O_3, and Na_2O towards leucite-richterite lamproites is consistent with fractionation (Figures 4.8a, e, and f). Therefore, following all the aforementioned major-geochemical trends defined by Coe et al. (2008), Howarth et al. (2011), and Kargin et al. (2014), the mineralogical varieties of Kareevlei lamproites could be generated by fractional crystallization with the leucite-richterite lamproites being the final product of olivine-dominated fractionation, and as a result, leucite-richterite lamproites are expected to be enriched in incompatible trace elements relative to their parental phlogopite-diopside rocks (e.g., Le Roex et al., 2003). Notably, La and other incompatible trace elements (e.g., LILE and HFSE) are higher in phlogopite-diopside samples than in the leucite-richterite samples, which rule out fractionation as the dominant control on the origin of the mineralogical variations of the Kareevlei lamproites.

In contrast to olivine fractionation, olivine xenocryst accumulation would result in elevated MgO and Ni contents of the bulk-rock. The MgO–Ni trends show clear separation with the phlogopite-diopside varieties following the trend of lherzolite accumulation (see Figures 5.3a and b). Thus, I suggest that the MgO–Ni trends can be attributed to relative olivine xenocryst accumulation. The elevated olivine macrocryst abundance, along with elevated MgO and Ni, of the phlogopite-diopside lamproites relative to the leucite-richterite lamproites support such an interpretation. Accumulation of olivine, however, should not significantly affect the incompatible trace element ratios and Sr-Nd isotopes, which can still be used to constrain the petrogenesis of the lamproites.

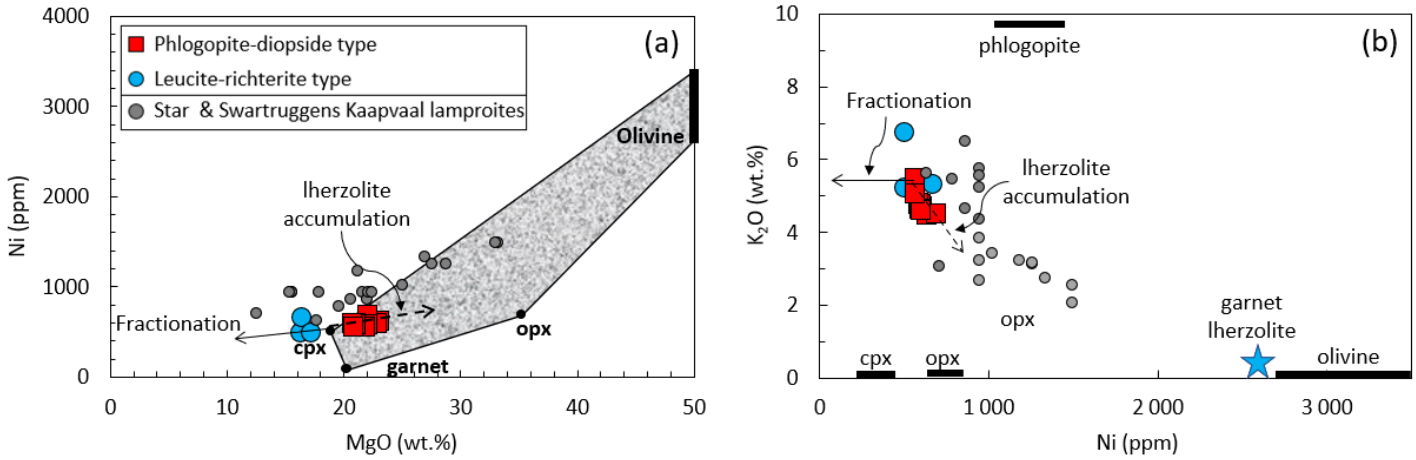

Figure 5. 3: The variation plots show the effect of xenocrystic olivine entrainment in the Kareevlei Kaapvaal lamproite varieties (Coe et al., 2008). The vectors on the graph represent the directions of the different processes that can change the chemistry of the rock. The gray field represents lherzolite composition.

5.4.2 Sr-Nd isotope constraints on mantle source

Kareevlei lamproites yielded $^{87}Sr/^{86}Sr_i$ ratios of 0.7071 to 0.7073, comparable with the range of other typical Kaapvaal lamproites as shown in Figures 4.14 and 5.4, e.g., Bellsbank, New Elands, Robert Victor, Newlands, Middle Water, Finsch ($^{87}Sr/^{86}Sr_i$ = 0.7072–0.7105; Becker and Le Roex, 2006; Mitchell, 1995), reflecting derivation from the SCLM as inferred for other Kaapvaal lamproites. The $^{143}Nd/^{144}Nd_i$ ratios (0.51177–0.51186) of Kareevlei lamproites corresponding with the $^{\varepsilon}Nd_i$ values (-14.0 to -12.2) slightly overlap with the unevolved Kaapvaal lamproites and are more comparable with the evolved subtypes from Sover North ($^{143}Nd/^{144}Nd_i$ = 0.51180–0.51181; $^{\varepsilon}Nd_i$ = -13.1 to -13.4; Mitchell, 1995). The Kaapvaal lamproites generally have similar Sr–Nd isotope compositions to the evolved subtypes, and there is no significant distinction between these lamproites, i.e., both unevolved and evolved varieties overlap in Sr–Nd space (Figure 4.14; Figure 5.4).

Likewise, Kareevlei lamproites exhibit no significant separation in Sr–Nd compositions between the mineralogical varieties and thus, the relative evolution in Kareevlei lamproites does not affect Sr–Nd isotope compositions, which suggests derivation from an isotopically homogeneous mantle source. If the two lamproite varieties are derived from a heterogeneous mantle source, they would be expected to yield different or varying Sr–Nd isotope compositions (Mitchell, 1995). Furthermore, the difference in incompatible trace elements and their ratios of Kareevlei lamproite varieties cannot be accounted for by fractional crystallization of Kareevlei magma but could be achieved by variable degrees of partial melting (e.g., Coe et al., 2008), which is discussed in the next section.

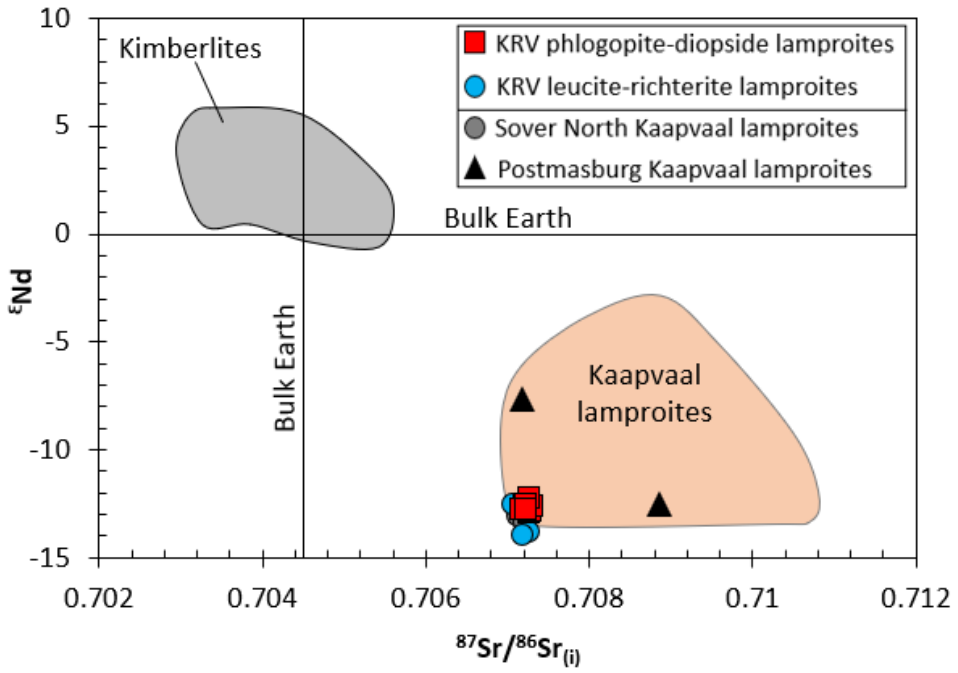

Figure 5. 4: Sr–Nd isotope compositions of Kareevlei lamproites in comparison to kimberlites (Becker and Le Roex, 2006) and other Kaapvaal lamproites (Becker and Le Roex, 2006; Coe et al., 2008; Mitchell, 1995). The Postmasburg and Sover North Kaapvaal lamproites are evolved varieties/subtypes of Kaapvaal lamproites (Mitchell, 1995). Sover North plots exactly underneath the Kareevlei lamproites. Note: KRV = Kareevlei.

5.4.3 Evaluation of variable degrees of partial melting

At Kareevlei, it is noted with reference to chondrite-normalized REE patterns that the phlogopite-diopside lamproites have slightly raised LREE patterns (Figures 4.13a and b) with higher La/Yb ratios (La/Yb_N = 120–147) relative to the sub-parallel leucite-richterite lamproites pattern (La/Yb_N = 72–102). Incompatible trace element ratios (e.g., Gd/Yb, La/Sm, and La/Yb) have previously been used to infer the degree of partial melting in the source of kimberlites and Kaapvaal lamproites (e.g., Becker and Le Roex, 2006; Coe et al., 2008; Le Roex et al., 2003; Mitchell, 1995). The raised sub-parallel chondrite-normalized LREE patterns of phlogopite-diopside lamproites (Figures 4.13a and b) corresponding with high incompatible trace elements ratios (Gd/Yb = 8.13–9.55; La/Sm = 12.4–13.4; La/Yb = 167–205) relative to leucite-richterite lamproites (Gd/Yb = 6.28–7.73; La/Sm = 10.0–11.0; La/Yb = 101–143) (see Figures 4.12c and d) are consistent with lower degrees of partial melting.

Becker and Le Roex (2006) used La/Sm and Gd/Yb ratios to infer the involvement of low degrees of partial melting in the genesis of Kaapvaal lamproites from the metasomatized peridotite mantle source. From the model of Becker and le Roex (2006), the source mineralogy for lamproites comprises the same proportion of olivine (67%) and orthopyroxene (26%) as the kimberlite source, but with less garnet (1%) and more clinopyroxene (6%) relative to the kimberlite source. The increase in La/Sm and Gd/Yb ratios indicates a decrease in partial melting degree (Becker and Le Roex, 2006; Mitchell, 1995). The trends of the two lamproites varieties from Kareevlei appear to follow the partial melting calculations defined by Becker and Le Roex (2006), with the phlogopite-diopside lamproites having higher La/Sm and Gd/Yb ratios indicating generation by lower degrees of partial melting between 0.1 and 0.5 % relative to leucite-richterite lamproites generated by greater degrees of partial melting between 0.5 and 1 % (see Figure 5.5).

Furthermore, lamproites are commonly interpreted to be generated by the partial melting of metasomatized mantle lithologies, including MARID xenoliths, which have been reported to occur as veins within the peridotitic SCLM (Giuliani et al., 2015; Mitchell, 2006; Mitchell and Bergman, 1991; Bergman, 1987; Mitchell and Edgar, 2002; Xiang et al., 2020). As a result, the partial melting of a MARID-veined peridotitic mantle has been suggested to generate hybridized lamproitic melts (Mitchell and Edgar, 2002). The Kareevlei lamproites record the distinctive history of metasomatized SCLM lithologies preserved by MARID and metasomatized peridotite xenocrystic cores in phlogopite, suggesting that these lamproites have assimilated at least two mantle lithologies (i.e., MARID plus peridotite components) during their formation. Experimental petrology has shown that MARID components tend to melt at higher degrees relative to peridotite components, due to the occurrence of amphiboles (i.e., K-richterite) with lower melting temperatures in the MARID components (e.g., Sweeney et al., 1993; Giuliani et al., 2015). The lower incompatible trace element ratios (La/Yb, Gd/Yb, and La/Sm) in leucite-richterite lamproites indicate higher degrees of partial melting and a higher relative contribution of a MARID-vein component from the SCLM.

In summary, the different incompatible trace element ratios of the Kareevlei lamproite varieties reflect two processes involved during their formation: (1) the relative contribution of the parental source rock (MARID-vein plus peridotite component) to each Kareevlei lamproite variety and (2) the variable partial melting degrees of the parental source rock. Therefore, I suggest that the relative evolution from phlogopite-diopside to leucite-richterite Kareevlei lamproites is more likely controlled by variable degrees of partial melting of an isotopically homogeneous SCLM source, rather than fractional crystallization. This interpretation is supported by nearly constant $^{87}Sr/^{86}Sr_i$ and $^{143}Nd/^{144}Nd_i$ ratios at widely varying La/Yb ratios (Figure 5.6a and b).

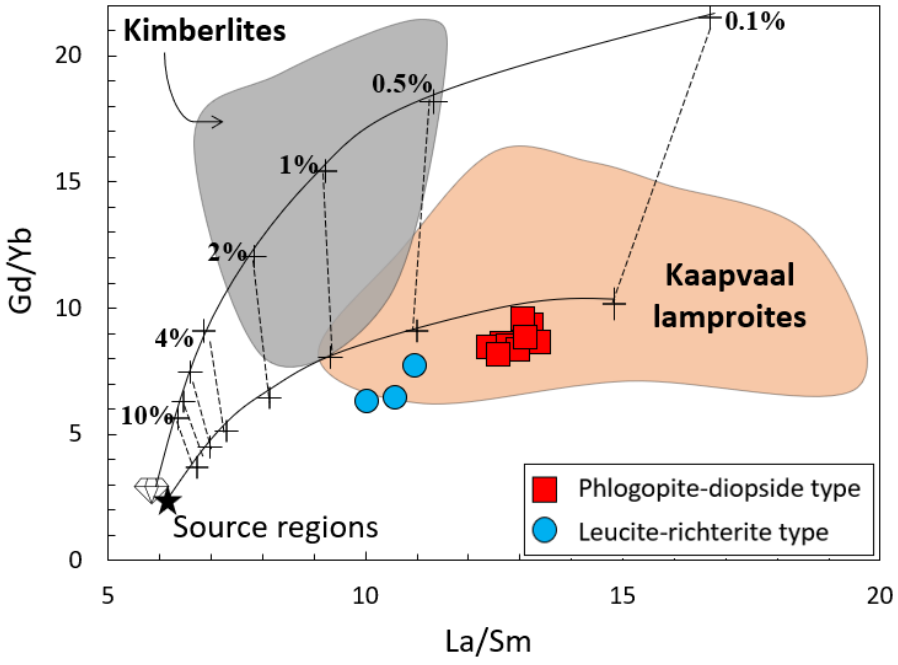

Figure 5. 5: Variation diagram of Gd/Yb vs La/Sm with the partial melting degrees curves of Becker and Le Roex (2006). The gray field of kimberlites was compiled from Harris et al. (2004) and Becker and Le Roex (2006); the Kaapvaal lamproites field was compiled from Becker and Le Roex (2006) and Coe et al. (2008).

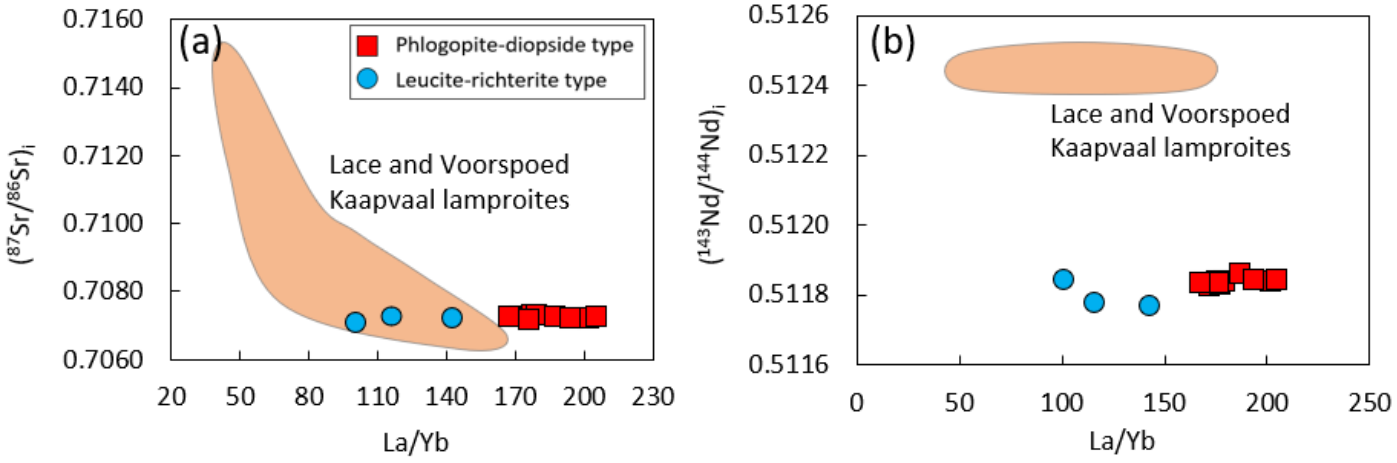

Figure 5. 6: Sr-Nd isotope compositions versus La/Yb ratios of Kareevlei lamproites in comparison to Lace and Voorspoed Kaapvaal lamproites (Howarth et al., 2011).

CHAPTER 6: CONCLUSIONS

The data provided in this study (i.e., petrography, compositions of phlogopite, diopside, and K-richterite, as well as bulk-rock geochemistry) were used to classify and assess the petrogenesis of the uncommon diamondiferous evolved Kaapvaal lamproites from Kareevlei diamond mine. Petrographic evidence shows that these rocks are clearly marked by "evolved mineral suites" (e.g., K-richterite and leucite), which is the recognizable feature of lamproites worldwide and therefore, they are classified as evolved Kaapvaal lamproites. Two distinct mineralogical varieties of Kareevlei Kaapvaal lamproites are classified as (i) phlogopite-diopside lamproites and (ii) leucite-richterite lamproites. These mineralogical varieties identified suggest relative evolution within the Kareevlei pipe, marked by high abundances of olivine macrocrysts and microcrysts (relative to leucite-richterite varieties) and the complete absence of the "evolved mineral suite" in the groundmass of the phlogopite-diopside lamproites.

The primary mineralogy reflects the major element compositions of Kaapvaal lamproites. This is noted in Kareevlei where the leucite-richterite lamproites have raised concentrations of SiO_2, Al_2O_3, and Na_2O, and lowered MgO concentrations relative to phlogopite-diopside lamproites. The major element geochemical trends in Kareevlei lamproites are argued to have not been significantly affected by fractional crystallization, but rather relative mantle xenocryst accumulation.

The Sr–Nd isotope compositions of Kareevlei lamproite mineralogical varieties show no significant variation, thus suggesting that both leucite-richterite and phlogopite-diopside lamproites were derived from an isotopically homogeneous source within the SCLM. The significant differences in incompatible trace elements ratios of these lamproites are regarded as a consequence of the formation of these rocks by variable degrees of partial melting, rather than an isotopically heterogeneous mantle source.

The Ba/Nb, Ce/Pb, and La/Nb ratios exhibit no significant variation between the Kareevlei lamproite mineralogical varieties, instead, these geochemical features simply define them as lamproites. The strong enrichment in La/Yb, Gd/Yb, and La/Sm in the phlogopite-diopside lamproites is clearly linked to the formation of these rocks by lower degrees of partial melting (0.1 to 0.5 %) in the peridotitic mantle source, consistent with partial melting models of Becker and Le Roex (2006). In contrast, the leucite-richterite lamproites are characterized by lower La/Yb, Gd/Yb, and La/Sm ratios associated with the generation of these lamproites by greater degrees of partial melting (0.5 to 1 %).

In conclusion, the data presented in this study supports the hypothesis that Kaapvaal lamproites are generated by partial melting from the MARID-veined peridotitic SCLM (e.g., Becker and le Roex, 2006; Coe et al., 2008; Giuliani et al., 2015). The difference in incompatible trace element ratios reflect variable degrees of partial melting during the generation of the lamproite melts in the source and possibly a secondary control by the relative contribution of MARID-vein material in the source. Therefore, the Kareevlei Kaapvaal lamproites varieties are argued to have been generated by variable degrees of partial melting in an isotopically homogeneous SCLM, rather than evolution through fractional crystallization en route to the surface.

REFERENCES

Arndt, N.T., Guitreau, M., Boullier, A.M., Le Roex, A., Tommasi, A., Cordier, P., Sobolev, A., 2010. Olivine, and the origin of kimberlite. Journal of Petrology 51, 573–602.

Barton, M., van Bergen, M.J. 1981. Green c1inopyroxenes and associated phases in potassium-rich lava from the Leucite Hills, Wyoming. Contributions to Mineralogy and Petrology 77, 101–114.

Becker, M., Le Roex, A.P., 2006. Geochemistry of South African on- and off-craton, group I and group II kimberlites: Petrogenesis and source region evolution. Journal of Petrology 47, 673–703.

Bergman, S.C. 1987. Lamproites and other potassium-rich igneous rocks: a review of their occurrence, mineralogy and geochemistry. Geological Society, London, Special Publications 30, 103–190.

Boettcher, A.L. and O'neil, J.R., 1980. Stable isotope, chemical, and petrographic studies of high-pressure amphiboles and micas: evidence for metasomatism in the mantle source regions of alkali basalts and kimberlites. American Journal of Science 280(A), 594–621.

Boyd, F.R. and Nixon, P.H., 1975. Origins of the ultramafic nodules from some kimberlites of northern Lesotho and the Monastery Mine, South Africa. In Physics and Chemistry of the Earth (431–454). Pergamon.

Chalapathi Rao, N. V, Gibson, S.A., Pyle, D.M. and Dickin, A.P. 2004. Petrogenesis of Proterozoic lamproites and kimberlites from the Cuddapah Basin and Dharwar craton, southern India. Journal of Petrology 45, 907–948.

Clarke, T. C., Smith, C. B., Bristow, J. W., Skinner, E. M. W., Viljoen, K. S., 1991. Isotopic and geochemical variation in kimberlites from the south western craton margin, Prieska area, South Africa. Fifth Int. Kimberlite Conf., Araxa, Brazil. Extended Abstracts. Companhia de Pesquisa de Recursos Minerais, Special Publication 2/91, 46–47.

Çoban, H., Flower, M.F.J., 2006. Mineral phase compositions in silica-undersaturated “leucite” lamproites from the Bucak area, Isparta, SW Turkey. Lithos 89, 275–299.

Coe, N., 2004. Petrogenesis of the Swartruggens and Star Group II kimberlite dyke swarms, South Africa. Master's thesis. University of Cape Town (South A frica).

Coe, N., Le Roex, A., Gurney, J., Pearson, G.D., Nowell, G., 2008. Petrogenesis of the Swartruggens and Star Group II kimberlite dyke swarms, South Africa: Constraints from whole rock geochemistry. Contributions to Mineralogy and Petrology 156, 627–652.

Currie, K.L. and Ferguson, J., 1970. The mechanism of intrusion of lamprophyre dikes indicated by "offsetting" of dikes. Tectonophysics, 9(6), 525–535.

Dawson, J.B., Smith, J.V. 1977. The MARID (mica-amphibole-rutile-ilmenite-diopside) suite of xenoliths in kimberlite. Geochimica et Cosmochimica Acta 41, 309–332.

Dawson, J.B., 1987. The kimberlite clan: relationship with olivine and leucite lamproites, and inferences for upper-mantle metasomatism. Geological Society, London, Special Publications 30(1), 95–101.

Field, M., Stiefenhofer, J., Robey, J., Kurszlaukis, S., 2008. Kimberlite-hosted diamond deposits of southern Africa: A review. Ore Geology Reviews 34, 33–75.

Foley, S.F., 1990. Experimental constraints on phlogopite chemistry in lamproites: 2. Effect of pressure-temperature variations. European Journal of Mineralogy 2, 327–342.

Fraser, K.J. 1988. Petrogenesis of kimberlites from South Africa and lamproites from Western Australia and North America. PhD Thesis. The Open University (United Kingdom).

Fraser, K.J., Hawkesworth, C.J., 1992. The petrogenesis of group 2 ultrapotassic kimberlites from Finsch Mine, South Africa. Lithos 28, 327–345.

Giuliani, A., 2018. Insights into kimberlite petrogenesis and mantle metasomatism from a review of the compositional zoning of olivine in kimberlites worldwide. Lithos 312–313, 322–342.

Giuliani, A., Pearson, D.G, Soltys, A., Dalton, H., Phillips, D., Foley, S.F., Lim, E., Goemann, K., Griffin, W.L., Mitchell, R.H., 2020. Kimberlite genesis from a common carbonate-rich primary melt modified by lithospheric mantle assimilation. Science Advances 6, 1–10.

Giuliani, A., Kamenetsky, V.S., Kendrick, M.A., Phillips, D., Wyatt, B.A., Maas, R., 2013. Oxide, sulphide and carbonate minerals in a mantle polymict breccia: Metasomatism by proto-kimberlite magmas, and relationship to the kimberlite megacrystic suite. Chemical Geology 353, 4–18.

Giuliani, A., Phillips, D., Kamenetsky, V.S., Goemann, K., 2016. Constraints on kimberlite ascent mechanisms revealed by phlogopite compositions in kimberlites and mantle xenoliths. Lithos 240–243, 189–201.

Giuliani, A., Phillips, D., Woodhead, J.D., Kamenetsky, V.S., Fiorentini, M.L., Maas, R., Soltys, A., Armstrong, R.A., 2015. Did diamond-bearing orangeites originate from MARID-veined peridotites in the lithospheric mantle? Nature Communications 6(1), 6837

Grégoire, M., Bell, D., Le Roex, A., 2002. Trace element geochemistry of phlogopite-rich mafic mantle xenoliths: Their classification and their relationship to phlogopite-bearing peridotites and kimberlites revisited. Contributions to Mineralogy and Petrology 142, 603–625.

Grégoire, M., Bell, D.R., Le Roex, A.P., 2003. Garnet lherzolites from the Kaapvaal Craton (South Africa): Trace element evidence for a metasomatic history. Journal of Petrology 44, 629–657.

Grillz, J.A., Lohrentz, C., 2019. Kareevlei mineral resource update for Kareevlei diamonds (Pty) Ltd. Z Star Mineral Resource Consultants (Pty) Ltd.

Gurney, J. J., Ebrahim, S. 1973. Chemical composition of Lesotho kimberlites. In Nixon, P. H. (ed.), Lesotho Kimberlites. Lesotho National Development Corporation, Maseru, Lesotho, 280–294.

Harris, M., Le Roex, A., Class, C., 2004. Geochemistry of the Uintjiesberg kimberlite, South Africa: Petrogenesis of an off-craton, group I, kimberlite. Lithos 74, 149–165.

Howarth, G.H., Giuliani, A., 2020. Contrasting types of micaceous kimberlite-lamproite magmatism from the Man Craton (West Africa): New insights from petrography and mineral chemistry. Lithos 362, 362–323.

Howarth, G.H., Michael, E., Skinner, W., Prevec, S.A., 2011. Petrology of the hypabyssal kimberlite of the Kroonstad group II kimberlite (orangeite) cluster, South Africa: Evolution of the magma within the cluster. Lithos 125, 795–808.

Howarth, G.H., Nembambula, T., 2021. Petrogenesis of Kaapvaal lamproites (aka orangeites) constrained by the composition of olivine and similarities with kimberlites and other diamondiferous lamproites. Lithos 406–407, 106499.

Jaques, A. L., Lewis, J. D., Smith, C. B. 1986. The kimberlites and lamproites of Western Australia. Geological Survey of Western Australia Bull 132, 268.

Kargin, A. V., Nosova, A.A., Larionova, Y.O., Kononova, V.A., Borisovsky, S.E., Koval'chuk, E. V., Griboedova, I.G., 2014. Mesoproterozoic orangeites (Kimberlites II) of West Karelia: Mineralogy, geochemistry, and Sr-Nd isotope composition. Petrology Boston 22, 151–183.

Konzett, J., 1997. Phase relations and chemistry of Ti-rich K-richterite-bearing mantle assemblages: an experimental study to 8.0 GPa in a Ti-KNCMASH system. Contributions to Mineralogy and Petrology 128, 385–404.

Kopylova, M.G., Mogg, T. and Scott Smith, B., 2010. Mineralogy of the Snap Lake kimberlite, Northwest Territories, Canada, and compositions of phlogopite as records of its crystallization. The Canadian Mineralogist 48(3), 549–570.

Le Roex, A.P., Bell, D.R., Davis, P., 2003. Petrogenesis of group I Kimberlites from Kimberley, South Africa: Evidence from bulk-rock geochemistry. Journal of Petrology 44, 2261–2286.

Mirnejad, H., Bell, K., 2006. Origin and source evolution of the Leucite Hills lamproites: Evidence from Sr-Nd-Pb-O isotopic compositions. Jounal of Petrology 47, 2463–2489.

Mitchell, R.H., 2006. Potassic magmas derived from metasomatized lithospheric mantle: Nomenclature and relevance to exploration for diamond-bearing rocks. Journal of Geological Society of India 67, 317–327.

Mitchell, R.H., 1995. Kimberlites, Orangeites, and Related Rocks. Springer Science & Business Media.

Mitchell, R.H., Bergman, S.C., 1991. Petrology of lamproites. Springer Science & Business Media.

Mitchell, R.H., Edgar, A.D., 2002. Melting experiments on SiO_2-rich lamproites to 6.4 GPa and their bearing on the sources of lamproite magmas. Mineralogy and Petrology 74, 115–128.

Pasteris, J.D., 1983. Spinel zonation in the De Beers kimberlite, South Africa: possible role of phlogopite. Canadian Mineralogy 21(1), 41–58.

Pearson, D.G., Woodhead, J., Janney, P.E., 2019. Kimberlites as geochemical probes of earth's mantle. Elements 15, 387–392.

Prelević, D., Foley, S.F., Romer, R. and Conticelli, S., 2008. Mediterranean Tertiary lamproites derived from multiple source components in postcollisional geodynamics. Geochimica et Cosmochimica Acta 72(8), 2125–2156.

Ramokgaba, L., Le Roex, A., Robey, J., 2021. Phlogopite-rich and phlogopite-poor kimberlite intrusions within the Du Toitspan kimberlite pipe, South Africa: Petrogenetic relationships and localised source heterogeneity. Lithos 390–391, 106125.

Robey, J., 1981. Kimberlites of the Central Cape Province, RSA. PhD Thesis. University of Cape Town (South Africa).

Shaikh, A.M., Patel, S.C., Ravi, S., Behera, D., Pruseth, K.L., 2017. Mineralogy of the TK1 and TK4 'kimberlites' in the Timmasamudram cluster, Wajrakarur Kimberlite Field, India: Implications for lamproite magmatism in a field of kimberlites and ultramafic lamprophyres. Chemical Geology 455, 208–230.

Shaikh, A.M., Kumar, S.P., Patel, S.C., Thakur, S.S., Ravi, S. and Behera, D. 2018. The P3 kimberlite and P4 lamproite, Wajrakarur kimberlite field, India: mineralogy, and major and minor element compositions of olivines as records of their phenocrystic vs xenocrystic origin. Mineralogy and Petrology 112, 609–624.

Skinner, E.M.W. 1989. Contrasting group I and II kimberlite petrology: Towards a genetic model for kimberlites. In International Kimberlite Conference: Extended Abstract (Volume 4, 202–204)

Skinner E. M. W., Clement, C. R., Gurney, J. J., Apter, D. B., Hatton, C. J. 1992. The distribution and tectonic setting of South African kimberlites. Russian Geology and Geophysics 33, 26–31.

Skinner, E.M.W., 1994. The petrography, tectonic setting and emplacement ages of kimberlites in the southwestern border region of the Kaapvaal craton, Prieska area. In Kimberlites, Related Rocks and Mantle Xenoliths. Proceedings of the International Kimberlite Conference, 5th, Araxa, Brazil, 1994 (Volume 1, 80–97).

Scott Smith, B.S., 2017, September. Kimberlites–from mantle to mine. In International Kimberlite Conference: Extended Abstracts (Volume 11).

Smith, C.B., 1983. Pb, Sr and Nd isotopic evidence for sources of southern African Cretaceous kimberlites. Nature Communications 304, 51–54.

Smith, C. B., Allsopp, H. L., Kramers, J. D., Hutchinson, G., Roddick, J. C. 1985. Emplacement ages of Jurassic-Cretaceous South African kimberlites by the Rb-Sr method on phlogopite and whole rock samples. Transactions of the Geological Society of South Africa 88, 249–266.

Smith, C. B., Clark, T. C., Barton, E. S., Bristow, J. W. 1994. Emplacement ages of kimberlite occurrences in the Prieska region, southwest border of the Kaapvaal craton, South Africa. Chemical Geology. (Isotope Geoscience Section) 113, 149–169.

Sun, S.-S. and McDonough, W.F. 1989. Chemical and isotopic systematics of oceanic basalts: implications for mantle composition and processes. Geological Society, London, Special Publications 42, 313–345.

Sweeney, R.J., Thompson, A.B., Ulmer, P., 1993. Phase relations of a natural MARID composition and implications for MARID genesis, lithospheric melting and mantle metasomatism. Contributions to Mineralogy and Petrology 115, 225–241.

Tainton, K.M., 1992. The petrogenesis of group-2 kimberlites and lamproites from the Northern Cape Province, South Africa. PhD Thesis. University of Cambridge.

Talukdar, D., Pandey, A., Chalapathi Rao, N. v, Kumar, A., Pandit, D., Belyatsky, B. and Lehmann, B. 2018. Petrology and geochemistry of the Mesoproterozoic Vattikod lamproites, Eastern Dharwar Craton, southern India: evidence for multiple enrichment of sub-continental lithospheric mantle and links with amalgamation and break-up of the Columbia supercontinent. Contributions to Mineralogy and Petrology 173.

Taylor, W.R., Kingdom, L., 1999. Mineralogy of the Jagersfontein kimberlite-an unusual group 1 micaceous kimberlite-and a comment on the robustness of the mineralogical definition of 'orangeite'. In: Proceedings of the 7th International Kimberlite Conference, Vol.1. Red Roof Design, CapeTown, 861–866.

Tovey, M., Giuliani, A., Phillips, D., Pearson, D.G., Sarkar, C., Nowicki, T. and Carlson, J., 2021. The spatial and temporal evolution of primitive melt compositions within the Lac de Gras kimberlite field, Canada: Source evolution vs lithospheric mantle assimilation. Lithos 392, 106142.

Viljoen, A., Howarth, G.H., Giuliani, A., Fitzpayne, A., Costin, G., 2022. Correlations between olivine composition and groundmass mineralogy in Sierra Leone kimberlites provide constraints on craton-specific melt-lithosphere interactions. Lithos 430–431, 106846.

Wagner, P.A., 1914. The diamond fields of southern Africa. Transvaal leader.

Wagner, C., Velde, D., 1986. The mineralogy of K-richterite-bearing lamproites. American Mineralogist 71, 17–37.

Winter, J.D. (2001) An Introduction to Igneous and Metamorphic Petrology. Prentice Hall Inc., Upper Saddle River 697.

Woodhead, J., Hergt, J., Giuliani, A., Maas, R., Phillips, D., Pearson, D.G., Nowell, G., 2019. Kimberlites reveal 2.5-billion-year evolution of a deep, isolated mantle reservoir. Nature Communications 573, 578–581.

Woolley, A.R., Bergman, S.C., Edgar, A.D., Le Bas, M.J., Mitchell, R.H., Rock, N.M.S., Scott Smith, B.H, 1996. Classification of lamprophyres, lamproites, kimberlites, and the kalsilitic, melilitic, and leucitic rocks. Canadian Mineralogist 34, 175–186.

Xiang, L., Zheng, J., Zhai, M., Siebel, W., 2020. Geochemical and Sr–Nd–Pb isotopic constraints on the origin and petrogenesis of Paleozoic lamproites in the southern Yangtze Block, South China. Contributions to Mineralogy and Petrology 175, 1–18.

APPENDICES

Appendix 1: Major element compositions (wt.%) of phlogopite from Kareevlei lamproites.

	F	Na_2O	MgO	Al_2O_3	SiO_2	K_2O	FeO	MnO	TiO_2	BaO	Cl	CaO	Cr_2O_3	Total
CORES							**Sample KRV2**							
	0.60	0.08	24.2	11.9	41.3	9.97	4.69	0.00	2.25	0.46	0.00	0.08	1.24	96.66
	1.06	0.08	24.3	12.3	41.4	9.98	4.29	0.04	2.59	0.35	0.01	0.04	1.51	97.86
	0.97	0.13	23.7	10.1	44.0	9.06	5.05	0.01	2.67	0.14	0.01	0.05	0.38	96.26
	1.04	0.08	22.8	11.6	39.9	9.84	4.65	0.02	2.60	0.24	0.00	0.20	1.30	94.31
	0.76	0.06	25.6	10.1	42.8	7.93	3.61	0.05	2.25	0.15	0.01	0.07	1.31	94.62
	0.97	0.05	22.6	12.1	42.8	9.50	4.33	0.02	2.41	0.39	0.00	0.09	1.24	96.44
RIMS &														
GROUNDMASS PHLOGOPITE														
	0.76	0.11	20.1	9.56	40.3	9.85	9.64	0.08	5.86	0.60	0.00	0.10	0.05	96.93
	0.91	0.10	20.3	10.2	39.0	9.44	8.15	0.08	5.52	0.89	0.02	0.04	0.06	94.77
	0.90	0.08	20.5	10.3	41.2	9.74	7.97	0.07	5.40	0.63	0.00	0.08	0.03	96.94
	0.76	0.09	20.3	9.90	41.0	9.72	8.60	0.06	5.97	0.63	0.01	0.08	0.00	97.17
	0.92	0.09	20.9	9.60	41.5	9.34	7.66	0.06	5.93	0.59	0.00	0.07	0.00	96.69
	0.70	0.09	19.1	8.74	42.6	9.42	8.80	0.02	5.91	0.40	0.01	0.14	0.14	96.03
	0.98	0.15	20.4	8.43	40.4	9.77	8.73	0.07	5.88	0.82	0.01	0.03	0.03	95.73
	0.83	0.16	20.3	8.25	40.0	9.9	9.11	0.08	6.33	0.70	0.01	0.05	0.02	95.74
	0.84	0.14	19.7	8.18	40.0	9.89	9.46	0.10	5.94	0.61	0.02	0.05	0.05	95.00
	0.86	0.19	20.0	8.48	39.7	9.25	8.91	0.05	5.8	0.75	0.00	1.11	0.07	95.17
	0.63	0.10	21.4	9.11	41.4	8.59	8.66	0.08	5.74	0.54	0.00	0.2	0.22	96.59
	0.75	0.10	19.3	8.26	40.2	9.64	9.97	0.08	6.11	0.64	0.00	0.14	0.08	95.28
	0.84	0.09	19.4	8.74	40.7	9.82	9.71	0.08	6.17	0.6	0.00	0.06	0.05	96.29
	0.76	0.07	20.3	9.28	40.3	9.91	9.11	0.08	6.43	0.77	0.00	0.12	0.00	97.09

	F	Na_2O	MgO	Al_2O_3	SiO_2	K_2O	FeO	MnO	TiO_2	BaO	Cl	CaO	Cr_2O_3	Total
GROUNDMASS							**Sample KRV3**							
Phl														
	1.46	0.26	20.5	10.8	39.2	9.76	6.85	0.02	5.82	0.84	0.00	0.08	0.63	96.27
	1.18	0.24	19.9	9.8	39.5	9.50	7.58	0.05	6.59	0.65	0.02	0.20	0.18	95.30
	1.26	0.23	19.1	8.80	38.9	9.62	8.83	0.07	6.28	0.56	0.01	0.16	0.00	93.77
	0.75	0.23	19.2	9.00	39.5	9.49	9.57	0.03	6.34	0.67	0.00	0.11	0.03	94.98
	0.96	0.23	20.8	10.5	40.9	9.50	7.21	0.04	6.28	0.65	0.01	0.17	0.32	97.51
	1.26	0.27	21.1	6.49	40.9	9.49	8.03	0.06	6.57	0.46	0.01	0.20	0.04	94.83
	1.25	0.24	20.9	10.4	40.3	9.70	7.22	0.04	5.94	0.70	0.01	0.08	0.52	97.34
	1.10	0.21	20.2	10.5	39.3	9.59	7.24	0.06	5.86	0.73	0.00	0.15	0.77	95.58

	F	Na_2O	MgO	Al_2O_3	SiO_2	K_2O	FeO	MnO	TiO_2	BaO	Cl	CaO	Cr_2O_3	Total
CORES							**Sample KRV5**							
	0.63	0.09	23.6	11.8	40.2	10.3	4.06	0.04	2.33	0.29	0.00	0.00	1.48	94.93
	0.81	0.04	23.6	11.5	40.1	10.3	4.66	0.01	2.57	0.31	0.00	0.03	1.31	95.24
	0.81	0.05	23.2	11.4	40.1	10.4	4.29	0.00	2.62	0.38	0.00	0.06	1.40	94.65
	1.06	0.07	22.3	10.6	39.6	10.2	5.29	0.02	4.22	0.83	0.01	0.01	0.44	94.58
	0.53	0.09	25.4	10.4	40.3	8.68	4.15	0.00	2.01	0.34	0.01	0.04	1.28	93.20
	0.85	0.07	24.5	9.95	40.4	9.76	5.33	0.05	3.02	0.38	0.01	0.01	0.13	94.41
	0.94	0.07	24.7	10.2	40.1	9.33	4.83	0.02	2.93	0.38	0.00	0.07	0.33	93.86
	0.85	0.08	24.1	9.42	40.5	8.57	6.25	0.06	3.95	0.67	0.01	0.10	0.15	94.68
RIMS														
	0.49	0.20	20.2	6.33	40.3	9.7	12.2	0.12	3.35	0.12	0.00	0.19	0.08	93.31
	0.77	0.05	22.1	9.65	40.4	10.1	7.44	0.07	4.42	0.61	0.00	0.04	0.2	95.90
	0.57	0.12	21.1	8.08	40.2	10.1	9.41	0.08	4.61	0.53	0.00	0.08	0.06	94.84
	0.71	0.09	21.5	9.55	39.2	10.1	7.29	0.07	4.66	0.53	0.00	0.11	0.15	93.95
	0.84	0.13	21.0	8.92	38.0	9.88	7.65	0.08	4.86	0.66	0.02	0.08	0.18	92.23
	0.32	0.17	19.9	6.28	40.1	9.34	12.9	0.13	4.43	0.53	0.00	0.06	0.01	94.25
	0.42	0.33	21.4	3.30	41.5	9.63	14.8	0.19	3.50	0.24	0.00	0.27	0.04	95.61
	0.71	0.09	21.9	9.39	40.3	9.96	7.35	0.06	4.69	0.51	0.01	0.07	0.13	95.20

	F	Na_2O	MgO	Al_2O_3	SiO_2	K_2O	FeO	MnO	TiO_2	BaO	Cl	CaO	Cr_2O_3	Total
CORES							**Sample KRV6**							
	0.18	0.20	26.1	9.68	42.0	8.15	4.49	0.06	0.72	0.18	0.03	0.04	0.48	92.29
	0.51	0.06	23.6	11.8	40.1	10.3	4.17	0.02	2.21	0.30	0.01	0.03	1.50	94.60
	0.41	0.18	25.4	11.3	42.1	10.5	2.69	0.01	0.38	0.20	0.03	0.02	0.68	93.88
	0.69	0.04	23.6	11.8	40.3	10.4	3.88	0.04	2.18	0.24	0.00	0.03	1.54	94.81
	0.36	0.07	26.8	9.43	40.6	7.85	3.53	0.02	1.86	0.24	0.00	0.06	1.01	91.88
	0.45	0.09	28.5	8.58	42.3	7.82	3.65	0.02	1.75	0.24	0.00	0.07	0.52	93.99
	0.26	0.31	24.9	10.1	42.4	10.6	3.61	0.01	0.70	0.14	0.02	0.01	0.44	93.47
	0.40	0.05	23.4	10.4	40.6	10.6	5.82	0.05	2.34	0.23	0.00	0.02	0.04	94.02
	0.52	0.03	23.5	11.5	40.2	10.5	3.79	0.03	2.27	0.20	0.00	0.02	1.97	94.37
	0.49	0.07	23.5	11.6	40.2	10.3	4.22	0.02	2.17	0.28	0.00	0.05	1.44	94.35
	0.45	0.04	22.6	12.7	39.1	9.86	5.84	0.03	2.55	0.69	0.01	0.02	0.11	94.05
	0.15	0.05	21.5	15.2	36.2	8.23	9.02	0.09	0.44	0.32	0.00	0.07	0.11	91.31
	0.28	0.14	26.7	9.30	39.8	6.04	7.24	0.04	0.45	0.10	0.01	0.03	0.27	90.43
RIMS														
	0.78	0.05	23.3	8.02	40.7	10.1	8.40	0.06	2.69	0.57	0.00	0.09	0.09	94.81
	0.80	0.06	22.7	7.14	40.18	10.1	9.50	0.08	2.60	0.57	0.00	0.11	0.04	93.87
	0.95	0.08	22.8	10.5	41.07	10.1	6.93	0.06	2.74	0.71	0.01	0.18	0.22	96.27
	0.88	0.05	23.8	9.76	40.64	10.0	6.11	0.05	2.88	0.73	0.00	0.08	0.24	95.27
	1.09	0.07	23.0	8.73	39.66	10.0	7.38	0.08	2.79	0.74	0.00	0.06	0.19	93.78
	1.13	0.07	23.3	9.78	40.11	10.2	6.15	0.06	3.30	0.70	0.00	0.07	0.22	95.11
	0.91	0.07	23.1	8.63	39.86	10.1	7.32	0.03	2.92	0.68	0.00	0.05	0.17	93.86
	1.03	0.05	23.1	9.03	40.0	10.0	7.71	0.12	2.88	0.94	0.01	0.04	0.15	94.99
	1.04	0.05	22.1	10.3	40.08	10.8	7.11	0.09	2.63	0.74	0.00	0.04	0.14	95.12
	0.87	0.05	23.5	10.3	40.21	10.2	5.90	0.07	2.72	0.53	0.01	0.05	0.53	94.93
	1.21	0.05	23.5	9.23	39.86	10.0	6.64	0.08	2.71	0.71	0.00	0.02	0.21	94.26
	0.84	0.05	22.5	6.42	39.33	10.0	11.6	0.14	2.01	0.60	0.00	0.05	0.00	93.58
	0.97	0.08	23.3	8.08	40.0	9.94	8.34	0.07	2.45	0.51	0.00	0.04	0.12	93.92

	F	Na_2O	MgO	Al_2O_3	SiO_2	K_2O	FeO	MnO	TiO_2	BaO	Cl	CaO	Cr_2O_3	Total
CORES							**Sample KRV9**							
	0.42	0.15	24.5	9.61	41.57	9.98	5.63	0.04	2.19	0.17	0.01	0.05	0.15	94.48
	0.26	0.30	24.2	11.0	43.0	10.5	3.90	0.03	1.00	0.09	0.02	0.00	0.25	94.55
	0.46	0.06	24.5	11.1	40.18	9.27	3.89	0.00	2.05	0.27	0.00	0.05	1.46	93.28
	0.83	0.08	23.6	11.4	40.59	10.2	4.45	0.02	2.52	0.25	0.01	0.06	1.24	95.25
	0.66	0.12	24.7	10.7	40.5	9.66	4.51	0.02	2.37	0.33	0.01	0.04	0.93	94.53
	0.66	0.10	23.7	11.4	40.16	10.1	4.19	0.02	2.32	0.35	0.00	0.03	1.39	94.45
	0.62	0.06	23.9	11.1	40.0	10.3	4.41	0.03	2.38	0.34	0.01	0.03	1.08	94.24
	0.52	0.06	23.4	11.2	40.22	10.3	4.67	0.04	2.69	0.30	0.02	0.02	0.99	94.41
	0.29	0.08	28.9	7.30	42.0	5.74	4.44	0.03	1.84	0.20	0.01	0.14	0.07	90.95
	0.53	0.12	24.0	10.2	41.46	10.4	5.09	0.02	2.49	0.25	0.01	0.02	0.23	94.81
	0.56	0.12	23.9	11.5	40.42	9.74	4.56	0.00	2.35	0.37	0.01	0.11	1.31	95.00
	0.61	0.07	23.9	10.7	40.85	10.3	4.61	0.01	2.20	0.15	0.01	0.03	0.51	93.91
	0.47	0.08	23.9	11.2	40.88	10.2	4.03	0.00	2.24	0.09	0.00	0.05	1.24	94.44
	0.63	0.09	24.9	11.0	40.87	9.75	4.55	0.04	2.47	0.32	0.00	0.06	0.89	95.53
RIMS														
	0.78	0.12	23.2	8.87	41.0	9.32	7.27	0.08	4.13	0.63	0.01	0.08	0.10	95.53
	1.13	0.09	21.4	9.22	39.4	10.0	6.95	0.04	4.00	0.66	0.00	1.00	0.14	93.98
	0.80	0.09	22.0	9.25	39.9	9.94	7.22	0.05	4.54	0.62	0.01	0.07	0.13	94.61
	0.80	0.11	22.2	9.00	40.3	9.87	7.53	0.06	4.37	0.63	0.00	0.12	0.09	95.13
	0.83	0.13	22.3	8.63	40.7	9.77	8.26	0.08	4.18	0.57	0.01	0.05	0.07	95.56
	0.53	0.12	24.3	8.47	41.7	8.29	6.94	0.10	3.59	0.60	0.00	0.15	0.13	94.87
	0.73	0.10	22.2	9.16	40.1	9.82	7.37	0.05	4.32	0.64	0.01	0.06	0.14	94.68
	0.87	0.08	22.7	9.00	40.5	10.3	7.97	0.08	3.46	0.39	0.00	0.04	0.08	95.42
	0.49	0.10	23.3	10.0	40.8	9.34	7.01	0.06	3.06	0.38	0.01	0.12	0.11	94.81
	0.72	0.13	21.6	9.35	40.6	9.85	7.92	0.10	4.47	0.50	0.00	0.10	0.15	95.50
	0.94	0.12	22.3	9.49	40.4	9.92	7.27	0.06	4.27	0.59	0.00	0.03	0.13	95.41
	1.06	0.12	21.4	8.90	39.7	9.64	8.07	0.07	4.68	0.80	0.02	0.07	0.07	94.51
	0.70	0.11	22.1	9.74	39.4	9.89	6.83	0.09	4.38	0.84	0.02	0.06	0.33	94.45
	0.76	0.11	23.1	10.1	40.3	9.97	5.85	0.05	3.52	0.52	0.01	0.08	0.20	94.50
	0.28	0.59	20.1	4.98	46.9	5.09	7.12	0.14	2.41	0.25	0.00	10.0	0.15	98.05
	0.64	0.20	21.9	8.20	40.7	9.25	8.52	0.17	3.30	0.46	0.02	0.81	0.36	94.45

	F	Na_2O	MgO	Al_2O_3	SiO_2	K_2O	FeO	MnO	TiO_2	BaO	Cl	CaO	Cr_2O_3	Total
CORES							**Sample KRV12**							
	0.64	0.06	23.2	11.8	41.2	10.4	4.65	0.06	2.25	0.29	0.00	0.00	1.37	95.86
	0.64	0.06	23.4	12.0	41.3	10.3	4.21	0.04	2.44	0.41	0.01	0.04	1.51	96.25
	0.59	0.06	23.2	11.7	41.1	10.1	4.31	0.05	2.40	0.41	0.01	0.05	1.37	95.41
	0.75	0.06	23.6	11.5	42.0	10.3	4.49	0.00	2.59	0.21	0.00	0.02	0.57	96.06
	0.43	0.08	23.0	11.9	42.0	10.0	4.38	0.07	1.34	0.26	0.05	0.04	0.47	94.07
	1.00	0.06	23.2	11.2	41.9	10.4	4.41	0.03	2.59	0.29	0.02	0.05	1.14	96.31
	0.77	0.05	23.4	11.9	41.7	10.2	4.48	0.04	2.32	0.29	0.00	0.05	1.42	96.57
	0.78	0.06	23.4	11.7	41.4	10.4	4.36	0.02	2.36	0.32	0.01	0.04	1.66	96.49
	0.68	0.09	23.5	10.3	41.7	10.3	4.83	0.05	2.55	0.36	0.00	0.03	0.89	95.22
	0.96	0.07	23.8	11.7	41.0	10.1	4.46	0.03	2.34	0.39	0.00	0.04	1.54	96.35
	0.69	0.08	23.3	11.6	41.1	10.3	4.28	0.00	2.45	0.27	0.00	0.03	1.68	95.74
	0.66	0.06	23.4	11.8	40.9	10.3	4.39	0.04	2.42	0.34	0.00	0.04	1.67	95.99
	0.66	0.05	23.4	11.8	41.0	10.4	4.24	0.03	2.43	0.39	0.01	0.02	1.57	96.02
	0.66	0.08	23.8	9.78	42.2	10.3	6.14	0.06	2.93	0.32	0.00	0.02	0.37	96.58
	1.13	0.08	23.4	10.0	42.4	10.4	5.97	0.03	2.41	0.16	0.00	0.01	0.22	96.22
	0.77	0.05	23.4	12.2	41.4	10.2	4.32	0.06	2.50	0.41	0.00	0.04	1.54	96.84
	0.80	0.07	23.0	12.1	41.6	10.1	4.09	0.01	2.24	0.31	0.01	0.06	1.65	95.92
	0.70	0.09	23.2	11.7	41.4	10.1	4.58	0.04	2.40	0.35	0.00	0.05	1.33	95.95
	0.62	0.11	23.0	11.9	41.2	10.1	4.62	0.03	2.37	0.34	0.00	0.06	1.62	95.91
	0.51	0.07	23.5	11.8	41.6	10.4	4.35	0.00	2.34	0.20	0.01	0.01	1.40	96.12
	0.64	0.08	23.1	11.7	41.5	10.2	4.31	0.01	2.33	0.25	0.00	0.04	1.50	95.60
RIMS														
	0.90	0.06	21.2	9.91	41.07	9.98	7.46	0.05	4.81	0.77	0.00	0.05	0.28	96.57
	1.08	0.08	21.1	8.91	40.68	9.91	7.88	0.03	4.98	0.79	0.00	0.24	0.07	95.75
	0.95	0.08	21.3	9.91	40.55	9.88	7.25	0.06	4.95	0.91	0.01	0.05	0.29	96.21
	0.92	0.07	21.2	9.99	40.83	10.0	7.82	0.09	5.30	0.93	0.01	0.07	0.27	97.47
	0.86	0.07	21.5	9.68	41.26	9.84	7.51	0.01	4.67	0.97	0.00	0.09	0.23	96.67
	1.09	0.08	21.2	9.01	40.84	9.74	8.71	0.09	5.16	0.74	0.01	0.04	0.02	96.76
	0.95	0.10	20.8	9.52	41.0	9.65	8.11	0.05	5.56	0.90	0.00	0.11	0.25	97.01
	1.03	0.06	21.2	9.07	41.13	9.46	7.50	0.05	4.73	0.81	0.00	0.29	0.15	95.49
	0.98	0.06	21.2	10.1	40.55	9.86	7.63	0.07	4.95	0.89	0.01	0.06	0.25	96.63
	0.92	0.08	21.1	9.06	40.33	9.86	8.01	0.08	4.98	0.72	0.00	0.09	0.19	95.39
	0.90	0.08	20.9	10.1	40.68	9.99	7.52	0.05	5.08	0.83	0.00	0.06	0.26	96.44
	1.08	0.07	21.5	9.98	40.76	10.1	7.42	0.10	4.7	0.84	0.00	0.05	0.2	96.79
	1.05	0.07	21.9	9.05	40.94	9.79	7.94	0.05	4.62	0.72	0.02	0.2	0.07	96.41
	0.94	0.06	21.5	9.20	41.28	9.86	7.94	0.04	4.92	0.63	0.00	0.08	0.12	96.56
	0.83	0.09	20.6	10.1	40.66	9.68	8.90	0.08	5.37	1.04	0.00	0.02	0.16	97.53
	0.87	0.09	21.4	9.93	40.45	9.83	7.29	0.06	5.11	0.80	0.01	0.06	0.26	96.11
	0.93	0.08	21.1	9.14	40.87	10.1	8.40	0.08	4.67	0.82	0.00	0.07	0.15	96.34
	0.96	0.11	21.6	8.65	41.24	9.73	8.57	0.09	4.58	0.71	0.01	0.12	0.05	96.46
	0.95	0.06	21.0	10.0	40.55	9.76	7.87	0.10	5.19	0.94	0.01	0.03	0.24	96.67
	0.82	0.08	20.8	10.2	40.3	9.79	7.66	0.04	5.24	1.05	0.00	0.10	0.18	96.22
	0.93	0.09	21.4	9.42	41.42	9.67	7.35	0.06	4.82	0.77	0.02	0.08	0.14	96.21
	1.01	0.10	21.2	9.92	40.52	9.71	7.86	0.06	5.09	0.95	0.02	0.06	0.32	96.80
	1.00	0.07	21.5	9.97	40.44	9.92	7.33	0.06	4.96	0.81	0.00	0.04	0.28	96.35
	0.98	0.06	21.7	9.52	40.91	9.96	7.40	0.10	4.68	0.72	0.00	0.04	0.11	96.16

	F	Na_2O	MgO	Al_2O_3	SiO_2	K_2O	FeO	MnO	TiO_2	BaO	Cl	CaO	Cr_2O_3	Total
RIMS					**Sample KRV12**									
	0.90	0.06	21.2	9.91	41.07	9.98	7.46	0.05	4.81	0.77	0.00	0.05	0.28	96.57
	1.08	0.08	21.1	8.91	40.68	9.91	7.88	0.03	4.98	0.79	0.00	0.24	0.07	95.75
	0.95	0.08	21.3	9.91	40.55	9.88	7.25	0.06	4.95	0.91	0.01	0.05	0.29	96.21
	0.92	0.07	21.2	9.99	40.83	10.0	7.82	0.09	5.30	0.93	0.01	0.07	0.27	97.47
	0.86	0.07	21.5	9.68	41.26	9.84	7.51	0.01	4.67	0.97	0.00	0.09	0.23	96.67
	1.09	0.08	21.2	9.01	40.84	9.74	8.71	0.09	5.16	0.74	0.01	0.04	0.02	96.76
	0.95	0.10	20.8	9.52	41.0	9.65	8.11	0.05	5.56	0.90	0.00	0.11	0.25	97.01
	1.03	0.06	21.2	9.07	41.13	9.46	7.50	0.05	4.73	0.81	0.00	0.29	0.15	95.49
	0.98	0.06	21.2	10.1	40.55	9.86	7.63	0.07	4.95	0.89	0.01	0.06	0.25	96.63
	0.92	0.08	21.1	9.06	40.33	9.86	8.01	0.08	4.98	0.72	0.00	0.09	0.19	95.39
	0.90	0.08	20.9	10.1	40.68	9.99	7.52	0.05	5.08	0.83	0.00	0.06	0.26	96.44
	1.08	0.07	21.5	9.98	40.76	10.1	7.42	0.10	4.7	0.84	0.00	0.05	0.2	96.79
	1.05	0.07	21.9	9.05	40.94	9.79	7.94	0.05	4.62	0.72	0.02	0.2	0.07	96.41
	0.94	0.06	21.5	9.20	41.28	9.86	7.94	0.04	4.92	0.63	0.00	0.08	0.12	96.56
	0.83	0.09	20.6	10.1	40.66	9.68	8.90	0.08	5.37	1.04	0.00	0.02	0.16	97.53
	0.87	0.09	21.4	9.93	40.45	9.83	7.29	0.06	5.11	0.80	0.01	0.06	0.26	96.11
	0.93	0.08	21.1	9.14	40.87	10.1	8.40	0.08	4.67	0.82	0.00	0.07	0.15	96.34
	0.96	0.11	21.6	8.65	41.24	9.73	8.57	0.09	4.58	0.71	0.01	0.12	0.05	96.46
	0.95	0.06	21.0	10.0	40.55	9.76	7.87	0.10	5.19	0.94	0.01	0.03	0.24	96.67
	0.82	0.08	20.8	10.2	40.3	9.79	7.66	0.04	5.24	1.05	0.00	0.10	0.18	96.22
	0.93	0.09	21.4	9.42	41.42	9.67	7.35	0.06	4.82	0.77	0.02	0.08	0.14	96.21
	1.01	0.10	21.2	9.92	40.52	9.71	7.86	0.06	5.09	0.95	0.02	0.06	0.32	96.80
	1.00	0.07	21.5	9.97	40.44	9.92	7.33	0.06	4.96	0.81	0.00	0.04	0.28	96.35
	0.98	0.06	21.7	9.52	40.91	9.96	7.40	0.10	4.68	0.72	0.00	0.04	0.11	96.16

Appendix 2: Major element compositions (in wt.%) of K-richterite from Kareevlei lamproites.

Number of grains	1	2	3	4	5	6	7
			KRV2				
SiO_2	54.5	55.2	53.7	53.8	53.6	52.8	53.8
TiO_2	3.39	3.77	3.71	4.18	3.84	5.13	3.86
Al_2O_3	0.59	0.70	0.73	0.48	0.58	0.57	0.50
Cr_2O_3	0.05	0.04	0.05	0.04	0.02	0.00	0.09
FeO	5.36	6.32	5.78	6.78	5.76	8.87	6.70
MnO	0.10	0.10	0.11	0.14	0.12	0.15	0.11
MgO	18.9	18.9	18.6	18.1	18.8	16.4	18.0
CaO	4.89	4.00	4.73	3.92	4.79	2.62	4.28
BaO	0.00	0.03	0.02	0.00	0.02	0.00	0.02
Na_2O	4.98	5.55	4.73	5.44	4.90	6.09	5.12
K_2O	4.68	4.60	4.73	4.77	4.80	4.78	4.77
Cl	0.00	0.02	0.01	0.00	0.01	0.00	0.00
F	0.89	0.50	0.81	0.83	0.91	0.71	0.70
Total	98.4	99.7	97.7	98.5	98.0	98.2	97.9
Cations bases on 22 oxygens							
Si	7.447	7.430	7.402	7.393	7.272	7.375	7.344
Ti	0.348	0.381	0.384	0.432	0.356	0.398	0.537
Al	0.095	0.111	0.118	0.078	0.305	0.094	0.093
Cr	0.005	0.004	0.005	0.004	0.001	0.002	0.000
Fe	0.612	0.711	0.666	0.779	0.549	0.663	1.032
Mn	0.012	0.011	0.013	0.016	0.011	0.014	0.018
Mg	3.852	3.786	3.817	3.709	4.132	3.849	3.411
Ca	0.716	0.577	0.698	0.577	0.707	0.707	0.391
Ba	0.000	0.002	0.001	0.000	0.002	0.001	0.000
Na	1.319	1.448	1.263	1.450	1.072	1.308	1.643
K	0.815	0.789	0.831	0.837	0.698	0.843	0.849
F	0.664	0.367	0.609	0.623	0.551	0.685	0.540
Cl	0.000	0.006	0.003	0.000	0.003	0.003	0.000
Total	15.22	15.25	15.20	15.28	15.10	15.25	15.32
Calculated ratios							
Na/K	1.62	1.83	1.52	1.73	1.54	1.55	1.94

Appendix 3: Major element compositions (wt.%) of diopside from Kareevlei lamproites.

Number of points	1	2	3	4	5	6	7
			Sample KRV2				
SiO_2	53.4	53.8	54.2	53.3	53.9	54.6	54.1
TiO_2	1.41	1.53	0.73	1.19	0.94	0.6	0.86
Al_2O_3	0.48	0.48	0.24	0.38	0.43	0.29	0.32
Cr_2O_3	0.11	0.02	0.07	0.01	0.88	0.22	0.59
FeO	3.63	3.51	2.99	3.75	2.89	3.16	2.64
MnO	0.09	0.03	0.12	0.10	0.04	0.11	0.09
MgO	16.2	16.5	17.1	16.3	17.2	17.2	17.1
CaO	24.7	24.4	24.7	24.7	24.2	24.0	24.6
Na_2O	0.48	0.46	0.22	0.54	0.33	0.42	0.24
K_2O	0.15	0.03	0.02	0.11	0.01	0.01	0.03
Total	100.7	100.7	100.4	100.3	100.8	100.6	100.7
Calculated atoms per 6 oxygens							
Si	1.952	1.958	1.974	1.956	1.956	1.982	1.965
Ti	0.039	0.042	0.020	0.033	0.026	0.016	0.023
Al	0.021	0.021	0.010	0.016	0.018	0.012	0.014
Cr	0.003	0.001	0.002	0.000	0.025	0.006	0.017
Fe	0.111	0.107	0.091	0.115	0.088	0.096	0.080
Mn	0.003	0.001	0.004	0.003	0.001	0.003	0.003
Mg	0.880	0.894	0.925	0.888	0.930	0.929	0.927
Ca	0.968	0.950	0.964	0.969	0.940	0.932	0.958
Na	0.034	0.032	0.016	0.038	0.023	0.030	0.017
K	0.007	0.001	0.001	0.005	0.000	0.000	0.001
Total	4.018	4.007	4.007	4.024	4.008	4.007	4.005

Number of points	1	2	3	4	5	6	7	8	9	10
					Sample KRV5					
SiO_2	52.9	53.1	52.6	52.6	53.4	53.5	52.6	53.3	52.8	53.1
TiO_2	1.02	0.77	1.09	1.32	1.09	0.63	1.09	0.84	0.87	1.11
Al_2O_3	0.27	0.25	0.35	0.51	0.19	0.09	0.44	0.25	0.22	0.41
Cr_2O_3	0.10	0.36	0.25	0.54	0.26	0.06	0.66	0.29	0.25	0.03
FeO	2.73	2.13	2.76	2.61	2.82	2.76	2.50	2.63	2.67	3.23
MnO	0.09	0.06	0.06	0.06	0.07	0.10	0.06	0.07	0.09	0.08
MgO	17.03	17.2	17.0	16.6	16.8	16.8	16.7	17.1	17.1	16.9
CaO	25.0	25.2	24.9	24.9	25.1	24.7	24.6	24.7	24.9	24.1
Na_2O	0.22	0.25	0.30	0.36	0.29	0.40	0.31	0.37	0.26	0.45
K_2O	0.01	0.01	0.01	0.01	0.01	0.00	0.01	0.02	0.01	0.02
Total	99.38	99.23	99.29	99.48	99.91	99.1	98.93	99.55	99.18	99.39
Calculated atoms per 6 oxygens										
Si	1.951	1.955	1.942	1.938	1.958	1.975	1.946	1.959	1.952	1.955
Ti	0.028	0.021	0.030	0.037	0.030	0.017	0.030	0.023	0.024	0.031
Al	0.012	0.011	0.015	0.022	0.008	0.004	0.019	0.011	0.010	0.018
Cr	0.003	0.010	0.007	0.016	0.008	0.002	0.019	0.008	0.007	0.001
Fe	0.084	0.066	0.085	0.081	0.087	0.085	0.077	0.081	0.083	0.100
Mn	0.003	0.002	0.002	0.002	0.002	0.003	0.002	0.002	0.003	0.002
Mg	0.936	0.945	0.937	0.914	0.916	0.927	0.923	0.938	0.941	0.931
Ca	0.988	0.993	0.985	0.984	0.985	0.978	0.976	0.971	0.987	0.951
Na	0.016	0.018	0.021	0.026	0.021	0.029	0.022	0.026	0.019	0.032
K	0.000	0.000	0.000	0.000	0.000	0.000	0.000	0.001	0.000	0.001
Total	4.021	4.022	4.027	4.019	4.015	4.019	4.016	4.022	4.025	4.021

Number of points	11	12	13	14	15	16	17
			Sample KRV5 continued				
SiO_2	53.3	53.0	52.3	53.4	51.9	52.4	52.6
TiO_2	0.87	1.00	1.45	0.63	1.70	1.10	0.80
Al_2O_3	0.33	0.34	0.38	0.12	0.79	0.43	0.30
Cr_2O_3	0.04	0.58	0.38	0.05	0.30	0.38	0.31
FeO	3.33	2.56	2.93	3.11	3.08	2.62	2.64
MnO	0.10	0.05	0.06	0.10	0.07	0.06	0.07
MgO	16.9	16.8	16.7	16.9	16.5	16.9	17.3
CaO	24.0	24.8	24.8	24.5	24.6	24.7	25.1
Na_2O	0.46	0.34	0.41	0.33	0.36	0.30	0.26
K_2O	0.00	0.01	0.02	0.02	0.01	0.01	0.02
Total	99.32	99.41	99.44	99.09	99.31	98.84	99.38
Calculated atoms per 6 oxygens							
Si	1.964	1.954	1.934	1.972	1.920	1.943	1.943
Ti	0.024	0.028	0.040	0.018	0.047	0.031	0.022
Al	0.014	0.015	0.017	0.005	0.034	0.019	0.013
Cr	0.001	0.017	0.011	0.001	0.009	0.011	0.009
Fe	0.103	0.079	0.091	0.096	0.095	0.081	0.082
Mn	0.003	0.002	0.002	0.003	0.002	0.002	0.002
Mg	0.928	0.920	0.921	0.928	0.912	0.934	0.950
Ca	0.949	0.977	0.980	0.970	0.977	0.981	0.992
Na	0.033	0.024	0.029	0.024	0.026	0.022	0.019
K	0.000	0.000	0.001	0.001	0.000	0.000	0.001
Total	4.020	4.015	4.027	4.019	4.024	4.023	4.033

Number of points	1	2	3	4	5	6	7	8	9	10	11
						Sample KRV12					
SiO_2	51.9	51.5	52.37	52.87	52.31	53.3	49.7	52.34	51.5	50.9	51.9
TiO_2	0.14	0.31	1.01	0.9	1.03	0.48	1.31	1.14	1.5	1.12	1.33
Al_2O_3	0.70	1.25	0.36	0.26	0.36	0.15	0.8	0.27	0.4	0.26	0.52
Cr_2O_3	0.00	0.01	0.41	0.41	0.38	0.01	0.48	0.52	0.47	0.36	0.37
FeO	10.8	7.98	2.39	2.38	2.42	4.55	3.02	2.94	3.13	3.32	2.83
MnO	0.82	0.62	0.06	0.08	0.05	0.17	0.07	0.07	0.08	0.08	0.06
MgO	14.1	14.2	17.4	17.2	17.3	16.6	15.4	16.5	17.0	16.7	16.9
CaO	20.5	22.7	25.1	25.0	25.1	24.1	24.7	24.7	24.6	24.2	24.8
Na_2O	0.58	0.54	0.28	0.24	0.31	0.42	0.49	0.46	0.57	0.62	0.38
K_2O	0.01	0.02	0.01	0.01	0.01	0.03	0.31	0.01	0.01	0.06	0.02
Total	99.49	99.15	99.42	99.25	99.3	99.77	96.3	98.95	99.34	97.59	99.09
Calculated atoms per 6 oxygens											
Si	1.967	1.943	1.933	1.950	1.933	1.967	1.912	1.944	1.913	1.924	1.926
Ti	0.004	0.009	0.028	0.025	0.029	0.013	0.038	0.032	0.042	0.032	0.037
Al	0.031	0.056	0.016	0.011	0.016	0.007	0.036	0.012	0.018	0.012	0.023
Cr	0.000	0.000	0.012	0.012	0.011	0.000	0.015	0.015	0.014	0.011	0.011
Fe	0.341	0.252	0.074	0.073	0.075	0.141	0.097	0.091	0.097	0.105	0.088
Mn	0.026	0.020	0.002	0.002	0.002	0.005	0.002	0.002	0.003	0.003	0.002
Mg	0.793	0.800	0.958	0.943	0.955	0.911	0.881	0.916	0.942	0.942	0.935
Ca	0.830	0.919	0.994	0.987	0.993	0.956	1.018	0.982	0.980	0.980	0.985
Na	0.043	0.040	0.020	0.017	0.022	0.030	0.037	0.033	0.041	0.045	0.027
K	0.000	0.001	0.000	0.000	0.000	0.001	0.015	0.000	0.000	0.003	0.001
Total	4.035	4.040	4.036	4.022	4.036	4.032	4.051	4.028	4.050	4.057	4.034

Note: Red highlighted point are cores, and yellow are rims

Number of points	12	13	14	15
	Sample KRV12 continued			
SiO_2	53.0	53.0	52.3	51.7
TiO_2	0.97	0.84	1.11	1.49
Al_2O_3	0.18	0.15	0.21	0.62
Cr_2O_3	0.06	0.31	0.18	0.89
FeO	3.13	3.25	3.48	2.85
MnO	0.11	0.09	0.08	0.07
MgO	16.8	16.49	16.7	16.6
CaO	24.9	24.3	24.6	24.6
Na_2O	0.38	0.56	0.53	0.44
K_2O	0.02	0.03	0.03	0.02
Total	99.52	99.05	99.21	99.23
Calculated atoms per 6 oxygens				
Si	1.954	1.964	1.941	1.917
Ti	0.027	0.023	0.031	0.042
Al	0.008	0.007	0.009	0.027
Cr	0.002	0.009	0.005	0.026
Fe	0.097	0.101	0.108	0.919
Mn	0.003	0.003	0.003	0.001
Mg	0.924	0.911	0.923	0.978
Ca	0.985	0.966	0.980	0.002
Na	0.027	0.040	0.038	0.032
K	0.001	0.001	0.001	0.088
Total	4.028	4.026	4.040	4.031